On the Impact of Structured Solar Wind on Magnetosheath Jets and Their Environment

Linking Heliophysics and Near-Earth Space Plasma Research

Florian Koller

June 7, 2024

UNIVERSITÄT GRAZ
UNIVERSITY OF GRAZ
Institute of Physics

PhD Thesis

On the Impact of Structured Solar Wind on Magnetosheath Jets and Their Environment

Linking Heliophysics and Near-Earth Space Plasma Research

Florian Koller

in partial fulfillment of the requirements for the degree of
PhD

Supervisor Assoc. Prof. Dr. Manuela Stadlober-Temmer

June 7, 2024

Florian Koller

On the Impact of Structured Solar Wind on Magnetosheath Jets and Their Environment — Linking Heliophysics and Near-Earth Space Plasma Research

Thesis in partial fulfillment of the requirements for the degree of PhD;

Institute of Physics, NAWI Graz, University of Graz.

Supervisor: Assoc. Prof. Dr. Manuela Stadlober-Temmer[1]
External Reader: Prof. Dr. Xochitl Blanco-Cano[2]

[1] Institut für Physik, NAWI Graz, University of Graz, Universitätsplatz 5/II, 8010 Graz, Austria.
[2] Instituto de Geofísica, Universidad Nacional Autónoma de México, Circuito de la Investigación Científica s/n, Ciudad Universitaria, Mexico City, Mexico.

Abstract

The supersonic plasma outflow from the Sun, known as the solar wind, constantly bombards the planets in the solar system. The Earth's magnetic field shields us from these particles. In the region between Earth's magnetosphere and interplanetary space, one finds the so-called magnetosheath. Here, the solar wind plasma is compressed at a shock front and flows around the Earth. The magnetosheath plasma is highly turbulent and prone to numerous effects and transients. Magnetosheath jets are one of these transients that have gained increased attention in scientific research over the past decades. Both the magnetosheath and the jets depend on conditions in the solar wind. These conditions, however, are not always steady and constant: the solar wind consists of different types and large-scale structures embedded within it. Our goal is to investigate the influence of large-scale solar wind structures on the magnetosheath and magnetosheath jets. By using solar wind data from OMNI and magnetosheath measurements by THEMIS, we find that coronal mass ejections decrease the occurrence of jets, while fast solar wind streams increase their occurrence. In a follow-up study, we confirm that the magnetic field angle in these structures is the primary cause of the modification of jet occurrence. Other parameters, however, also play a minor role. These results point to the fact that jets mostly appear behind the quasi-parallel shock region, which is the area where the interplanetary magnetic field is perpendicular to the shock surface. A reliable classification of this region is usually done by measuring the flux of highly energetic ions. However, we find that fast solar wind conditions can complicate classification efforts by significantly increasing the ion energy in the magnetosheath. The interdisciplinary approach of connecting solar wind research with near-Earth plasma research that we use throughout this work opens up new possibilities to make connections between different fields of research.

Zuammenfassung

Der schnelle Plasmastrom von der Sonne, der Sonnenwind, bombardiert andauernd die Planeten im Sonnensystem. Das Magnetfeld der Erde schirmt uns gegen diese Teilchen ab. In der Region zwischen der Magnetosphäre der Erde und dem interplanetaren Raum findet man die so genannte Magnetosheath. Hier wird das Sonnenwindplasma an einer Schockfront komprimiert und fließt um die Erde herum. Das Plasma in der Magnetosheath ist turbulent und anfällig für zahlreiche Effekte und Transienten. Magnetosheath-Jets sind eine dieser Transienten, die in den letzten Jahrzehnten in der wissenschaftlichen Forschung verstärkt Beachtung gefunden haben. Sowohl die Magnetosheath als auch die Jets hängen von den Bedingungen im Sonnenwind ab. Diese Bedingungen sind jedoch nicht immer gleichmäßig und konstant: Der Sonnenwind besteht aus verschiedenen Typen und großräumigen Strukturen, die in ihm eingebettet sind. Unser Ziel ist es, den Einfluss großräumiger Sonnenwindstrukturen auf die Magnetosheath und die Magnetosheath-Jets zu untersuchen. Unter Verwendung von Sonnenwinddaten von OMNI und Magnetosheath-Messungen von THEMIS finden wir heraus, dass koronale Massenauswürfe das Auftreten von Jets verringern, während schnelle Sonnenwindströme ihr Auftreten erhöhen. In einer Folgestudie bestätigen wir, dass der Magnetfeldwinkel in diesen Strukturen die Hauptursache für die Veränderung des Auftretens von Jets ist. Andere Parameter spielen jedoch auch eine - wenn auch untergeordnete - Rolle. Diese Ergebnisse deuten darauf hin, dass Jets meist hinter der quasi-parallelen Schockregion auftreten, also in dem Bereich, in dem das interplanetare Magnetfeld senkrecht zur Schockoberfläche steht. Eine zuverlässige Klassifizierung dieser Region erfolgt üblicherweise durch die Messung des Flusses hochenergetischer Ionen. Wir haben jedoch festgestellt, dass schnelle Sonnenwinde die Klassifizierung erschweren können, da sie die Ionenenergie in der Magnetosheath deutlich erhöhen. Der interdisziplinäre Ansatz, den wir in dieser Arbeit gewählt haben, um die Sonnenwindforschung mit der erdnahen Plasmaforschung zu verbinden, eröffnet neue Möglichkeiten, um Verbindungen zwischen verschiedenen Forschungsgebieten herzustellen.

Acknowledgement

First, I want to thank my supervisor, Manuela Stadlober-Temmer, for this opportunity and for trusting me with this work. Her counsel, input, and help at every step have been invaluable in introducing me to the academic world.

I also thank the group at the Institute of Physics, in particular Roland and Klaus for the indispensable IT support, Karin, Claudia, and Robert for their organizational efforts in the secretary's office, and Astrid for the counsel and help throughout the past six years. I also want to thank the best office mates possible for a PhD: Greta, Daniel, Amaia, Carlos, and Jose-Ivan. Thanks to all my PhD and postdoc colleagues at the institute who made every lunch break and every movie night a special time. I also thank my colleagues at the Space Research Institute, in particular Luis, Cyril, and Zoltan, and our colleagues who have moved to new frontiers like Ferdinand and Owen. I am grateful to our small and expanding jet community, in particular Adrian L., Adrian P., Laura, Savvas, Jonas, Eva, Niki, Georg, and Tara. Thanks to all senior scientists in our jet community, especially all colleagues that joined our jet meeting in Graz 2023. In particular I want to thank Xochitl Blanco-Cano to agree to be my second reviewer for this work.

This work would not have been possible without the help of my family, in particular my parents Rosmarie and Arnulf, who always supported me beyond all measures without question. Thanks to my brothers, my sisters-in-law, and my nieces and nephew for keeping our family strongly tied together.

I thank all my friends who supported me throughout the years. My Graz physics colleagues Martin, Verena, Stefan, Christian, Hannes, David, Marco, Michael, Anita, Kevin, Anna, and many more who helped me survive the Bachelor's, Master's, and PhD time, and I wouldn't want to miss a second of it. Thanks to my flatmates Martin Star, Eva, Mathias, and Stefan for the great time in a relaxed home. Thanks to all friends young and old, in particular David (whose screens made this thesis possible), Stefan K.Ham, Sandro, Stefan Mr.L. & Anastasia, Heimo, and Patrick A.

Sustenance is of high importance, therefore I thank the local Spar for their nutritious food, in particular the pizza bread and latte espresso that made this work possible.

I gratefully acknowledge the Austrian Science Fund (FWF): P 33285 (under the PI-ship of Ferdinand Plaschke, Owen Roberts, Zoltan Vörös, and Manuela Stadlober-Temmer) for supporting this project. I thank the Physics Doctoral School at the University of Graz for the travel grant that allowed me to participate in the Iberian Space Science Summer School in Coimbra, Portugal, 2023. I also thank the NAWI Förderungsstipendium for the research stay grant in 2023 that made the collaboration with my colleague Savvas Raptis at The Johns Hopkins University possible.

And finally, I thank my wife Sophie for supporting me at every step of this journey. I cannot wait to tackle all the future adventures that lie ahead together with you.

Contents

1 Introduction and Thesis Overview

1.1 Overview and motivation

The solar system is our laboratory to understand fundamental plasma processes in the universe. The Sun, our plasma source, provides us with a continuous stream of charged particles called the solar wind. The solar wind consist of protons, electrons, alpha particles, and heavier elements as well. The plasma flow can be differentiated into large-scale structures and different origin sources in the Sun's atmosphere, all of which are dependent on the solar activity (Temmer, 2021). This plasma drags the magnetic field of the Sun with it, which we denote as interplanetary magnetic field (IMF). The planets in the solar system have either an intrinsic magnetic field or an induced magnetic field, shielding the planet from this constant plasma bombardment coming from the Sun. The interaction of the solar wind with these magnetic fields causes a variety of structures and secondary effects, which we will discuss in more detail in this work. In particular, we focus on the dayside region of Earth's magnetic field, that is, the area between the Earth and the Sun (also denoted as subsolar region). The solar wind hits Earth's magnetic field at supersonic velocities, causing the solar wind plasma to suddenly decelerate - a shock is formed. The region downstream of this shock is called the magnetosheath, a turbulent region of highly interacting compressed solar wind plasma. The inner boundary of the magnetosheath is the magnetopause, which is the boundary to the Earth's magnetic field. Every large scale structure in the solar wind must first traverse the Earth's shock and the magnetosheath before it hits Earth's magnetic field.

The magnetosheath itself is home to a variety of structures. The past three decades saw a rise in research on dynamic pressure enhancements in the magnetosheath. These transients are also called magnetosheath jets and were first reported by Němeček et al. (1998). A review paper on jets by Plaschke et al. (2018) kick-started increased interest and research efforts on magnetosheath jets in recent years. These jets can impact the magnetopause and cause effects in the Earth's magnetic field as well (Hietala et al., 2018; Nykyri et al., 2019; Wang et al., 2022; Dmitriev and Suvorova, 2023). Therefore, magnetosheath jets serve as a link between the upstream solar wind from the Sun and the magnetic field of the Earth. The formation of the majority of jets is connected to the bow shock and has been investigated increasingly in the past years (Hietala et al., 2009; Suni et al., 2021; Raptis et al.,

2022a). It is of particular interest to understand which solar wind conditions cause the formation of jets. First statistical analysis on the solar wind influence on jet occurrence has been conducted by Plaschke et al. (2013), Vuorinen et al. (2019), and LaMoury et al. (2021). The increasing amount of near-Earth plasma data from spacecraft gives us the opportunity to further investigate this connection.

In particular, the influence of large-scale solar wind structures on the occurrence of jets remained an open question, one, that we aim to answer within the work conducted in this thesis. There are two main motivations for this analysis: first, these large-scale structures in the solar wind are the cause of geomagnetic effects and thus of high relevance for technical infrastructure as well as navigation and communication systems. Jets are an additional way of transferring energy from the shock to Earth's magnetic field, therefore we want to understand, if and how these jets play a role during geoeffective events. Second, the solar wind undergoes an 11-year cycle of activity, which causes a change of large-scale structure occurrence throughout this time span. In order to understand the occurrence (and consequently the impact) of jets on long time scales, we first must understand, how jet formation is influenced by these structures in the solar wind.

This analysis is interdisciplinary by nature and immediately raises a follow-up question: how is the magnetosheath in general influenced by structured solar wind? The connection of heliospheric research with magnetosheath research is so-far underinvestigated and poses a great opportunity to better understand the full chain of events from the Sun to Earth's magnetic field. Crucially, large-scale solar wind structures fundamentally change the plasma environment of the magnetosheath. This in turn influences all research conducted in this region, including jets. The combination of solar wind research with near-Earth plasma research helps us to build new connections by combining knowledge from different research subfields by analyzing common underlying physical processes.

Figure 1.1 illustrates the system that we are analyzing in this work: the terrestrial dayside magnetosphere and magnetosheath. The magnetosheath and jets within it are influenced by various types of structured solar wind (indicated by the list of solar wind types on the left side of the figure). The connection of upstream solar wind conditions with downstream effects is the focus of the thesis. Section 2.2 describes the classification of the solar wind, while Section 2.3.2 describes the magnetosheath.

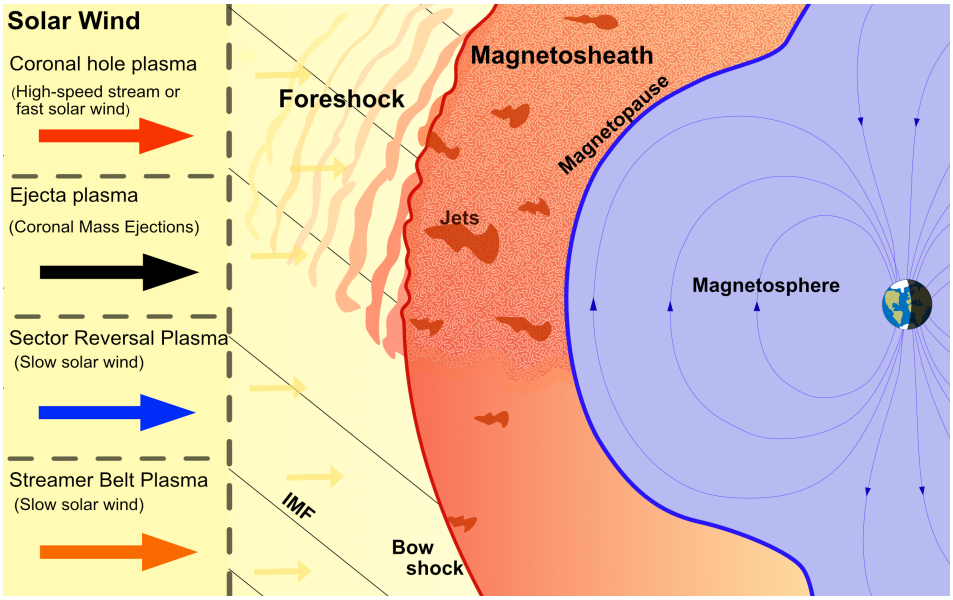

Fig. 1.1: Overview of Earth's dayside magnetosphere and magnetosheath. Different types of structured solar wind is listed on the left side of the figure. The thesis focuses on the influence of structured solar wind on magnetosheath and jets. This figure is adapted from Koller et al. (2024).

1.2 Overview of Thesis Structure

In this thesis we investigate the effect of the solar wind and large-scale structures within the solar wind on the magnetosheath with a focus on magnetosheath jets. In particular, we address the following questions:

- What influence do coronal mass ejections and stream interaction regions have on the occurrence of jets in the magnetosheath?
- Which parameters in coronal mass ejections and stream interaction regions cause the modification of jet occurrence in the magnetosheath and why?
- How is structured solar wind changing the plasma environment - in particular the ion energy - in the magnetosheath and how does this affect magnetosheath classification?

To answer these questions, we use THEMIS spacecraft measurements in the dayside magnetosheath. This is combined with OMNI data to know the solar wind conditions that caused the parameter measured in the magnetosheath. The work is focused on statistical results to gain knowledge on general trends and long term effects over more than a solar cycle. Automatic detection of the magnetosheath region in THEMIS data is performed to obtain all intervals of interest. Further studies

on these subintervals (like the detection of jets based on dynamic pressure criteria) are conducted. The solar wind condition by OMNI during times of interest are the main focus of these studies. The overarching aim of the FWF project which financed this thesis (P 33285: Magnetosheath jets throughout the solar cycle) is to learn about the long-term effects of the solar cycle on the magnetosheath and jets. Tackling the questions posed above is the key to answer this overarching research question.

This thesis is structured as follows: To give context to the published works, we first introduce all necessary topics and concepts.We start with looking at the basics of plasma physics relevant for the work at hand, then we introduce the solar wind and structures within it. This is followed by the description of shock physics and phenomena in the downstream magnetosheath. A special focus lies on magnetosheath jets by quickly reviewing recent discoveries in this field of research. Afterwards the three first author papers published in peer-reviewed journals are presented. The first paper showcases that solar wind structures like CMEs and SIRs modify the occurrence of jets. The second paper analyzes, which parameters in these structures cause the change in jet occurrence in the magnetosheath. The third paper sheds light on how solar wind structures in general change the magnetosheath plasma, especially in the context of classifying the plasma environment. In the end we will discuss our work in the context of current scientific efforts, discuss the methodology, and summarize our conclusions. We end with open questions and outlook on subsequent work based on our results.

Here we briefly summarize the results of our published articles:

Paper1: In Koller et al. (2022), published in *The Journal of Geophysical Research: Space Physics*, we investigated the impact of large-scale solar wind structures on the occurrence rate of jets in the magnetosheath. In particular, we analyzed the number of jets that appear during CMEs, CME-driven sheaths, SIR compression regions and SIR high-speed streams. We used OMNI data for the solar wind and THEMIS for the dayside magnetosheath in the time range between 2008 and 2021. Two different jet detection criteria were employed. Superposed epoch analysis was used to infer the influence of the large-scale solar wind structures on jet occurrence in more detail. We found that the number of jets measured in the magnetosheath increases during solar wind high-speed streams. On the other hand, we detected a significant decrease in jet occurrence during CMEs and their driven sheaths. This is the first published work that connected solar wind structures with these kind of magnetosheath transients.

Paper 2: In Koller et al. (2023), published in *The Journal of Geophysical Research: Space Physics*, we further investigated the trend found in Koller et al. (2022) by analyzing the plasma parameters in large-scale solar wind structures. OMNI data

was used for the solar wind and THEMIS for the magnetosheath in the time range of 2008 to 2022. We found that the unfavorable conditions for jet occurrence in CMEs primarily come from the statistically high probability of high cone angles. In addition to that, the strong magnetic field and, as a consequence, low Alfvén Mach number also result in a reduced number of jets. The plasma parameters in high-speed streams on the other hand show mostly favorable conditions for jet formation.

Paper 3: In Koller et al. (2024), published in *The Astrophysical Journal Letters*, we investigated the influence of solar wind types on the magnetosheath in general. The previous publications (Koller et al. (2022) and Koller et al. (2023)) pointed towards the fact that the quasi-parallel magnetosheath and foreshock buildup is the most important factor for jet formation. A correct classification of quasi-parallel and quasi-perpendicular magnetosheath is therefore in order. In this study, we point out that fast solar wind can drastically increase the energy distribution of ions in the magnetosheath, which is one of the primary methods to differentiate the quasi-parallel from the quasi-perpendicular region. The results of this study are of substantial importance for future analysis on magnetosheath effects under different solar wind types.

2 The Heliophysical Plasma Environment Up - and Downstream of the Earth's Bow Shock

2.1 Basics of Plasma Physics

We will briefly introduce important plasma physics concepts and basics below. For a detailed discussion of the topic we refer to space plasma physics textbooks (e.g. Baumjohann and Treumann, 1996; Treumann and Baumjohann, 1997).

The majority of the observational baryonic matter in the universe is in the plasma state. In plasma, the negatively charged electrons are no longer bound to the positively charged atom nucleus made out of protons and neutrons. Therefore, ions and electrons can move independently, which gives rise to a plethora of new effects not possible in neutral matter.

Plasma is well defined by three criteria that need to be fulfilled. The first criterion requires the plasma to be quasi-neutral on the scale length L in question. This means that the electric potential of an individual charge is sufficiently decreased by the surrounding charges, so that the whole plasma appears in-quasi-neutral state above a certain length. The Debye shielding length λ_D describes the length after which the potential decreased by $1/e$ and is defined as

$$\lambda_D = \sqrt{\frac{\epsilon_0 k_B T_e}{n_0 e^2}} \tag{2.1}$$

where ϵ_0 denotes the dielectric constant, k_B the Boltzmann constant, T_e the electron temperature, n_0 the particle density, and e the elementary charge. The first plasma criterion is fulfilled when $\lambda_D << L$, which holds true for the plasma analyzed throughout this work. The second criterion requires that the plasma parameter $\Lambda = n_e \lambda^3 >> 1$, where n_e denotes the electron density. Thus, the number of charged particles within a volume defined by the Debye length should be much greater than one. The third criterion requires that the collision of plasma particles with neutral

particles is limited ($\omega\tau > 1$, with ω being the circular plasma oscillation frequency and τ the average time of collisions with neutral particles). The plasma oscillation frequency or Langmuir frequency is given as

$$f_p = \frac{1}{2\pi}\sqrt{\frac{ne^2}{m\epsilon_0}} \tag{2.2}$$

with n and m being the density and mass of the particle in question, respectively.

Magnetic fields cause gyration of plasma particles due to the Lorentz force $F_L = q(E + v \times B)$, with q being the charge, E the electric field, v the particle velocity, and B the magnetic field. The resulting gyration or cyclotron frequency is given as $\omega_c = \frac{eB}{m}$, resulting in a gyration radius (also called Larmor radius or gyroradius) $r_L = \frac{mv_\perp}{eB}$ with $v_\perp$ being the particle velocity perpendicular to the magnetic field vector. The Larmor radius is different for protons and electrons due to their mass and they gyrate in opposite directions due to the sign of the charge. In the solar wind, the proton gyroradius at 1 astronomical unit ($AU = 149,597,870,700\,\mathrm{m}$) is about 160 km and for electrons about 2 km (Verscharen et al., 2019).

Magnetohydrodynamics (MHD) is a description of macroscopic plasma flow that treats plasma as a magnetized fluid. In general, plasma is described by the following equations (Baumjohann and Treumann, 1996):

$$\frac{\partial n}{\partial t} + \nabla \cdot (n\mathbf{v}) = 0 \tag{2.3}$$

$$\frac{\partial (nm\mathbf{v})}{\partial t} + \nabla \cdot (nm\mathbf{v}\mathbf{v}) = -\nabla \cdot \mathbf{P} + \rho\mathbf{E} + \mathbf{j} \times \mathbf{B} \tag{2.4}$$

$$\mathbf{E} + \mathbf{v} \times \mathbf{B} = \eta\mathbf{j} + \frac{1}{ne}\mathbf{j} \times \mathbf{B} - \frac{1}{ne}\nabla \cdot \mathbf{P}_e + \frac{m_e}{ne^2}\frac{\partial \mathbf{j}}{\partial t} \tag{2.5}$$

$$\nabla \times \mathbf{B} = \mu_0\mathbf{j} + \mu_0\epsilon_0\frac{\partial \mathbf{E}}{\partial t} \tag{2.6}$$

$$\nabla \times \mathbf{E} = -\frac{\partial \mathbf{B}}{\partial t} \tag{2.7}$$

$$\nabla \cdot \mathbf{B} = 0. \tag{2.8}$$

Vector quantities are marked in bold. Here, $\mathbf{P}$ denotes the total pressure tensor, $\mathbf{j}$ the electric current density, η the plasma resistivity, and μ_0 the vacuum permeability. An equation of state or energy equation is used to complete the system of equations. An adiabatic relation like $P = const \cdot \rho^\gamma$ is often used with γ being the adiabatic exponent (usually set to 5/3 for ideal gas). Ideal MHD is a simplification of these equations utilizing the assumption that plasma is a perfect conductor without viscosity and thermal conductivity. In this assumption, electric field differences are compensated immediately by the freely moving ions (along magnetic field lines)

without losing energy in form of thermal losses. Thus, $dE = 0$ and $\eta = 0$. Several terms that describe viscosity vanish. In this simplified set of equations the plasma is bound to the magnetic field line (also called "frozen-in"). Ideal MHD is a good approximation for numerous space plasma applications. The description might locally break down when significant resistive effects take place. This can happen in high plasma beta (introduced below) regions due to high temperature and high densities. Specifically, in reconnection events (rearrangements of magnetic fields), the ideal MHD description does not hold. Reconnection is of great relevance for both solar physics (e.g., flare-CME occurrence and particle acceleration in the Sun's atmosphere) and magnetospheric physics (e.g., dayside and nightside reconnection), however, the detailed description of this phenomenon goes beyond the scope of this work. At this point we also want to stress that the analysis in this work considers large plasma structures, i.e., structures much larger than the Debye length or the ion gyroradius.

Introducing linear perturbation theory into the set of MHD equations leads to the description of MHD waves. One of the fundamental type of waves in plasma is the Alfvén wave. It propagates along in the direction of the magnetic field vector with an amplitude perpendicular to the field line. The propagation speed is given by the Alfvén velocity

$$v_A = \frac{B}{\sqrt{\mu_0 \rho}} \tag{2.9}$$

and is thus visibly only dependent on the magnetic field strength and density of the plasma. Sonic waves also appear, as is common in any fluid. Their velocity is given as $v_s = \sqrt{\gamma \frac{P}{\rho}}$ and moves independent of the magnetic field orientation. The MHD compressional wave that propagates normal of the magnetic field orientation has a characteristic velocity (also called magnetosonic speed) given as

$$v_{ms} = \sqrt{v_A^2 + v_s^2}. \tag{2.10}$$

For arbitrary wave propagation angles one arrives at two different magnetoacoustic waves: the fast MHD mode and the slow MHD mode.

There are important parameters relevant for the description and analysis of space plasmas. Subsequent analysis in this work utilizes the dynamic pressure of plasma, which physically describes the kinetic energy of particles in a volume. It is described as

$$p_{dyn} = \frac{1}{2} \rho \cdot v^2. \tag{2.11}$$

In this equation usually only the plasma ions are used due to the negligible mass of electrons. It is important to note that in literature the dynamic pressure is also often used without the factor $1/2$.

The plasma beta (β) is a measure that indicates whether a plasma is governed by the thermal or magnetic pressure. The measure is the ratio of both types of pressure and explicitly given as

$$\beta = \frac{nk_BT}{B^2/2\mu_0}. \tag{2.12}$$

A β value below one indicates that the magnetic pressure dominates and the plasma closely follows magnetic field lines, while β above one indicates that high thermal movement of the ions dominate the plasma. In the solar wind the plasma beta is usually found to be around a value of one, with varying ranges depending on large-scale structures, plasma origin, and effects and processes acting on the plasma.

Mach numbers are relevant for the description of shock physics. The Alfvén Mach number is given as

$$M_A = \frac{v}{v_A} = \frac{v}{\sqrt{B^2/\mu_0\rho}} \tag{2.13}$$

and the magnetosonic Mach number as

$$M_{ms} = \frac{v}{v_{ms}} = \frac{v}{\sqrt{v_A^2 + v_s^2}}. \tag{2.14}$$

As described above, the fast and slow wave propagation modes result in different velocities relevant for the Mach number depending on the propagation angle relative to the magnetic field orientation.

Finally we also want to introduce the so-called cone angle as the angle of the magnetic field vector with respect to the Sun-Earth line. This parameter is connected to geocentric coordinate systems and of most relevance for solar wind plasma at 1 AU:

$$\Phi = arccos\left(\frac{|B_x|}{B}\right). \tag{2.15}$$

Here, B_x denotes the magnetic field component along the Sun-Earth line. Here the angle is not depending on whether the magnetic field orientation is sunward or earthward. This angle is used in the geocentric solar ecliptic system (GSE) and the geocentric solar magnetospheric system (GSM). Both GSE and GSM have the X-axis pointing from the Earth to the Sun. The GSE-Y axis lies in the ecliptic plane pointing towards dusk (against Earth's orbital motion) and GSE-Z lies perpendicular to the ecliptic. The GSM-Y axis is defined as being perpendicular to Earth's magnetic dipole and GSM-Z points in the same direction as the magnetic north pole. GSM is particularly useful for describing the impact of the IMF orientation on the Earth' magnetic field and subsequent processes in the magnetosphere. This work focused on GSE coordinates to describe the Sun and solar wind impact on the plasma environment outside of the magnetosphere.

2.1.1 Plasma Measurements Using Spacecraft

Instruments on spacecraft are used to measure in-situ properties of plasma in space. Knowledge on the system and the caveats of each mission and instrument are necessary for studying space plasmas. The solar wind is continuously monitored using spacecraft that orbit the Lagrange point 1 (L1). The gravitational pull of the Sun, the Earth, and the centrifugal force acting on an object are equalized at L1, allowing spacecraft to permanently stay at the position and measure the solar wind. The L1 point in the Sun-Earth system is about 1.5 million km sunward of the Earth. The ACE (Stone et al., 1998) and Wind (Harten and Clark, 1995) spacecraft orbit L1 and provide continuous solar wind measurements. The data of both missions data are usually used to compile the OMNI database (King and Papitashvili, 2005). The high-resolution OMNI dataset provides plasma parameters in 1 min temporal resolution. Because of the distance of the L1 point, the plasma measured there needs about 40 minutes to reach the bow shock of the Earth. In OMNI, the measured solar wind values are propagated to the nose of the bow shock to predict the plasma parameters that hit the Earth's magnetospheric system. One important caveat to note here is that the spacecraft are not located exactly at L1 and can have significant distances of tens of earth radii away from the Sun-Earth line (Walsh et al., 2019; Borovsky, 2018). This could introduce an uncertainty because the plasma measured at these spacecraft might not exactly match the plasma that hits the Earth's magnetosphere.

Near Earth plasma measurements are conducted e.g. by multi spacecraft missions that orbit either Earth or the Moon. Cluster (Escoubet et al., 1997) is a mission utilizing 4 spacecraft in an elliptical orbit in up to 90 degree orbital inclination that started in 2001. THEMIS (Angelopoulos, 2008) is a mission comprising of 5 spacecraft that started in 2007 in elliptical orbits around the Earth with varying apogees and inter-spacecraft distances. Probe B and C of the THEMIS mission were transferred to a lunar orbit from 2010 onward (Angelopoulos, 2011). The Magnetospheric Multiscale mission (MMS, Burch et al., 2016) consists of 4 spacecraft in elliptical Earth orbits with varying apogees as well and started in 2015. MMS mostly utilizes a tight spacecraft formation (with spacecraft distances of about 10 km) to study effects on short temporal and spatial scales. The research conducted as part of this thesis primarily uses THEMIS data due to the sufficient spatial coverage of the dayside magnetosheath and the temporal coverage comprising more than a full solar cycle.

Herein we briefly describe some of the instruments of THEMIS important for the subsequent analysis. Magnetic fields are measured using a Fluxgate Magnetometer (FGM, Auster et al., 2008). THEMIS spacecraft have a fluxgate sensor on a 2m

long boom and can measure range of $\pm 25,000$ nT and temporal resolutions of up to 128 Hz. The electrostatic analyzer on THEMIS (ESA, McFadden et al., 2008) measures ion and electron distribution functions from which the plasma moments like density, velocity, and temperature are derived. The measured ion energy distribution ranges from ~6–7 eV to ~25 keV. THEMIS spacecraft, like Cluster and MMS, are spinning with rotation periods of several seconds to allow measurements in every direction. The ESA instrument sweeps the full 4π steradian coverage every 3 s with 32 logarithmically spaced energy bins. Plasma moments are provided by either the on-board moments or ground ("reduced") calibrated moments. The on-board moments have an integrated correction for spacecraft potential using measurements from the electric field instrument (EFI, Bonnell et al., 2008).

The highly elliptical orbits used e.g. by THEMIS cause the spacecraft to transit vastly different plasma environments in a full orbit. The regions that can be studied vary depending on the current apogee and season of the year. THEMIS is able to measure about 4 months of dayside magnetosheath plasma each year. Up to several hours of magnetosheath measurements per orbit are possible. The spacecraft velocity is usually rather low compared to the plasma structures analyzed throughout this thesis, especially close to the apogee. Therefore, the spacecraft velocity is negligible when analyzing plasma speed in solar wind and magnetosheath. The orbit itself can introduce biases in long term statistics: Vuorinen et al. (2023b) pointed out that a lower apogee of THEMIS A, D, and E caused the detection of less magnetosheath jets between 2010 – 2015 compared to 2016 and onward. The low coverage of magnetosheath close the bow shock caused the main jet detection decrease rather than solar wind conditions during these years. Therefore it is important to consider how the orbit might affect the results, in particular when analyzing a plasma environment that shows differences between regions further out and further in.

2.2 The Solar Wind

In order to understand the environment of the near-Earth space, we first need to introduce the plasma flow which it is subject to at all times, the solar wind. For a more detailed discussion on the solar wind and its values at 1 AU beyond the brief introduction below we refer to Schwenn (2006), Cranmer et al. (2017), and Temmer (2021), and references therein. The constant outflow of plasma from the Sun's atmosphere, the solar wind, is made up of substructures of varying sizes and complexity. This solar wind dominates the plasma environment in the heliosphere and shapes the surrounding of magnetized and unmagnetized objects in the solar system. Large-scale differences in the plasma parameter can often be tracked down

to the source at the Sun. The solar atmosphere consists of the photosphere (which appears as the visible surface to the human eye), the chromosphere, and the solar corona, which extends far into the interplanetary space. The corona specifically shapes the plasma environment of the heliosphere due to its nature of being a radial outwards flow of particles. The plasma flow from the Sun and integrated structures within it evolve and change as they move through the interplanetary space. The plasma drags the magnetic field with it (frozen-in condition, see Section 2.1). Usual solar wind parameters at 1 AU show velocities of 250 to 800 km/s (Schwenn, 2006), magnetic field strengths up to about 20 nT and densities between 1 and 30 #/cm^3 (Yermolaev et al., 2009; Yermolaev et al., 2021; Koller et al., 2023). The solar wind plasma beta is found in a range between 0.1 and 30 (Yermolaev et al., 2009; Koller et al., 2023). The flow is usually both super-Alfvénic and super-magnetosonic, which is especially important for the formation of collisionless shocks as discussed in Section 2.3. The average angle of the magnetic field orientation in the solar wind is dictated by the rotation of the Sun: it is more radially aligned close to the Sun and increasingly inclined further outside the solar system due to the rotation of the whole system. This creates the so-called Parker spiral, describing the magnetic field angle projected on the ecliptic (Parker, 1958). Solar wind parameters are often correlated and thus can not be easily investigated without the full context (see Koller et al. (2023) for an analysis of correlation coefficients in plasma parameters). We herein discuss solar wind structures and types relevant for the subsequent analysis.

2.2.1 Solar Wind Structures and Types

We will first discuss solar wind structures detected at Earth and then consider the types of solar wind originating at the Sun.

Coronal mass ejections (henceforth denoted as CMEs) are explosive large scale transients that propagate through the interplanetary space (Chen, 2011). There are several models that describe the eruption and onset of CMEs (see the works by e.g. Green et al., 2018; Webb and Howard, 2012, for reviews on the onset of CMEs). A CME measured in interplanetary space is also often called interplanetary coronal mass ejection or ICME. Figure 2.1 showcases a CME example event measured by ACE. CMEs consist of a so-called magnetic flux rope, which shows a high magnetic field strength and a smoothly rotating pattern in the magnetic field vectors (visible in the second panel of Figure 2.1). This structure is sometimes also denoted as magnetic ejecta (ME), magnetic cloud, or magnetic obstacle (Rouillard, 2011). The exact definition might vary from structure to structure, however, the general parameters described herein hold true for most cases. The global structure of a CME has a croissant-shape and expands self-consistently while moving radially outwards away from the Sun. The strong magnetic pressure causes the flux rope to expand.

This results in a velocity gradient of the structure because the front is accelerated forwards while the back side expands backwards (the velocity gradient is visible in the third panel of Figure 2.1). The internal density is usually low due to the pressure balance under a dominating magnetic field pressure (panel one of Figure 2.1). This combination causes a low Alfvén Mach number (see Figure 2.1, panel four). A fast CME can drive a shockfront as it pushes against the slower solar wind in front of it. This interplanetary shock causes a sudden increase in density, magnetic field strength, and velocity analogous to planetary shocks (see Section 2.3). This forms a sheath region between the undisturbed solar wind and the flux rope. This CME-sheath, sometimes also denoted as CME disturbance, shows very turbulent plasma with erratic changes in the magnetic field vectors. The example in Figure 2.1 shows such a CME with a well-developed sheath region in front. A so-called leading edge between the CME-sheath and the magnetic ejecta was reported (Temmer and Bothmer, 2022). CME flux ropes often last for about a day and their sheath region about 10 hours at 1 AU (Koller et al., 2022).

CMEs can drive strong geoeffective responses and are thus subject to excessive research efforts throughout the space weather community. In particular, being able to forecast whether a CME will hit the Earth's magnetic field and forecasting the parameters within it is of paramount importance for the safety of human infrastructure both in space and on the ground.

Stream interaction regions (henceforth denoted as SIRs) are large-scale events that significantly shape the plasma flow in the heliosphere (see e.g. Cranmer, 2002; Tsurutani et al., 2006, for reviews on SIRs). They are caused by fast solar wind (also called high-speed streams or HSSs) emanating from coronal holes. These high-speed streams collide with the slow solar wind in front of it causing a compression region (as the plasma can not overtake the slow plasma due to the previously discussed frozen-in condition). Figure 2.2 showcases such an SIR event measured at 1 AU by ACE. The compression region consists of plasma with high density and shows an increasing velocity profile. The density peak marks the stream interface - the change from slow to fast solar wind plasma. The temperature after the stream interface steeply increases, while the density drops (Jian et al., 2006). The magnetic field components in this region are highly fluctuating due to the compression of the plasma. The rear of the SIR consists of the fast solar wind (or high-speed stream), which has by definition a high velocity and a resulting low density. Note that different works might call the combination of compression region and high-speed stream the SIR, while other works might only refer to the compression region itself as SIR. The co-rotating flow that emanates form the Sun is roughly time-stationary (Gosling and Pizzo, 1999), which is why SIRs cause a compression region spiral in the interplanetary space (see Figure 2.3). This is the reason why SIRs are also called co-rotating interaction regions (CIRs Smith and Wolfe, 1976; Gosling and Pizzo,

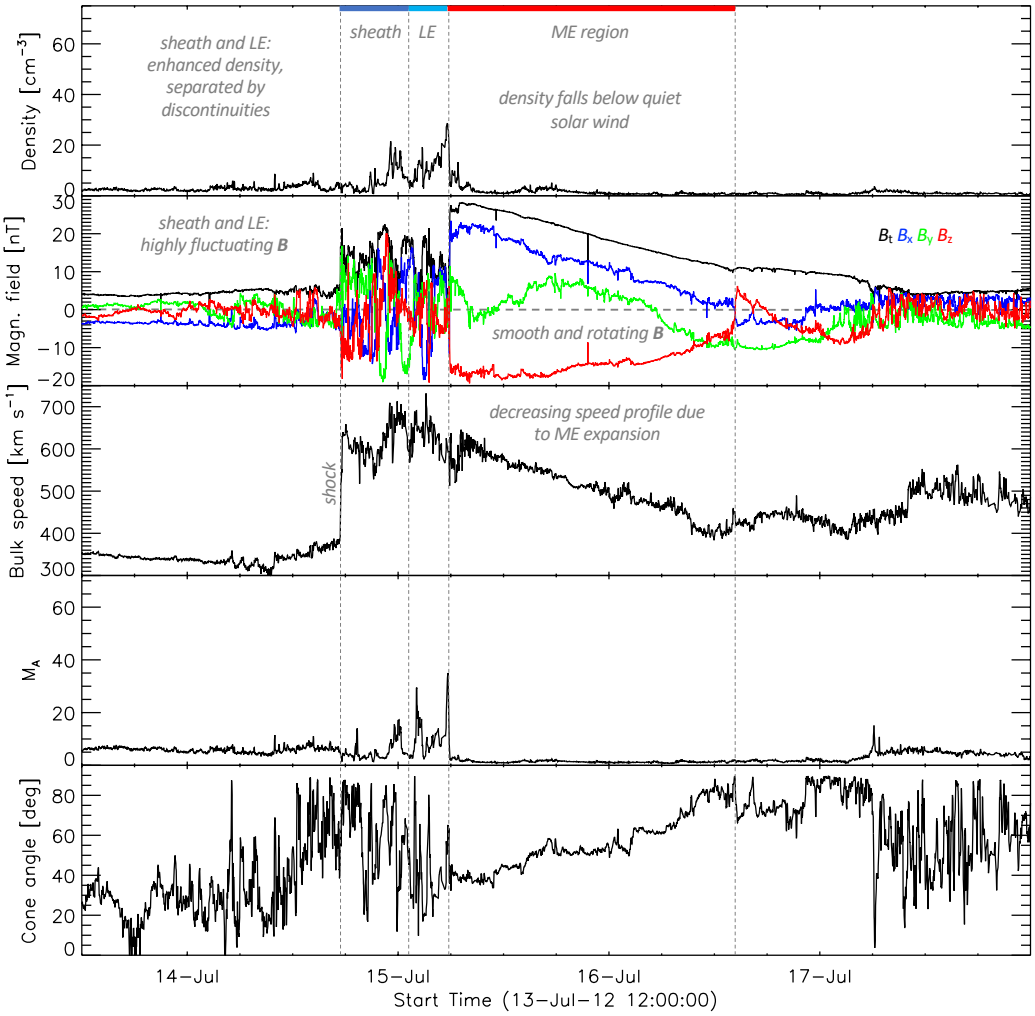

Fig. 2.1: Example in-situ measurements of a CME by ACE. The panels show (from top to bottom): ion density, magnetic field components, velocity, Alfvén Mach number, and IMF cone angle. This figure is reproduced from Koller et al. (2023).

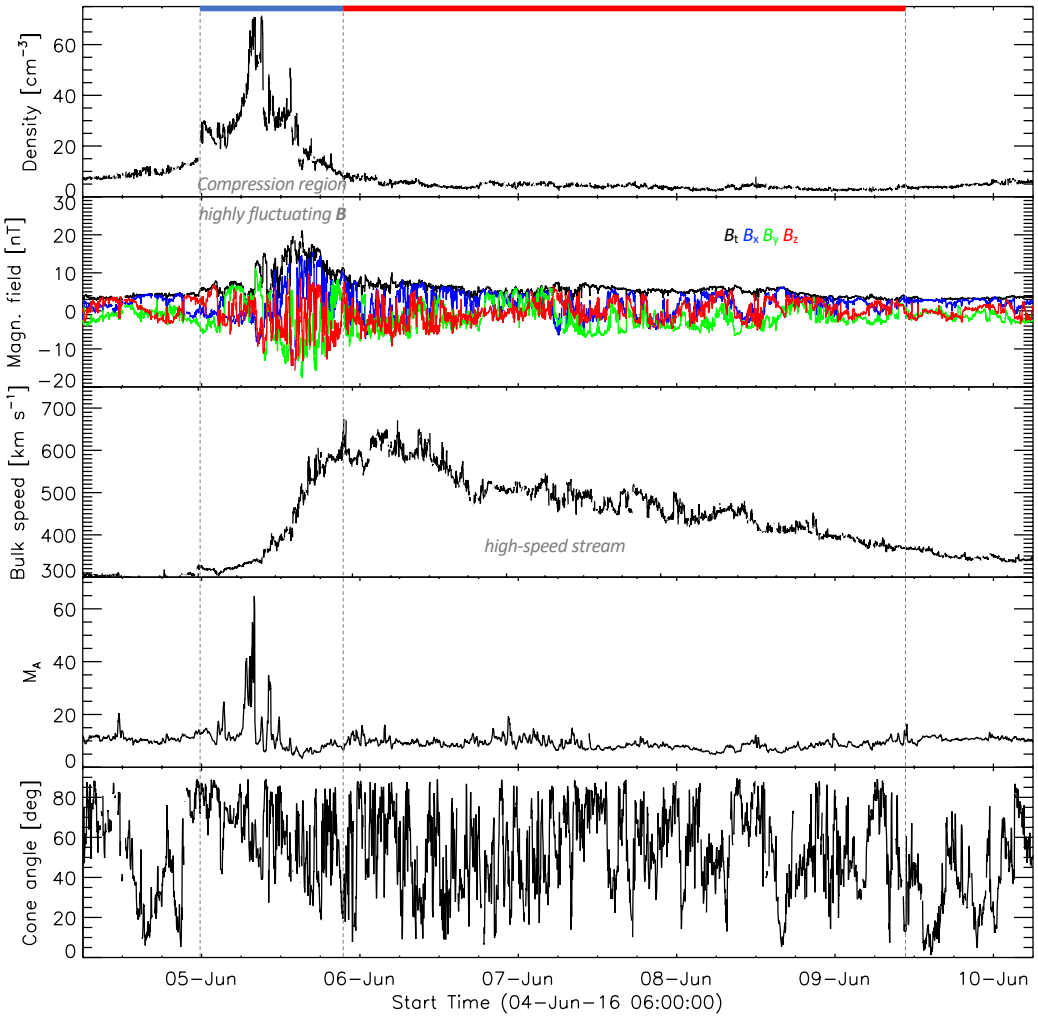

Fig. 2.2: Example in-situ measurements of an SIR by ACE. The panels show (from top to bottom): ion density, magnetic field components, velocity, Alfvén Mach number, and IMF cone angle. This figure is reproduced from Koller et al. (2023).

1999). Several works reclassify SIRs that persist over a full solar rotation as CIRs (e.g. Allen et al., 2021). SIRs at 1 AU can last for several days, averaging around 5 days (Koller et al., 2022). The front of an SIR can also cause a shock, which is more likely happening further outside the solar system, e.g. at Mars distance, than inside (Geyer et al., 2021).

The heliospheric current sheet (HCS) divides the interplanetary plasma in a region with radially outwards direction of magnetic field orientation and radially inward direction (Smith, 2001). Due to the Maxwell equations, a rotation in magnetic field orientation results in an electric current at the border. As a result, the HCS shapes the plasma as it can not mix with each other as dictated by the frozen-in condition. The HCS is spiral-shaped due to the solar rotation.

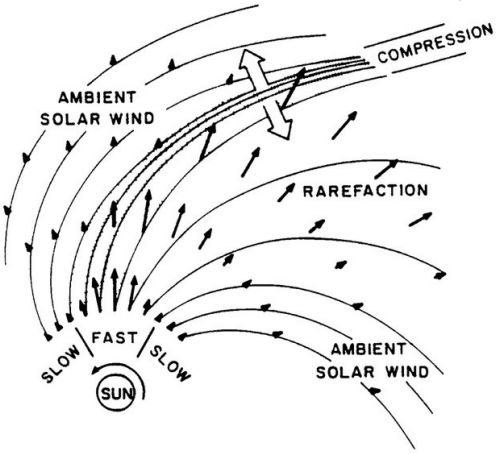

Fig. 2.3: Illustration of the formation of an SIR in interplanetary space, reproduced from Pizzo (1978).

Xu and Borovsky (2015) introduced a categorization of the solar wind plasma into four types based on their origin on the solar atmosphere. Some of these types overlap with the structures discussed above. The categorization of Xu and Borovsky (2015) is based on the proton specific entropy (defined as $S_p = T_p/n_p^{2/3}$), proton Alfvén speed, and proton temperature compared to the expected temperature at the given velocity. Their four categories are as follows: ejecta, coronal hole, sector reversal, and streamer belt.

The ejecta plasma type is closely correlated to CME structures (Xu and Borovsky, 2015). They have a high Alfvén velocity which results in low Alfvén Mach numbers. Plasma beta inside an ejecta is low, while the magnetic field strength is high. The proton temperature is low compared to the expected temperature, for which Xu and Borovsky (2015) used a velocity-dependent empirical power law. The IMF angle does not follow the expected Parker-spiral (Borovsky et al., 2019).

Coronal hole plasma shows a high proton specific entropy and has high velocities and high temperatures in in-situ measurements (Xu and Borovsky, 2015). The proton temperature follows an empirical velocity-dependent power law. The plasma also shows a low O^{7+}/O^{6+} ratio as well as a Parker spiral IMF (Xu and Borovsky, 2015; Borovsky et al., 2019). Notably, the Parker spiral is more radial at higher velocities, which is especially relevant for coronal hole plasma. The fluctuation of plasma parameters in this type is higher compared to the other 3 types of solar wind (Borovsky et al., 2019). This plasma is the origin of the aforementioned high-speed streams or fast solar wind in interplanetary space. The plasma emanates from open field lines in coronal holes, which manifests itself as dark regions in EUV images of the solar corona (Temmer, 2021). Therefore, detection of coronal holes in EUV

images are used to predict the occurrence of fast solar wind and SIRs at Earth (Heinemann et al., 2019; Milošić et al., 2023).

Sector reversal plasma is characterized by a low proton specific entropy and low Alfvén velocity (Xu and Borovsky, 2015). Their origin lies in the top of helmet streamers, which are magnetic loops in the solar corona separating coronal holes of opposite magnetic polarity. This is the reason why the magnetic field orientation reverses in this type of plasma and does not follow a Parker spiral orientation (Borovsky et al., 2019). Sector reversal plasma in in-situ measurements has low velocity and high Alfvén Mach numbers as well as a high O^{7+}/O^{6+} ratio (Xu and Borovsky, 2015).

Streamer belt plasma falls into intermediate ranges in the three parameter categorization by Xu and Borovsky (2015). This type shows low velocities and follows a Parker spiral IMF orientation (Borovsky et al., 2019). The origin of this plasma is thought to lie between coronal holes and helmet streamers or in the region separating two coronal holes of the same polarity (Xu and Borovsky, 2015). Both sector reversal and streamer belt plasma make up the so-called slow solar wind measured at 1 AU.

There have been efforts by Camporeale et al. (2017) to classify the OMNI dataset into the four categories based on machine learning. Their work includes probability measures to estimate how certain the classification of in-situ measurements are. The Xu and Borovsky (2015) classification notably does not consider more complex structures that can appear at 1 AU. While the high-speed streams of SIRs correlate with the coronal hole plasma, the compression region in front of it would fall into a mix of coronal hole plasma and streamer belt or sector reversal plasma. The sheath of a CME is usually weakly shocked slow solar wind and thus should have their origin in either the streamer belt or sector reversal region, however an erroneous classification into coronal hole plasma due to the high velocity or into ejecta plasma due to the strong magnetic field strength is also plausible. Interacting events can further complicate the classification. Overall, to fully describe the solar wind plasma at 1 AU one needs to take a detailed view on the origin of the plasma as well as structures that emerge in the flow.

2.2.2 Solar Cycle

The Sun exhibits an activity cycle of about 11 years (peak-to-peak) with increased flux and outburst of energetic events during the peak. The cycle is connected to the switch of magnetic polarity in the Sun's photosphere, which takes 22 years for a full switch back to the original polarity (called the Hale cycle). This whole process, the

solar dynamo, arises due to the differential rotation of the outer region of the Sun, the convection zone (Schrijver and Siscoe, 2009). The solar equator rotates faster than the polar region, causing the magnetic field lines (which are dragged with the plasma) to wind up and amplify. Regions of intense, strong magnetic fields form, and due to the balance of magnetic and thermal pressure, these regions appear less dense and less hot creating sunspots in the photosphere. The number of sunspots is therefore an indicator of the solar cycle and solar activity. These sunspot areas create active regions, which are especially visible in EUV images of the solar corona. Complex active regions regularly cause outbursts of radiation (flares) and mass (CMEs) by reconnection events. The solar cycle largely dictates which solar wind types and large-scale structures appear in the heliosphere (Hathaway, 2010). CMEs appear mostly during the maximum of the activity. Coronal holes usually appear at the poles of the Sun during quiet times, while they can appear all over the solar corona during times of higher activity. The number of coronal holes near the solar equator is especially heightened during the declining phase of the cycle. We refer to the living review by Hathaway (2010) for a detailed overview on the solar cycle.

2.3 Collisionless Plasma Shocks

The following section briefly covers collisionless shocks, for a detailed view we refer to Balogh and Treumann (2013) and Burgess and Scholer (2015). The solar wind at 1 AU has high velocity which is usually faster than the speed of waves within the plasma. Thus, the solar wind has high Mach numbers as it is super-Alfvénic, supersonic, or both (super-magnetosonic). A flow with high Mach number causes a shock when an obstacle is hit, as the plasma flow can not evade the obstacle in time. Such a shock, the so-called bow shock, is formed when the solar wind hits Earth's magnetic field. Space plasma shocks are purely collisionless, because the effect results form the magnetic and electric properties of the plasma, while the density of the medium is too low to allow for collisions of particles (in contrast to shocks in the Earth's atmosphere like sonic booms at airplanes). Collisionless shocks are ubiquitous and can be found all over the solar system and beyond. Every planet with an intrinsic magnetic field (like Mercury, Earth, Jupiter) has a bow shock due to the high Mach number solar wind. Unmagnetized or weakly magnetized objects like Venus and Mars or comets also have bow shocks, though much closer to their surface. In the case of Venus and Mars, the ionosphere and exosphere causes the obstacle to the incoming solar wind plasma (Tatrallyay et al., 1983; Bertucci et al., 2011). Mars also possesses a remnant magnetic field on the surface (Bertucci et al., 2011). In all above mentioned cases, the solar wind creates the shock due to its high velocity. The Alfvén Mach number for those shocks range from 3 to 20 or more, depending on the local solar wind conditions. However, shocks can also arise in the solar wind itself.

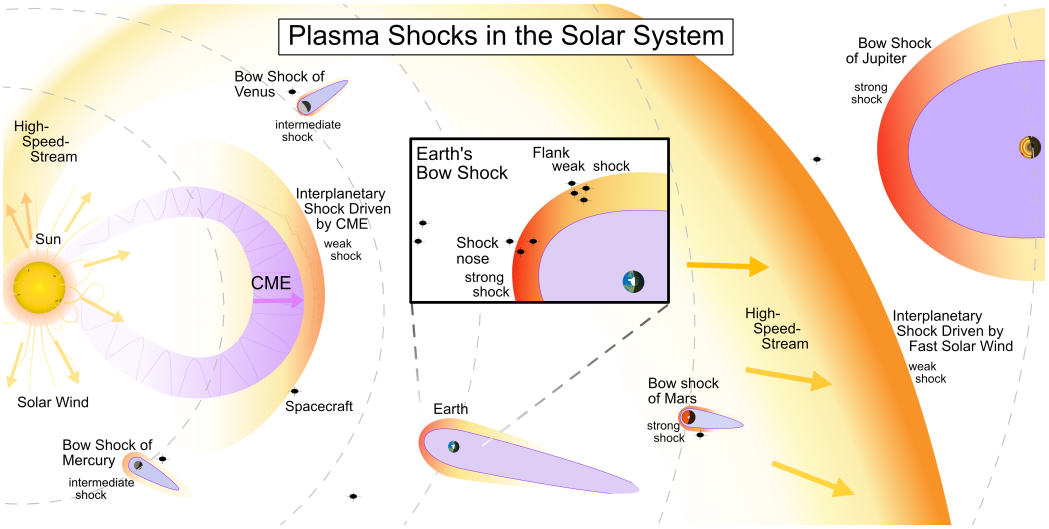

Fig. 2.4: Overview of shocks found in the inner solar system.

As was described in Section 2.2.1, fast CMEs can cause interplanetary shocks due to the collision with the slow solar wind in front of them. SIRs can also cause shocks, which are more prevalent further away from the Sun. The Alfvén Mach number of these shocks is lower compared to the planetary events, with usual values of 2 to 10. This is because the obstacle is embedded within the solar wind and has to greatly exceed the flow of the plasma in front of it. Figure 2.4 gives an overview of collisionless shocks found in the inner solar system, including shocks caused by large-scale solar wind structures.

The plasma undergoes rapid changes in its parameters at a collisionless shock. In particular, the velocity decreases to sub-Alfvénic and sub-magnetosonic speed and the particles heat up (thermalize) in the process. The density increases, which in turn also increases the magnetic field strength. The changes of plasma parameters between up- and downstream of a shock can be described by the Rankine-Hugoniot jump conditions. The subsequent Rankine-Hugoniot equations in ideal MHD (following Burgess and Scholer (2015)) use brackets $[...]$ to denote the difference of upstream and downstream conditions, thus $[x] = x_u - x_d$. The subscripts n and t denote normal and tangential to the shock surface, respectively. Vector quantities are marked in bold.

$$[\rho v_n] = 0 \tag{2.16}$$

$$\left[\rho v_n^2 + p + \frac{B^2}{2\mu_0}\right] = 0 \tag{2.17}$$

$$\left[\rho v_n \mathbf{v}_t - \frac{B_n \mathbf{B}_t}{\mu_0}\right] = 0 \tag{2.18}$$

$$\left[\rho v_n \left(\frac{v^2}{2} + \frac{\gamma}{\gamma - 1}\frac{P}{\rho} + \frac{v_n B^2}{\mu_0} - \mathbf{v}\cdot\mathbf{B}\frac{B_n}{\mu_0}\right)\right] = 0 \tag{2.19}$$

$$[v_n \mathbf{B}_t - B_n \mathbf{v}_t] = 0 \tag{2.20}$$

$$[B_n] = 0 \tag{2.21}$$

This set of equation describes the conservation of mass, momentum, and energy flow across discontinuities. A shock has a non-zero mass flow $\rho v_n \neq 0$ and results in a change in both density and normal velocity across the discontinuity (Burgess and Scholer, 2015). The full set of equations results in three solutions of MHD shocks connected to the three characteristic speeds (slow, Alfvén, and fast mode). The shock compression ratio is given as $r = \rho_d/\rho_u$. In the high Mach number limit this ratio approaches 4, thus the compression of plasma is limited independent of other quantities like the magnetic field. Upstream kinetic energy is converted to downstream thermal energy, therefore, intense plasma heating appears at strong Mach number shocks. Burgess and Scholer (2015) noted that solutions of the full conservation relations indicate that the high Mach number limit is approximately valid above values of 5 – 10. We want to note here that a fast magnetosonic shock Mach number can be described as a function of β_u, Θ_{Bn}, and M_A. Θ_{Bn} describes the IMF angle relative to the shock normal, which is equivalent to the cone angle at the subsolar point of the Earth's bow shock. Due to uncertainties in the Θ_{Bn} determination in observations it is most convenient to describe shock strengths using M_A (Burgess and Scholer, 2015). Jump condition solutions are dependent on the magnetic field angle with respect to the shock normal Θ_{Bn}. For strictly perpendicular shocks ($\Theta_{Bn} = 90°$) one finds that the magnetic field and density increase by the factor of r while the normal velocity decreases by the factor of r. In a strictly parallel case ($\Theta_{Bn} = 0°$), the compression ratio for the magnetic field strength is 1 and is therefore unaffected (hydrodynamical shock). Physical shocks are oblique cases, thus the magnetic field orientation and the velocity have arbitrary angles to the shock surface. The distinction into quasi-parallel and quasi-perpendicular shock based on Θ_{Bn} will further play an important role in the subsequent description.

As discussed in detail in Balogh and Treumann (2013) and Burgess and Scholer (2015), shocks have a critical Mach number. Solutions to the jump conditions above this value are not stable as they do not provide the necessary dissipation of incoming energy. Above this critical value the dissipation of energy by ion reflection becomes important, showing a qualitative change in collisionless shock behavior. Most heliospheric shocks are supercritical, which is why this effect is of high relevance as we will see in the following section.

2.3.1 The Foreshock

A supercritical shock gives rise to a secondary phenomenon: the so-called foreshock. At supercritical shocks, the shock can not take in and decelerate the particles to sub-Mach velocities at once, resulting in ions and electrons to get accelerated backwards upstream of the shock along magnetic field lines (Balogh and Treumann, 2013). For a detailed description of the physical processes we refer to the discussion of particle reflection and acceleration at shocks in Balogh and Treumann (2013). Reflected ions interact with the incoming particles, causing a deceleration of solar wind plasma ahead of the bow shock in the foreshock region. The 2D ion velocity distribution in the foreshock reveals the different ion populations in this region. The main component of the velocity distribution is always the bulk solar wind flow, visible as a clear and sharp beam moving anti-sunward. Close to the foreshock boundary one finds an additional field-aligned ion beam moving sunward, while deeper inside the foreshock one finds instead a diffuse ion ring distribution (Balogh and Treumann, 2013).

The co-existence of two ion populations carries a substantial amount of free energy, which is dissipated via excitation of waves and wave turbulence via instability (Balogh and Treumann, 2013). Burgess (1997) gave an overview of waves found in the foreshock. A large variety of Ultra low frequency (ULF) waves are found within the foreshock, with most frequently observed ULF waves being the 30 s, 10 s, 3 s and 1 s waves (Burgess, 1997; Eastwood et al., 2005; Zhang et al., 2022). Large-amplitude magnetic fluctuation or pulsations as well as steepened nonlinear ULF waves (called shocklets) appear therein (Zhang et al., 2022). Short large amplitude magnetic structures (SLAMS) are defined as magnetic enhancements of more than two times above the surrounding magnetic field (Schwartz et al., 1992; Zhang et al., 2022). Shocklets show the same behavior as SLAMS with lower amplitude and scale (see Zhang et al., 2022, for a discussion on the connection between SLAMS and shocklets). On can also find plasmoids showing an increase in density in the foreshock and mixed structures showing the behavior of both plasmoids and SLAMS (e.g. Xirogiannopoulou et al., 2024).

Several other structures also form in the foreshock, some of which we will briefly introduce: Foreshock bubbles (FBs) form when backstreaming ions hit a rotational discontinuity in the solar wind (Omidi et al., 2010; Zhang et al., 2022). Due to the change in magnetic field orientation, the particles get reflected and create a bubble that expands fast-magnetosonically (Omidi et al., 2010). Hot flow anomalies (HFAs) are driven by the intersection of tangential discontinuities in the solar wind with the bow shock and show a depletion of density and magnetic field strength in the core and a strong compression at the edges (Schwartz et al., 1985; Zhang et al.,

2022). They also show significant particle deflection and plasma heating, hence the name. Spontaneous hot flow anomalies (SHFAs) show a similar behavior however without being connected to discontinuities in the IMF (Zhang et al., 2013; Zhang et al., 2022). Foreshock cavities show a core region with low field strength and densities and compressional boundaries (Sibeck et al., 2002; Zhang et al., 2022). In contrast to HFAs, they only show little particle deflection and heating. Foreshock compressional boundaries (FCBs) form at the edge between the foreshock and the unperturbed solar wind and show an increase in density and magnetic field strength (Omidi et al., 2009; Zhang et al., 2022). In summary, the foreshock is a highly complex region with a barrage of waves and structures and still poses numerous open science questions.

Due to the high Mach number of the solar wind, all structures and waves that form in the foreshock are convected with the solar wind back to the shock where they interact with the shock surface itself. Foreshock structures themselves play an important part in the turbulent reformation (or non-stationarity) of the quasi-parallel shock front. Schwartz and Burgess (1991) proposed that SLAMS formed in the foreshock grow in amplitude and accumulate at the shock where they then form the new shock surface. As a result of that, the quasi-parallel shock surface is patchy, rippled, and irregular (see also Raptis et al., 2022a, for measurements of a shock reformation process).

Therefore, the presence of the foreshock changes the plasma downstream of the bow shock, dividing it into two different regions: the quasi-parallel and quasi-perpendicular magnetosheath. This division is governed by two parameters: the orientation of the IMF and the strength of the shock. A weak shock does not provide enough energy to accelerate particles back upstream and cause nonlinear foreshock structures. The naming of both regions is due to the magnetic field orientation being either (quasi-) parallel to the shock normal vector (IMF angle at shock surface $\theta_{Bn} < 45°$) or (quasi-) perpendicular to the shock normal vector ($\theta_{Bn} > 45°$). Figure 2.5 shows the dayside magnetosheath region including the ion foreshock and the quasi-parallel and quasi-perpendicular magnetosheath region. The wavy magnetic field lines at the quasi-parallel shock illustrate the turbulent plasma behavior.

The quasi-perpendicular shock has no foreshock structure, because all particles that are accelerated back upstream hit the shock again after gyrating once around their field line (Balogh and Treumann, 2013). This causes a non-gyrotropic (meaning that the plasma parameter are depending on the gyrophase) shock transition region. Because of the general higher parallel velocities of electrons compared to protons, the foreshock has a different front for each type of particle (Balogh and Treumann, 2013). We focus on the effects of the ion foreshock in all subsequent analysis.

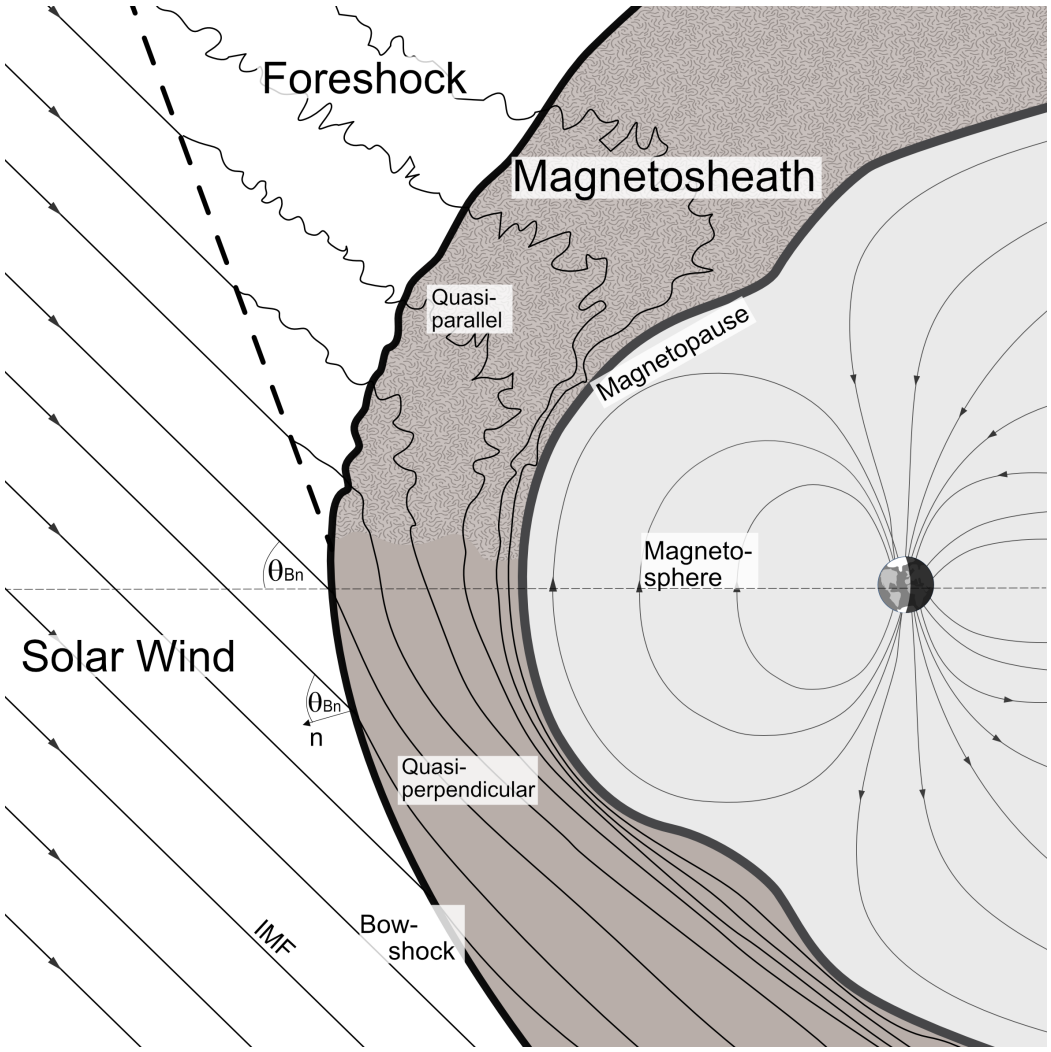

Fig. 2.5: Illustration of the foreshock, magnetosheath, and magnetosphere of the Earth.

2.3.2 The Magnetosheath

The following description is valid for all types of plasma downstream of collisionless shocks, however, the main focus is put on the terrestrial magnetosheath.

The magnetosheath, consisting of the shocked solar wind plasma, is bounded by the bow shock and the surface of the magnetopause. Depending on the solar wind conditions, it can be found between 10 – 18 earth radii (Re = 6371 km) sunward of the Earth. At the magnetopause, the plasma pressure of Earth's magnetic field equals the plasma pressure of the incoming particles, creating a boundary that is impenetrable for ideal MHD plasma. Thus, the magnetosheath plasma flows around the magnetosphere and joins the solar wind at sufficiently high distances away from the Earth again. As a result of this, the magnetosheath plasma is faster at the flanks and slower at the dayside of the shock (Dimmock and Nykyri, 2013).

The plasma downstream of the bow shock overall is decelerated to roughly sub-Alfvénic speeds with a 4 times increase in density and a substantial temperature increase. The magnetosheath plasma is subject to numerous effects such as instabilities and turbulent interactions. The behavior substantially changes close to the bow shock compared to the region close to the magnetopause. Certain plasma conditions can also cause local interactions with the terrestrial plasmasphere, like pressure-caused indentations of the magnetopause (Shue et al., 2009) or reconnection of field lines.

The subsolar magnetosheath can be easily identified in spacecraft data. Figure 2.6 shows an example of THEMIS A traversing the magnetosheath coming from the solar wind and ending up in the Earth's magnetosphere. The ion density (Figure 2.6 c)) in the magnetosheath is significantly higher compared to the solar wind and the magnetosphere and can therefore be used to detect magnetosheath intervals. The ion velocity (Figure 2.6 b)) in the solar wind is high and primarily anti-sunward directed. The outer magnetosphere on the other hand shows very low ion velocities. Magnetic field strength (Figure 2.6 a)) ranges from a view nT in the solar wind to tens of nT in the magnetosheath to up to 100 nT in the outer magnetosphere. The ion energy (Figure 2.6 f)) also is the lowest in the solar wind and the highest in the magnetosphere. The ion energy distribution is much broader in the magnetosheath. The solar wind shows a narrow energy distribution, while the magnetosphere shows a peak at the upper energy limit.

The local plasma conditions are different in the quasi-parallel and quasi-perpendicular sheath. In Figure 2.6 the times of excess energy around 10 keV indicate the presence of the foreshock region in the solar wind and quasi-parallel plasma in the

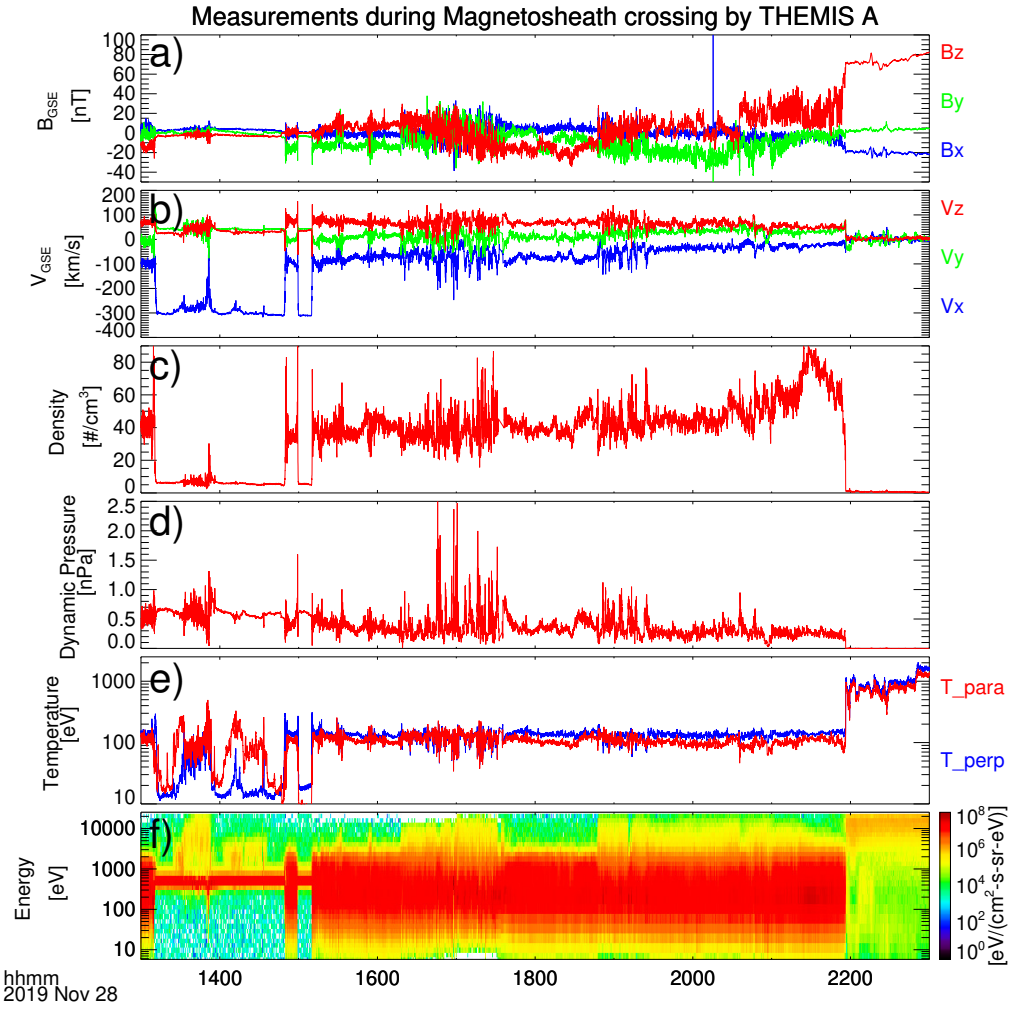

Fig. 2.6: Ten hours of THEMIS A measurements during the crossing of Earth's magnetosheath. The spacecraft is in the solar wind for almost two hours around 14:00 UT and again for a short time around 15:00 UT. The spacecraft crosses the magnetopause the Earth's magnetosphere around 22:00 UT. All other measurements show magnetosheath plasma. The panels show: a) magnetic field vector components, b) velocity vector components, c) ion density, d) dynamic pressure, e) ion temperature (parallel and perpendicular to the magnetic field), and f) the ion energy spectrum.

magnetosheath. The times of quasi-parallel magnetosheath plasma also show fluctuations in the magnetic field components, velocity components, and in the ion density. These conditions can be used to differentiate both regions (Karlsson et al., 2021). Several dynamic pressure peaks are visible which indicate magnetosheath jets (see Section 2.4). In addition to showing more jets, the quasi-parallel sheath is substantially more turbulent (Gurchumelia et al., 2022) and shows an increase of plasma sheet occurrences (Yordanova et al., 2020). This is all the result of the presence of the upstream foreshock. The quasi-perpendicular magnetosheath (which shows no excess energy distribution at 10 keV) on the other hand is less turbulent, but is prone to several plasma instabilities: The quasi-perpendicular shock causes ion temperature anisotropy (differences in the ion temperature along and perpendicular to the magnetic field line), because the perpendicular ions get heated more. This anisotropy can cause plasma instabilities, like the ion-cyclotron instability or the mirror mode instability (Verscharen et al., 2019).

The position of the bow shock and the magnetopause are governed by the solar wind parameter. Models for magnetopause and bow shock are used to provide the position and shape of the two surfaces. By using these, one can infer the relative position of a spacecraft traversing the magnetosheath. One of the frequently utilized magnetopause models is the one by (Shue et al., 1998). Bow shock models (e.g. Merka et al., 2005) are in general more complex than magnetopause models. Both types of models are usually based on empirical equations that use solar wind dynamic pressure and magnetic field orientation (B_z in particular). Some uncertainty of the positioning of a spacecraft in the magnetosheath is always in order, as the models can not perfectly predict the exact positions of the surfaces at all times.

2.4 Magnetosheath Jets

Magnetosheath jets are defined as dynamic pressure enhancements downstream of a shock, thus they either show an increase in velocity, density, or both in comparison to their surroundings. The first event of this type was reported by Němeček et al. (1998) calling them transient flux enhancements. The review by Plaschke et al. (2018) gives an overview of definitions and different names corresponding to these structures. The increasing data availability of the dayside magnetosheath by Cluster, THEMIS, and MMS led to the detection of numerous jets in the past decades (see datalist by e.g. Plaschke et al., 2013; Raptis et al., 2020; Koller et al., 2023; Pöppelwerth et al., 2024). Jets range from some seconds to some minutes in duration in in-situ measurements, which roughly corresponds to sizes of 0.1 up to several earth radii (Plaschke et al., 2020). The majority of jets are found within the quasi-parallel bow shock (Plaschke et al., 2013), while jets also have been reported

in the quasi-perpendicular region (Goncharov et al., 2020; Kajdič et al., 2021) and the boundary region between both (Raptis et al., 2020). Jets are found more often close to the bow shock than to the magnetopause (LaMoury et al., 2021). Jets have been reported to impact the magnetopause and cause measurable effects in the magnetosphere. While jets are primarily observed and studied in the terrestrial magnetosheath due to the availability of data, the occurrence of these events should be universal to collisionless shocks. Recently, Gunell et al. (2023) reported the first detection of jets in the martian magnetosheath using MAVEN data, Zhou et al. (2024) reported jet observations in the magnetosheath of Jupiter in Voyager data, and Hietala et al. (2024) reported the first jet-like candidates downstream of an interplanetary shock. Figure 2.7 shows a schematic of magnetosheath jets in the near-Earth plasma environment. The figure includes the subcategories of jet research which we will herein briefly review: the current theories in jet formation (Figure 2.7 panel a)), their occurrence based on solar wind parameters (indicated by the large-scale structure in the top left of Figure 2.7), an overview of jet properties as they move through the magnetosheath (Figure 2.7 panel b)), and the impact they have on the magnetospheric system (Figure 2.7 panel c)).

2.4.1 Jet Criteria

Before we can discuss the physics of jets we first need to clarify how jets are defined in the literature. The detection of jets is based on threshold imposed on the dynamic pressure of the magnetosheath. Several different criteria are used (see Plaschke et al., 2018, for an overview of previosly used criteria). The criterion introduced by Plaschke et al. (2013) is frequently used throughout the literature. They defined jets as follows:

$$p_{\mathrm{dyn,x}} > \frac{1}{2} p_{\mathrm{dyn,sw}} \tag{2.22}$$

where $p_{\mathrm{dyn,x}}$ denotes the magnetosheath dynamic pressure in GSE-X, and $p_{\mathrm{dyn,sw}}$ the SW dynamic pressure. The jet time range is defined as the time when $p_{\mathrm{dyn,x}}$ exceeds 1/4 of the SW dynamic pressure. Plaschke et al. (2013) also used secondary requirements: there must be data available in the minute before and after the jet and the velocity in GSE-X needs to be negative (earthward) and at least 2 times faster during the pressure peak in comparison to the magnetosheath flow one minute before and after the jet. This ensures that the jets are earthward moving and have a high velocity compared to the surrounding plasma. This criterion is only valid close to subsolar region, because the flow in the magnetosheath flanks is faster and thus fulfills the criterion at all times. What is also important to consider is that there is a velocity gradient in the magnetosheath with higher values close to the bow shock

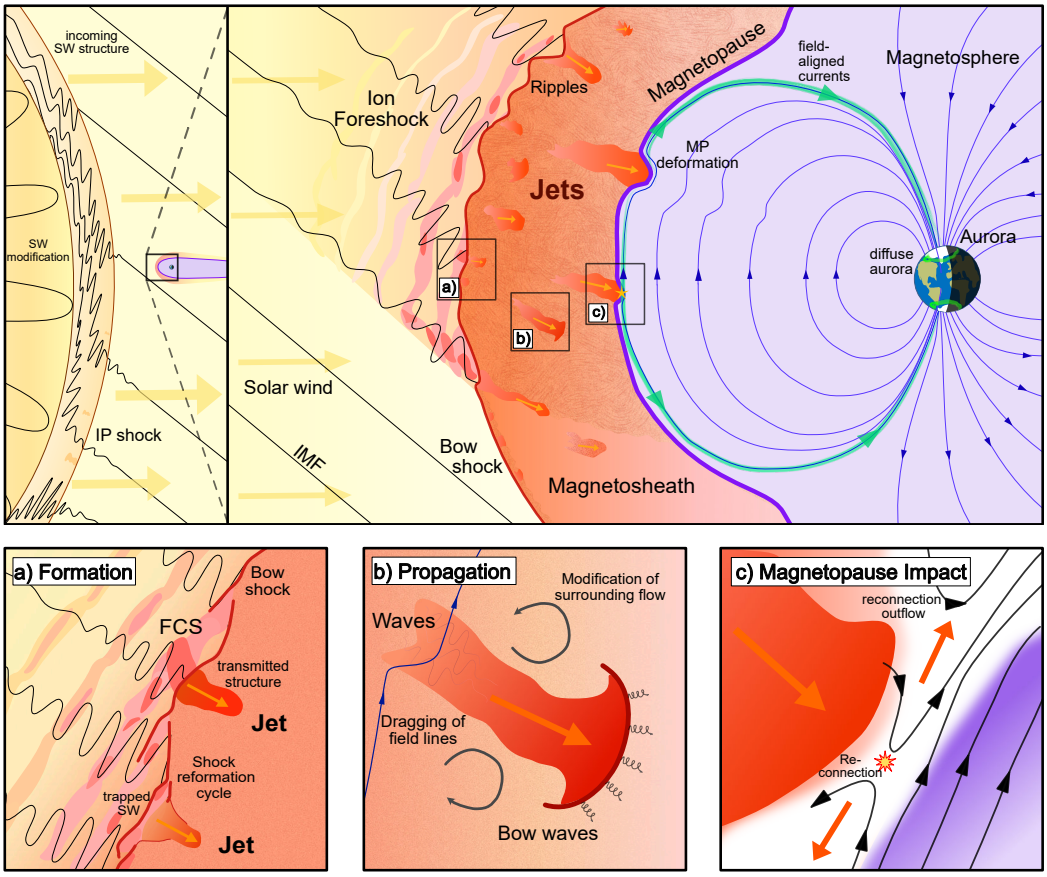

Fig. 2.7: Overview of magnetosheath jet research in full context. This schematic gives an overview of the dayside magnetosheath including jets as well as the formation (panel a)), propagation (panel b)), and magnetopause impact (panel c)) of jets. The panel on the left indicates incoming solar wind structures like interplanetary shocks. This schematic is reproduced from the review paper by Krämer et al. (in preparation).

and lower values close to the magnetopause, thus the criterion will naturally be more often fulfilled close to the shock.

The statistical analysis by Archer and Horbury (2013) employed the following criterion based on the local change in magnetosheath dynamic pressure:

$$\frac{\delta P_{dyn}}{\langle P_{dyn} \rangle} > 1. \tag{2.23}$$

Here, the angular brackets refer to a running average of the value, for which an averaging window of 20 minutes is used. Essentially, it means that the dynamic pressure must exceed two times the 20 minute averaged pressure. This criterion is much less strict than the one by Plaschke et al. (2013) and picks up more events. The criterion detects more jets close to the magnetopause than close to the bow shock. It appears to be less likely that an event close to the bow shock (where the dynamic pressure is the strongest) exceeds two times the surrounding pressure. Notably, this criterion also has no preference in velocity and direction, thus it can detect events that move in any direction (including sunward) and also slow events that are exceptionally dense.

Koller et al. (2022) employed the following criterion that is a mixture of both Plaschke et al. (2013) and Archer and Horbury (2013):

$$p_{dyn,x} > 3 \times \langle p_{dyn,x} \rangle_{20min}. \tag{2.24}$$

Here, the 20 minute averaged pressure in GSE-X must be exceeded 3 times. In addition to that, the velocity criteria from Plaschke et al. (2013) were also employed, resulting in fast, earthward directed jets. However, the dependence on upstream conditions is not given anymore in contrast to Plaschke et al. (2013). The reasoning for using this criterion is that Koller et al. (2022) analyzed the influence on solar wind structures, which often show sudden changes in the values. OMNI sometimes does not perfectly reflect the measurements at the magnetosheath (Walsh et al., 2019) and timing offsets due to spacecraft positions deep in the magnetosheath are not considered. Therefore, OMNI might not reflect the plasma measured at the spacecraft. Large-scale SW structures with sudden dynamic pressure changes would cause erroneous jet detection or jet omission in the detection algorithm due to the attached uncertainties. Koller et al. (2022) used local conditions only to avoid this additional cause for uncertainties.

2.4.2 Jet Formation

The formation of jets is subject to extensive current research. There are several theories on their formation, some of which might be connected and show different interpretations of the same processes.

Most jets appear in the quasi-parallel magnetosheath and close to the bow shock, therefore, a connection to the foreshock is a reasonable assumption. Hietala et al. (2009) introduced a possible formation mechanism based on bow shock ripples. Waves and compressive structures in the upstream foreshock integrate into the quasi-parallel shock (as part of the shock reformation mechanism), which causes the surface to show a patchy and rippled surface. The Rankine-Hugoniot relations show that plasma perpendicular to shock geometry gets decelerated more compared to the velocity parallel to the shock surface. Therefore, a shock showing large scale indentations can have regions where the fast solar wind can enter the shock without being significantly decelerated and thus causing a high-speed jet. Suni et al. (2021) and Suni et al. (2023) connected jet occurrence to upstream foreshock compressive structures (FCSs) themselves. They conducted an analysis on 2D global hybrid Vlasov simulations, where they report the formation of jets in the magnetosheath after FCSs impacted the shock surface. Direct confirmation of this process by spacecraft observation is challenging due to limitation by spacecraft orbits and inter-spacecraft distances. The work by Xirogiannopoulou et al. (2024) on foreshock transients is preparatory for confirming the jet-foreshock structure connection. Notably, FCSs can also cause ripples in the shock surface, therefore the connection to the ripple mechanism is also plausible. Raptis et al. (2022a) reported the formation of a magnetosheath jet as a consequence of the shock reformation itself. They used MMS measurements during a string-of-pearl formation where they tracked the position of the bow shock. The found a trapped patch of solar wind plasma between the previous shock surface and the newly formed surface further upstream. Thus, a region of plasma with higher velocity is confined in the magnetosheath plasma, fulfilling the definition of magnetosheath jets. The scale of this structure however is smaller than the medium size of jets reported in most of the literature. Preisser et al. (2020) report, based on 2D local hybrid simulation, the formation of a plasmoid in quasi-parallel shock region as a consequence of reconnecting plasma layers of opposite B-field orientation. This plasmoid had a self-consistent magnetic field inside with increased density but low velocity.

A small portion of jets were found to be linked to solar wind discontinuities moving through the magnetosheath, as reported by Archer et al. (2012). They describe these jets as being pressure pulses formed by the rapid change from quasi-parallel to quasi-perpendicular magnetosheath and vice versa. Zhou et al. (2023) showed

that an upstream discontinuity could cause a downstream jet by producing a HFA. Their proposed jet formation combines of both the ripple mechanism by Hietala et al. (2009) and the discontinuity mechanism by Archer et al. (2012). Some jets where found in the quasi-perpendicular magnetosheath, however, with clear properties of quasi-parallel sheath plasma (Raptis et al., 2020). These so-called "encapsulated" jets were interpreted as being formed in the quasi-parallel magnetosheath and migrated to the other plasma region. Kajdič et al. (2021) analyzed jets in the quasi-perpendicular region with different formation mechanisms, like flux tube connected to the quasi-parallel magnetosheath or reconnection exhausts at the magnetopause with jet-like signatures. Blanco-Cano et al. (2020), Blanco-Cano et al. (2023), and Kajdič et al. (2021) reported co-existing mirror modes and jets. Mirror modes might show parameters that can fulfill jet criteria due to the density enhancements within them.

Vuorinen et al. (2023a) also reported a population of jets that form entirely within the quasi-perpendicular transition region. These jets appear to be gyrobunched plasma enhancements and can not be found further away from the quasi-perpendicular shock.

2.4.3 Occurrence Based on Solar Wind Parameters

Solar wind parameter influence the occurrence of jets. Because most jets occur in the quasi-parallel magnetosheath and therefore require the building of the foreshock region, the most important parameter governing the jet formation in the subsolar magnetosheath is the IMF angle relative to the shock normal Θ_{Bn}. This angle is equivalent to the cone angle at the bow shock nose, which is why the cone angle is often used as a substitute for Θ_{Bn} in the subsolar region (which avoids the need to use bow shock models for shock curvature estimations). Vuorinen et al. (2019) report a 9 times higher occurrence of jets at low cone angles compared to high cone angles. This relation was confirmed several times (e.g. Plaschke et al., 2013; Goncharov et al., 2020; LaMoury et al., 2021; Koller et al., 2023), while other solar wind parameter play a lesser role. However, their influence have been investigated in detail in the past years as well. LaMoury et al. (2021) reported that the number of jets slightly increases at lower solar wind densities. The solar wind dynamic pressure does not appear to significantly influence the jet occurrence. They also discovered that solar wind properties can impact the formation and propagation of jets differently: jets formed under high solar wind velocities and strong IMF strength have a higher likelihood of hitting the magnetopause. This suggests that jet formation analysis based on solar wind conditions can include biases due to jets that survive longer while traversing the magnetosheath. Vuorinen et al. (2023a) further investigated jet formation close to the bow shock in the low and high cone

angle regime. They showed that a minimum value of 0.5 for β and 5 for M_A is necessary for the onset of jet formation. The occurrence of jets in the quasi-parallel (or low cone angle) region does not appear to be significantly modified by any other parameters as long as β and M_A is sufficiently large. The jet formation in the quasi-perpendicular region showed dependencies on other parameters as well. The number of jets increases in low solar wind density, low magnetic field strength, high β, and high M_A. These jets appear to be mainly part of the quasi-perpendicular shock transition region and do not show up further in the magnetosheath. Tinoco-Arenas et al. (2022) used 2D local hybrid simulations to examine jet properties under different Θ_{Bn} angles and M_A values. The production of jets ceased for simulation runs with $\Theta_{Bn} = 65°$. Jet occurrence correlated positively with Mach number and $\Theta_{Bn} \leq 45°$.

The results by Koller et al. (2022) and Koller et al. (2023) showcased in this thesis analyze the influence of jet occurrence by solar wind structures. Large-scale events like CMEs or SIRs restrict the solar wind parameter space to a certain combination of values. CMEs for example usually cause high magnetic field strengths, low M_A, low β, high cone angles and low densities. High-speed streams on the other hand are defined by their high velocities and often show low densities, low magnetic field strength, and low cone angles. Koller et al. (2022) (see Chapter 3) showed that CMEs and the driven sheath in front of fast CMEs cause a reduction in jet occurrence. High-speed streams in SIRs cause an increase in jet occurrence. The follow-up study by Koller et al. (2023) (see Chapter 4) analyzed the dependence of jet occurrence on solar wind parameters in more detail. The combination of high cone angles and low M_A cause the reduction of jets in CMEs. The strong magnetic field strength in CMEs cause a decrease in β and in Mach numbers (following Equations 2.12, 2.13, and 2.14). High-speed streams have a higher likelihood of showing low cone angles, which causes the expected increase in jets. The high velocity is also often anti-correlated with density, which are both favorable for jet formation. The general correlation of parameters in the solar wind were also investigated by Koller et al. (2023).

The solar wind structure influence results by Koller et al. (2022) and Koller et al. (2023) motivated a study by Vuorinen et al. (2023b) on the long term effects of jet formation caused by the solar cycle. They used THEMIS and OMNI measurements over solar cycle 24 to infer, whether the change of solar wind parameters due to structured solar wind can significantly influence jet occurrence over a solar cycle. They quickly noticed that the measurements are heavily biased by spacecraft orbits and their apogee. Jets are more often observed close to the bow shock, therefore, years with low apogee orbits observed less jets. To tackle this issue, Vuorinen et al. (2023b) only considered jets close to the bow shock, which should correspond better to the formation mechanism as suggested by LaMoury et al. (2021). To get an

unbiased view of long-term jet formation, they constructed an empirical model that estimates jet occurrence based on solar wind input parameter. The rich database was used to construct this model to connect a jet occurrence estimation value to every combination of input parameters. This model was then checked using test samples. Vuorinen et al. (2023b) then applied this model to the entire solar cycles 23 and 24. The best fitting jet occurrence model uses the IMF cone angle and the IMF magnitude as data input. They found that the jet formation changes only little within a solar cycle, with a maximum decrease of 10 – 20 % at solar maximum, most likely due to increased CME occurrence. However, this is also within the range of error of the occurrence estimation model.

2.4.4 Jet Properties

The properties of the plasma connected to magnetosheath jets cover a wide range and are dependent on the criterion. Based on the criteria given in Equations 2.22, 2.23, and 2.24, jets show by definition an increase in dynamic pressure. The statistical parameter study by Plaschke et al. (2013) showed that the maximum dynamic pressure had increases up to 25 times stronger than the surrounding plasma. 89 % of their high-speed jets showed an increase in density as well. About 14 % of jets in the subsolar region are reported to be super-magnetosonic (Plaschke et al., 2013) and can therefore also create local shock fronts and shock particle acceleration (Hietala et al., 2009; Hietala et al., 2012; Liu et al., 2019; Liu et al., 2020b; Liu et al., 2020a; Vuorinen et al., 2022). Jets can show either increase, decrease, or steady magnetic field strength inside compared to the surrounding plasma. Jets that show an increase in density only are more often connected to increases of magnetic field strength as well (Archer and Horbury, 2013) and fulfill the description of paramagnetic plasmoids described by Karlsson et al. (2012). Karlsson et al. (2015) argue that these plasmoids make up a subset of magnetosheath jets. Archer and Horbury (2013) note that some jets which show a decrease in density could be associated to flux transfer events (FTEs) caused by reconnection at the magnetopause. These events would show velocities close to the Alfvén speed and increases in both magnetic field strength and temperature. The plasma temperature inside jets in general is often lower compare to the surrounding plasma (Plaschke et al., 2018). This hints at a formation mechanism where plasma gets less thermalized. Blanco-Cano et al. (2020) analyzed different jests in detail, where they showed that analyzing the velocity distribution function and temperature anisotropy in jets can help to infer details on their formation. Raptis et al. (2022b) reported jets that consist of two different plasma populations: the fast and cold jet plasma more akin to SW plasma and the slow, hot magnetosheath plasma. Notably, such a mix would render average jet values and measurements based on the assumption of a single Maxwellian velocity distribution inaccurate. The size of jets can reach up to several Re, while Plaschke

et al. (2020) determined a typical size of 0.1 Re. The morphology of jets is still under discussion within the community.

Figure 2.8 shows an example of a jet at 01:37:45 UT in THEMIS A data. This jet fulfills the Plaschke et al. (2013) criterion as can be seen in panel e). The duration of the jet is about 30 s and is caused by an increase in both density and earthward velocity. Panel f) shows the significant decrease of temperature inside the jet. The jet enhancement also caused an intensity peak in the ion energy spectrum (panel g)). The second dynamic pressure increase at 01:39:30 UT does not fulfill the Plaschke criterion, however it still shows the same behavior.

2.4.5 Jet Impact on the Magnetospheric System

The focus of this thesis lies on the solar wind influence on the magnetosheath and specifically on jets. Herein we will briefly review how jets can be geoeffective and influence the magnetospheric system, which underscores the importance of understanding jet formation. This helps us understanding the chain of events from solar wind to the Earth's magnetic field as well as effects on the ground.

The impact of jets on the magnetopause can cause secondary effects, some of which have been studied only recently. Jets can influence the reconnection mechanism at the dayside magnetopause, as was shown in a case study by Hietala et al. (2018). Using multiple THEMIS spacecraft, they investigated a jet impacting the magnetopause followed by reconnection outflows from the location of impact. They suggested that the dynamic pressure of the jet compressed the local current sheet, causing the onset of reconnection at the magnetopause. Vuorinen et al. (2021) found that jets are more likely to show magnetic field orientation including the opposite Bz orientation in comparison to non-jet magnetosheath flows. This means that even during northward Bz (which is usually non-reconnecting with the dayside magnetopause), an incoming jet can bring in negative Bz pulses. Thus, jets might trigger reconnection in times of northward Bz, while on the other hand they might also suppress reconnection in times of negative Bz. Ng et al. (2021) reported bursty-like reconnection caused by impacting jets in 3D simulations. While these studies refer to local effects at the magnetopause, the possibility of jets affecting the larger, global geospheric system was also considered. Nykyri et al. (2019) conducted a multi-spacecraft case study of a geomagnetic substorm which supposedly was triggered by an impacting magnetosheath jet. The jet in their study provided negative Bz pulses during times of northward IMF, which, as Nykyri et al. (2019) suggested, caused reconnection at the magnetopause and consequently flux loading in the magnetotail. Afterwards magnetotail reconnection started, causing a geomagnetic substorm.

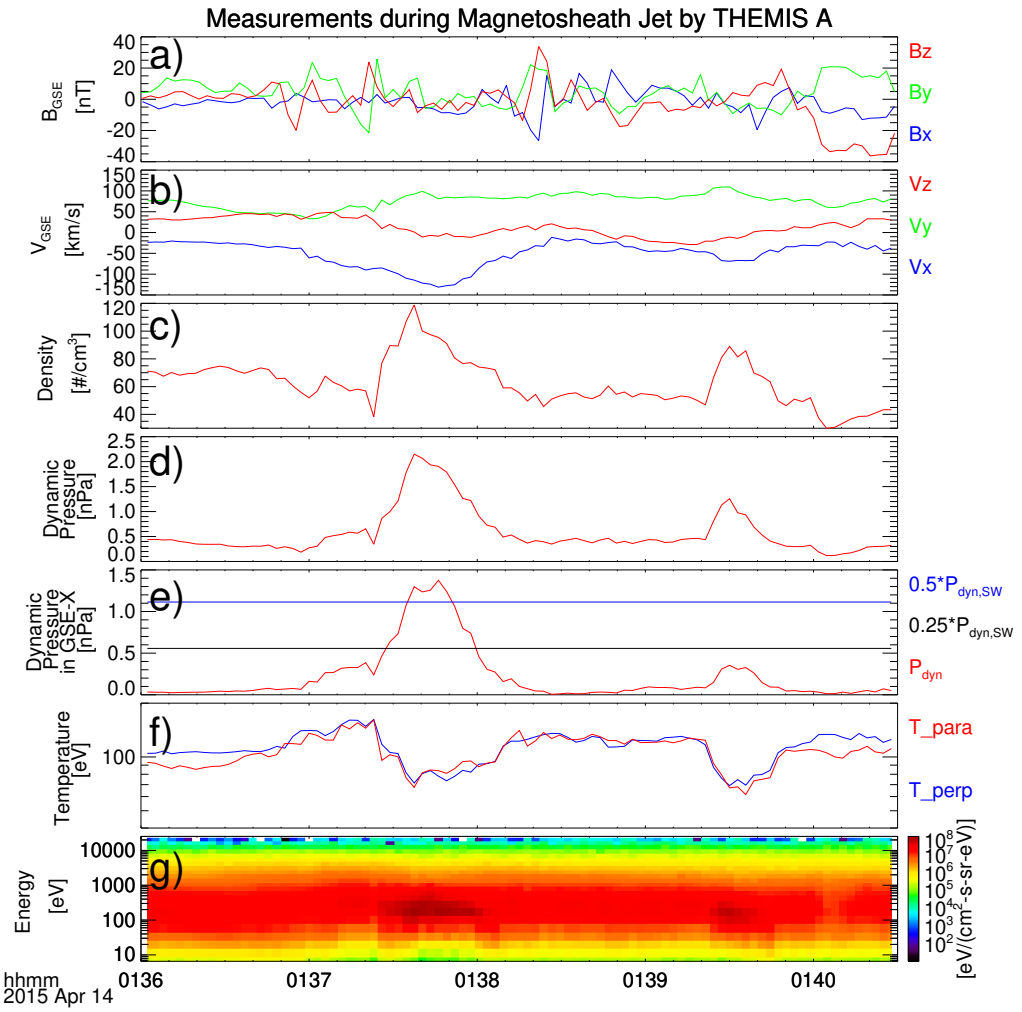

Fig. 2.8: Example of a magnetosheath jet in 4.5 minutes of THEMIS A data. The spacecraft is in the solar wind for almost two hours around 14:00 UT and again for a short time around 15:00 UT. The spacecraft crosses the magnetopause the Earth's magnetosphere around 22:00 UT. All other measurements show magnetosheath plasma. The panels show: a) magnetic field vector components, b) velocity vector components, c) ion density, d) dynamic pressure, e) dynamic pressure in GSE-X direction including the Plaschke criterion thresholds, f) ion temperature (parallel and perpendicular to the magnetic field), and g) the ion energy spectrum.

Localized compression of the magnetopause also have effects besides their influence on reconnection. Shue et al. (2009) reported wave-like motions of the magnetopause and sunward sheath plasma flow after a fast flow in the magnetosheath (equivalent to high-speed jets) hit the magnetopause. Archer et al. (2019) showed that impinging jets can cause the excitation of a surface wave eigenmode of the magnetopause. Effects can also be traced down to the Earth's surface. Magnetometers on the ground on Earth at high latitudes can measure disturbances induced by the impacts of jets at the magnetopause as reported by Norenius et al. (2021). In principal, one can measure magnetic field oscillations (Alfvénic waves) in the field lines that connect the ground with the position of jet impact at the magnetopause. Wang et al. (2022) investigated this effect in more detail. They found that several back-to-back impacting jets cause a stronger response in ground magnetometers in contrast to one single jet event. Strong jets might also impact geomagnetic indices as well as causing strong suprathermal ion precipitation (affecting ionization in the upper atmosphere) as was shown by Dmitriev and Suvorova (2023). They suggested that these ionospheric enhancements might influence radio communication and navigation. Jet-induced localized magnetopause indentations also were reported to cause auroral brightening. Discrete auroras (showing clear boundaries and intense luminosity) at the equatorward magnetic local noon edge correspond to the open-closed field lines of the magnetopause and magnetosheath (Han et al., 2018). Thus, mapping the magnetic field lines through these auroral regions should directly reflect effects at the magnetopause boundary. Han et al. (2018) reported evidence of discrete aurora caused by magnetopause indentation (which was measured by MMS). They considered that impacting jets caused these indentations, which in turn caused the auroral response towards lower latitudes (which they defined as throat aurora). Wang et al. (2018) used simultaneous measurements of THEMIS in magnetosheath, magnetosphere, and all-sky imager (ASI) data at the south pole. They could connect magnetosheath jets and their impact with responses in the magnetosphere and brightening in the discrete and diffuse aurora by ASI. They argue that impacting jets cause ULF waves and field-aligned currents in the magnetic field lines, which then cause the ionospheric response in the auroral imaging.

Paper 1

3

Magnetosheath Jet Occurrence Rate in Relation to CMEs and SIRs

Florian Koller[1] , Manuela Temmer[1] , Luis Preisser[2] , Ferdinand Plaschke[3] , Paul Geyer[1,4] , Lan K. Jian[5] , Owen W. Roberts[2] , Heli Hietala [6] , and Adrian T. LaMoury[6]

[1] Institute of Physics, University of Graz, Graz, Austria
[2] Space Research Institute, Austrian Academy of Sciences, Graz, Austria
[3] Institut für Geophysik und extraterrestrische Physik, TU Braunschweig, Braunschweig, Germany
[4] Hvar Observatory, Faculty of Geodesy, University of Zagreb, Zagreb, Croatia
[5] Heliophysics Science Division, NASA Goddard Space Flight Center, Greenbelt, MD, USA
[6] The Blackett Laboratory, Imperial College London, London, UK

The following article is published in the Journal of Geophysical Research: Space Physics, Volume 127, Issue 4, article id. e2021JA030124 (2022). The pdf document is available in the online version of this journal and embedded one-to-one in this thesis. My own contribution to this work was 80%.

JGR Space Physics

RESEARCH ARTICLE
10.1029/2021JA030124

Magnetosheath Jet Occurrence Rate in Relation to CMEs and SIRs

Florian Koller[1], Manuela Temmer[1], Luis Preisser[2], Ferdinand Plaschke[3], Paul Geyer[1,4], Lan K. Jian[5], Owen W. Roberts[2], Heli Hietala[6], and Adrian T. LaMoury[6]

[1]Institute of Physics, University of Graz, Graz, Austria, [2]Space Research Institute, Austrian Academy of Sciences, Graz, Austria, [3]Institut für Geophysik und extraterrestrische Physik, TU Braunschweig, Braunschweig, Germany, [4]Hvar Observatory, Faculty of Geodesy, University of Zagreb, Zagreb, Croatia, [5]Heliophysics Science Division, NASA Goddard Space Flight Center, Greenbelt, MD, USA, [6]The Blackett Laboratory, Imperial College London, London, UK

Key Points:

- Occurrence rate of magnetosheath jets is found to vary due to the arriving CMEs and SIRs
- Fewer jets are found when magnetic ejecta regions of CMEs hit the Earth, more jets are found when SIRs and high speed streams hit the Earth
- The jet duration does not appear to vary much during individual SW structures

Correspondence to:

F. Koller,
florian.koller@uni-graz.at

Citation:

Koller, F., Temmer, M., Preisser, L., Plaschke, F., Geyer, P., Jian, L. K., et al. (2022). Magnetosheath jet occurrence rate in relation to CMEs and SIRs. *Journal of Geophysical Research: Space Physics*, *127*, e2021JA030124. https://doi.org/10.1029/2021JA030124

Received 15 NOV 2021
Accepted 23 MAR 2022

Author Contributions:

Conceptualization: Manuela Temmer, Luis Preisser, Ferdinand Plaschke
Data curation: Ferdinand Plaschke, Lan K. Jian, Adrian T. LaMoury
Funding acquisition: Manuela Temmer, Ferdinand Plaschke
Methodology: Manuela Temmer, Luis Preisser, Ferdinand Plaschke, Paul Geyer
Project Administration: Manuela Temmer, Ferdinand Plaschke
Resources: Luis Preisser, Ferdinand Plaschke, Lan K. Jian
Software: Paul Geyer, Adrian T. LaMoury
Supervision: Manuela Temmer, Ferdinand Plaschke, Owen W. Roberts
Writing – original draft: Manuela Temmer
Writing – review & editing: Manuela Temmer, Luis Preisser, Ferdinand Plaschke, Paul Geyer, Lan K. Jian, Owen W. Roberts, Heli Hietala, Adrian T. LaMoury

Abstract Magnetosheath jets constitute a significant coupling effect between the solar wind (SW) and the magnetosphere of the Earth. In order to investigate the effects and forecasting of these jets, we present the first-ever statistical study of the jet production during large-scale SW structures like coronal mass ejections (CMEs), stream interaction regions (SIRs) and high speed streams (HSSs). Magnetosheath data from Time History of Events and Macroscale Interactions during Substorms (THEMIS) spacecraft between January 2008 and December 2020 serve as measurement source for jet detection. Two different jet definitions were used to rule out statistical biases induced by our jet detection method. For the CME and SIR + HSS lists, we used lists provided by literature and expanded on incomplete lists using OMNI data to cover the time range of May 1996 to December 2020. We find that the number and total time of observed jets decrease when CME-sheaths hit the Earth. The number of jets is lower throughout the passing of the CME-magnetic ejecta (ME) and recovers quickly afterward. On the other hand, the number of jets increases during SIR and HSS phases. We discuss a few possibilities to explain these statistical results.

1. Introduction

The solar wind (SW) is a continuous outflow of plasma and magnetic field from the Sun. The Earth's magnetic field is an obstacle to that SW. The SW is both supersonic and super-Alfvénic at 1 AU. This causes the formation of a permanent standing shock wave in front of the Earth, called the bow shock where the SW is slowed down, compressed, and heated. It further evolves downstream over the magnetosheath and its inner boundary, the magnetopause, which is the dividing boundary between the Earth's magnetic field and the interplanetary magnetic field (IMF). Hence, the dynamics of the magnetosheath vary under different SW conditions (e.g., Samsonov et al., 2007; Spreiter et al., 1966).

Structures disrupting that continuous SW severely impact the bow shock and magnetopause standoff distances (Baumjohann & Treumann, 1996; Tátrallyay et al., 2012). The SW is regularly disturbed by large-scale structures, such as stream interaction regions (SIRs) or transient events like coronal mass ejections (CMEs). SIRs are produced by the interaction between slow and high speed streams (HSSs). The fast stream often originated in open-field coronal holes compresses the slow wind stream in front of it. This results in a compression region, where the density and total pressure increase sharply (Jian et al., 2006a). The velocity increases continuously throughout the SIR and peaks within the HSS. SIRs may periodically recur due to the Sun's rotation, which is then called a co-rotating interaction region (CIR, Smith & Wolfe, 1976; Richardson & Cane, 2010). Other large-scale SW structures are coronal mass ejections (CMEs), which are transient events propagating in the SW. SIRs typically present sheath-like regions of compressed plasma and magnetic field. CMEs reveal a strong magnetic field region showing a rotating pattern in the magnetic field vector. We refer to this inner part of a CME as magnetic ejecta (ME; see e.g., Rouillard, 2011; Temmer, 2021). Because CMEs are often faster than the surrounding SW plasma, they can form a shock and drive an associated CME-sheath region (Good et al., 2019; Kilpua et al., 2017). Typically, the energy input and the effects on Earth's magnetosphere are dominated by CMEs, especially during phases of high solar activity. On the other hand, during solar minimum and declining phase, long lived CIRs and their HSSs may continuously interact with the Earth (Tsurutani et al., 2006).

In this study, we focus on the interaction of these large-scale SW structures with the bow shock and the magnetosheath region. Both CMEs and SIRs can compress the magnetosphere significantly due to extreme values

of specific SW parameters. In particular, the SW dynamic pressure and the southward component of the IMF largely determine the standoff distance of the magnetopause (Chapman & Bartels, 1940; Fairfield, 1971; Shue et al., 1998). At the magnetopause, the dynamic pressure of the SW is equal to the magnetic pressure of the Earth's magnetic field. The place of the magnetopause is therefore a consequence of the interplay between magnetic and dynamic pressure at both sides. Large southward magnetic field values can decrease the standoff distance by reconnection processes with the Earth's day-side magnetic field (Baumjohann & Treumann, 1996). This component is therefore considered the main driver of geoeffective interaction between the SW and the Earth's magnetic field. CMEs, SIRs, and HSSs are major sources for large southward magnetic field values (Richardson, 2018; Wu & Lepping, 2002).

While CMEs, SIRs, and HSSs arrive frequently at the magnetosheath region, they are rather sporadic events compared to so-called magnetosheath jets. First detected in 1998 (Němeček et al., 1998), magnetosheath jets are dynamic pressure enhancements traveling downstream of the bow shock toward the Earth's magnetopause. Different names have been assigned to the same or similar phenomenon, including: transient flux enhancement (Němeček et al., 1998), supermagnetosonic jets (Hietala et al., 2012), dynamic pressure pulses (Archer et al., 2012), high-speed jets (Plaschke et al., 2013), plasmoids (Karlsson et al., 2015), and supermagnetosonic plasma stream (Savin et al., 2014). While there are differences between each definition, they all share common properties. They either describe an enhancement in the velocity, density, or both within the Earth's magnetosheath. There is ongoing research about the origins of these jets and several generation mechanisms have been proposed, mainly involving processes at the bow shock (see Hietala et al. (2012); Karlsson et al. (2015); Preisser et al. (2020) or a review of the proposed mechanisms in Plaschke et al. (2018)). There is the consensus that the jets primarily appear downstream of the quasi-parallel bow shock (Archer & Horbury, 2013; Plaschke et al., 2013; Raptis et al., 2020; Vuorinen et al., 2019). There is evidence that magnetosheath jets significantly influence the magnetopause and cause geomagnetic substorms in Earth's magnetosphere (Hietala et al., 2018; Norenius et al., 2021; Nykyri et al., 2019; Wang et al., 2018). Magnetosheath jets are therefore an important link between the SW and the magnetopause. Large-scale SW structures and magnetosheath jets can be geoeffective on their own. It is therefore of great interest to learn how these effects are linked with each other.

There have been recent efforts to analyze the general favorable conditions for jet production using statistics of numerous jets (Archer & Horbury, 2013; Karlsson et al., 2015; LaMoury et al., 2021; Plaschke et al., 2013). In particular, LaMoury et al. (2021) concluded that favorable conditions for jet formation include low IMF cone angles, both slow and fast SW speeds, low magnetic field strength, high plasma-β, low dynamic pressure, high Alfvén Mach number, and low density. They found that jets are more likely to survive the propagation through the magnetosheath with SW conditions showing low IMF cone angle, high SW speed, high IMF magnitude, low plasma-β, and high dynamic pressure. This suggests that HSSs may have favorable SW conditions for jets, while the net effect of SIRs and CMEs cannot be deduced without dedicated research. Overall, the general relationship of jets with SW structures like SIRs, HSSs, and CMEs remain so far unexplored.

This work aims to reveal how these specific large-scale SW structures influence the occurrence rate of magnetosheath jets. We perform a thorough statistical analysis using the overlapping times of magnetosheath observations and times of CMEs/SIRs hitting the Earth to fulfill this goal. We use magnetosheath data from Time History of Events and Macroscale Interactions during Substorms (THEMIS) spacecraft between January 2008 and December 2020. For the CME and SIR + HSS list, we use lists provided by literature and expanded on incomplete lists using OMNI data to cover the same time range. In addition, we check the robustness of our results by using two different methods for the automatized detection of magnetosheath jets.

2. Data and Methods

2.1. CME and SIR Data

In this study we use several different lists of large-scale SW structures. We unified those lists to seamlessly cover the time range May 1996–31 December 2020.

For CMEs we use the list maintained by Richardson and Cane (Cane & Richardson, 2003; Richardson & Cane, 2010), which includes information of CMEs since 1996. It contains, among other information, start and end times for CME-ME. It also contains the start times of corresponding CME-shocks if one is present. We define the time between shock arrival and start of the magnetic ejecta as the CME-sheath crossing time. The start time

Table 1
Mean Durations for SW Events

	Time length (hours)			
	SIR + HSS	CME-sheath	CME-sheath + ME	CME-ME (all)
Minimum	16.2	0.7	7.0	6.0
Median	87.0	10.0	33.0	20.0
Mean	100.4	10.7	36.9	23.4
Maximum	288.0	22.7	73.8	58.0

Note. Only events that are overlapping with THEMIS magnetosheath data are used.

of the shock is defined as the time of associated geomagnetic storm sudden commencement in this list. The magnetic ejecta times are the times measured by the Active Composition Explorer (ACE, Stone et al., 1998). We briefly discuss timing issues due to measurements at L1 and the Earth in Section 4.1. The list does not include measurements of CME-sheaths without a ME.

We use an extended collection of SIR lists to cover the time range of January 1995 - December 2020. In contrast to the CME list, the definitions of start and end times of SIRs vary between different sources. We therefore made efforts to unify and standardize those lists to make our results more robust. We combine the Jian SIR list (Jian et al., 2011, time range: 1995–2009), the Grandin SIR and HSS catalog (Grandin et al., 2019, time range: 1995–2017), and the updated list by Geyer (Geyer et al., 2021, time range: 2014–2018).

The SIR and HSS list of Grandin is used as a basis for the whole list, because it provided the largest time coverage, with SIRs and HSSs from 1995 to 2017. The list provides the start time of the event, the time of maximum SW speed (within 3 days after the beginning of the event), and the end time of the event. The end time is defined by the time, where the speed drops below 450 km s^{-1} (Grandin et al., 2019). The event times of Grandin were used when an event was given in several lists.

The list by Jian provides times for each SIR, giving a start, stream interface, and end time, and the stream interface time is defined at the peak of the total perpendicular pressure (Jian et al., 2006a). For Jian's list, Wind (Harten & Clark, 1995; Wilson et al., 2021) and ACE (when Wind data is unavailable) data are used. The time of maximum SW velocity and information on the trailing HSS of each SIR is not given. We therefore manually checked each event and added the times using 1-min resolution OMNI data (King & Papitashvili, 2005). For the time range investigated OMNI data comes from Wind and ACE at the L1 point and is propagated to the nose of the bow shock. We defined the end time of each HSS as the time when the velocity dropped below 400 km s^{-1}. This value is a compromise between Grandin's list and other lists used in this paper. When several HSSs overlap and the velocity did not drop below 400 km s^{-1} in between, the time of the minimum value before the start of the next stream was used.

The list of Geyer focused on HSSs, with the start time defined as the density peak, and the end time as the time when the velocity drops below 350 km s^{-1}. We manually checked that list and provided the times for the maximum velocity, the time for the velocity to drop below 400 km s^{-1}, and an estimated time for the start of the associated SIR. The new start times were necessary, because the time at the density peak is usually slightly before the stream interface of the SIR. We use the start time of the SIR itself, which coincides with the increase of density and velocity.

Additionally, we manually searched for SIRs in OMNI data from 2019 to 2021, using the following definitions: the start of the SIR defined as the start of the increase of density and velocity, the maximum velocity time, and the end time where the velocity drops below 400 km s^{-1}. We checked the proton temperature to gain confidence in our SIR detection, because the temperature sharply increases after the stream interface (Jian et al., 2006a). In our final SIR list, we excluded events where the velocity never reached 400 km s^{-1} and events that coincided with several or strong CMEs. These efforts ensure that we can make robust analysis of the jets happening during each type of large-scale SW events.

For the further analysis we use the coherent lists of start and end times of the following large-scale structures: (a) SIR + HSS, (b) CME-sheath, (c) CM-ME.

Table 1 shows the minimum, median, mean and maximum durations of SW events in hours. It showcases the times for SIRs + HSSs, CME-sheaths, CME-sheath + CME-ME (when a CME showed both regions), and CME-ME (all ME, regardless of the presence of a CME-sheath). Only events that are overlapping with THEMIS magnetosheath data (see Section 2.2) are used for this statistic.

2.2. Jet Lists

The detection of magnetosheath jets is strongly dependent on the imposed definition and thresholds. Several studies have detected jets by using dynamic pressure thresholds based on the SW (LaMoury et al., 2021; Plaschke et al., 2013; Vuorinen et al., 2019). As we analyze the occurrence of jets during SW disturbances, SW parameters (and subsequently the jet detection thresholds) can rapidly change during these times. This could cause a bias in our jet occurrence during SW events. Therefore, we compiled two lists of jets. The first jet list uses SW based thresholds, which we call the upstream jet list. The second jet list, named the local jet list, is based on local magnetosheath data to reduce the previously mentioned biases. We provide both new jet lists (upstream and local criteria) and the magnetosheath times at https://osf.io/6ywjz/ (Koller et al., 2021).

Both jet lists are created using THEMIS data (Angelopoulos, 2008). THEMIS consists of five spacecraft named A, B, C, D, and E. The orbits of the individual THEMIS spacecraft can differ and change over time, which can cause a significant difference of detected jets by different spacecraft. Therefore, we look at the data of each spacecraft individually. Because both B and C spacecraft were placed in an orbit around the Moon in 2010 as part of the Acceleration, Reconnection, Turbulence and Electrodynamics of the Moon's Interaction with the Sun (ARTEMIS) mission, we have only a small number of magnetosheath events from THEMIS B and C (Angelopoulos, 2011). We used data from the THEMIS Electrostatic Analyzer (ESA; McFadden et al., 2008) and Fluxgate Magnetometer (FGM; Auster et al., 2008). Specifically, we used the ESA ion velocity, ESA ion density, ESA temperature moments, ESA ion energy flux, and the FGM magnetic field measurements.

In order to obtain the time intervals when each THEMIS spacecraft were within the magnetosheath we used the criteria of Plaschke et al. (2013). Here we briefly describe these criteria: The spacecraft is required to be within a 30° Sun-centered cone with tip at Earth. This ensures that the spacecraft is confined to the sub-solar region around local noon, and therefore avoids jet criteria issues that can occur in the flanks of the magnetosheath. The distance is required to be within 7–18 R_e from the Earth's center. The measured ion density needs to be twice as dense as the solar wind. The energy flux of 1 keV ions is required to be larger than that of the 10 keV ions. This excludes times of measurements within the magnetosphere. The intervals are required to be longer than 2 min. We used the original magnetosheath interval times provided by Plaschke et al. (2013). In addition to that, we expanded the list up to 31 December 2020 by using the same criteria. Then we searched for jets in these magnetosheath intervals.

The first jet list, named the upstream jet list, uses the criteria given by Plaschke et al. (2013). The main threshold is given by $p_{\mathrm{dyn,x}} > \frac{1}{2} p_{\mathrm{dyn,x,sw}}$, using upstream SW data from 1-min resolution OMNI data at the same time as a base for setting the threshold. $p_{\mathrm{dyn,\,x}}$ denotes the dynamic pressure in GSE-X direction, and $p_{\mathrm{dyn,x,sw}}$ the dynamic pressure of the SW in GSE-X direction. The time range for the jet was then defined as the range when the dynamic pressure exceeds 1/4 of the SW dynamic pressure. We used the original list of jets from 2008 to 2012 for THEMIS A-E by Plaschke et al. (2013) and the expanded list of jets using THEMIS A, D, and E from 2012 to 2018 (LaMoury et al., 2021; Plaschke et al., 2013). Both original lists are available online (Plaschke, Hietala, & Angelopoulos, 2020; Plaschke, Hietala, & LaMoury, 2020). We reforged the jet list to include the time range of 1 January 2018–2031 December 2020. It is important to note that THEMIS data are sometimes reprocessed. Therefore there might be differences in the jets and magnetosheath times between the current list and the original datasets.

Our second jet list, which we name the local jet list, uses the following criteria: $p_{\mathrm{dyn,x}} > 3 \times \langle p_{\mathrm{dyn,x}} \rangle_{\mathrm{20min}}$. Here, $\langle p_{\mathrm{dyn,x}} \rangle_{\mathrm{20min}}$ denotes the 20 min running average of the magnetosheath dynamic pressure in GSE-X direction. All magnetosheath times shorter than 20 min (e.g., close to the boundary) are not considered. This definition is a modification of the jet definition used by Archer and Horbury (2013), but we use the component of the dynamic pressure in the GSE-X direction similar to the upstream jet list definition. Archer and Horbury (2013) used a factor of 2 as a threshold for the dynamic pressure. Because we only use the GSE-X velocity component (which is the most significant component in the magnetosheath), we settled on using the next higher integer as a threshold. The time range for the jet was then defined as the range when the dynamic pressure increases above $2 \times \langle p_{\mathrm{dyn,x}} \rangle_{\mathrm{20min}}$. This resulted in a jet list from start of January 2008 to December 2020 for THEMIS A, D, and E and January 2008 to December 2009 for THEMIS B and C.

The original upstream jet list used the dynamic pressure in x direction only to mainly find jets that can reach the magnetopause. We followed up on this goal in our definition for the local jet list. As a positive side effect,

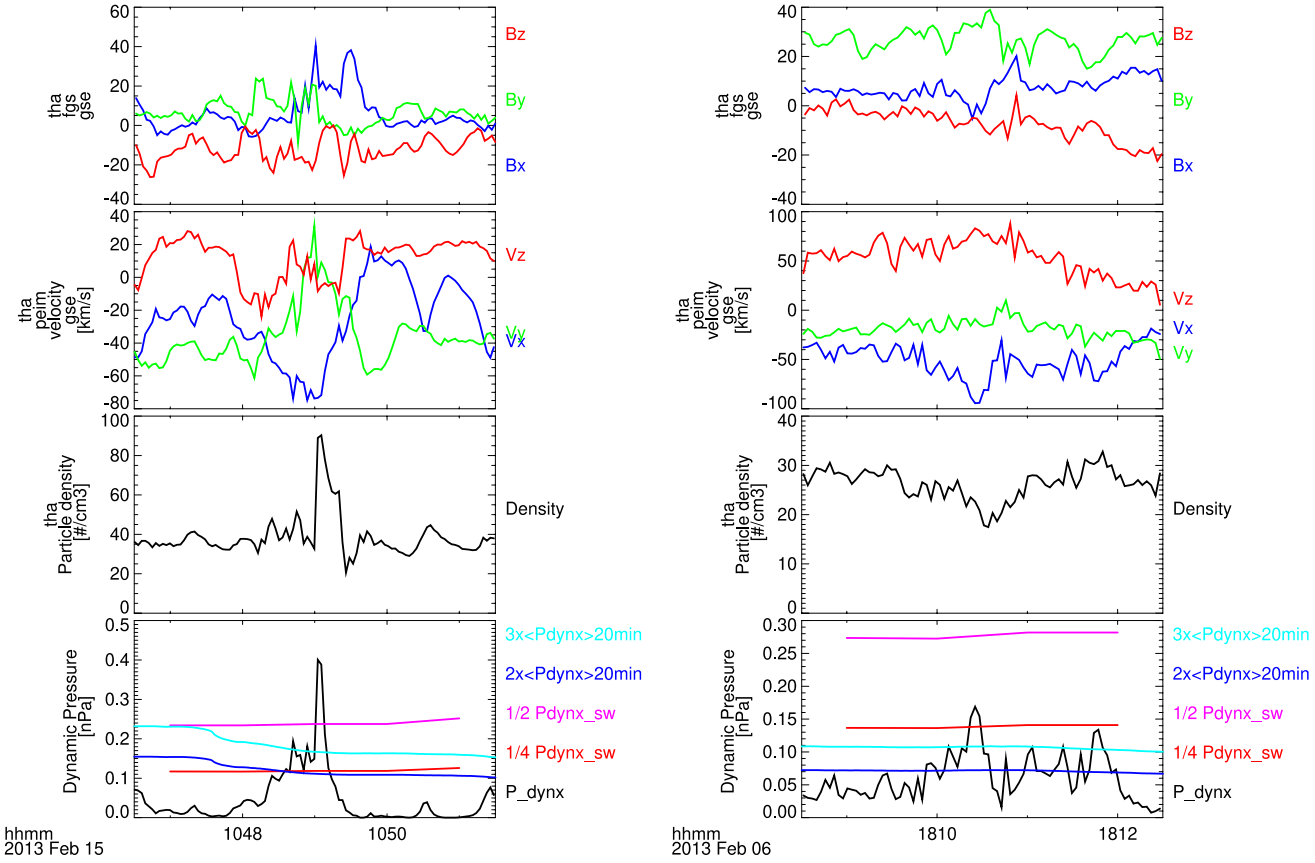

Figure 1. Two examples of jet detection by THEMIS A with threshold comparison. From top to bottom: magnetic field components, ion velocity components, particle density, and dynamic pressure. The dynamic pressure thresholds for both jet definitions are displayed in each bottom panel. The local definition thresholds (turquoise and blue) are defined as 3 and 2 times the 20-min-averaged magnetosheath dynamic pressure in GSE-X direction. The upstream definition thresholds (pink and red) are defined as 1/2 and 1/4 times the SW dynamic pressure in GSE-X direction. In the case shown on the left side, the lower dynamic pressure thresholds of both conditions (red and blue), which mark the beginning and end of the jet, are almost identical, while the upper threshold, marking the dynamic pressure that must be exceeded for the detection, is higher for the upstream condition (pink). In the case shown on the right side, the upstream jet conditions did not detect any jets, because the detection threshold (pink) is too high, while the local jet criteria (cyan) detected two jets.

Table 2
Statistical Overview of the Two Main Jet Lists Used Within This Work

	Upstream jet list	Local jet list
Total jets	16,494	18,808
THEMIS A	4147	5405
THEMIS B	147	118
THEMIS C	586	506
THEMIS D	3801	5001
THEMIS E	7813	7778
Total jet time (days)	8.7	6.2
Mean jet time (sec)	45.6	28.5
Median jet time (sec)	29.0	19.0
Number of overlapping jets	8935	9351

both lists became comparable. This validates that we are indeed looking at the same jet effects. To ensure this, the local jet list includes the same side criteria as the upstream jet list (Plaschke et al., 2013): the ion GSE-X velocity of the jet has to be negative, and the magnetosheath GSE-X velocity within 1 min before and after the jet interval has to go above half of the measured GSE-X velocity during the jet's dynamic pressure peak. Calibration features and orbit differences might impact the total number of jets detected for individual spacecraft. We manually checked to make sure that the detected jets are indeed distinct pressure enhancements over the background value for each spacecraft. Figure 1 shows the differences between both detection criteria for two examples. Following this procedure we obtain a different number of jets that is summarized and compared in Table 2. For each jet list we give the number of jets detected by each spacecraft, the total jet time in days as well as the mean and median jet time in seconds. The last row shows, how many jets of the list are (at least partially) overlapping with jets from the other list. The difference in the number of overlapping jets stems from the fact that several jets in a list may overlap with only one jet from the other list.

Orbits of the different spacecraft may be similar, which could result in single jets detected at more than one spacecraft. We give spacecraft separation estimates for THEMIS A, D, and E to address the issue of double-counting of jet events. We derive that for 39.77% of the available observation time, only one of the three spacecraft was within the previously defined magnetosheath range. We determine the spacecraft separation for the residual time, which means for all instances when at least two spacecraft were within the defined magnetosheath range at the same time. As jets dominantly move along the GSE-X direction, we determine the separation in the GSE y- plane. The average Y-Z separation for all instances over the whole time range was 1.33 R_e with a standard deviation of 1.25 R_e. We find that the orbits of the THEMIS spacecraft changed significantly during the analyzed time range. The orbits deviated from each other in the time range of 2016–2019. We determine an average Y-Z separation of 2.54 R_e with a standard deviation of 1.59 R_e for this time range. Overall, all three spacecraft together showed the closest separation in 2010 with an average distance of 0.40 R_e and a standard deviation of 0.15 R_e. Considering this, the average separation of THEMIS spacecraft exceeded the expected median perpendicular scale size of jets of 0.12 R_e (see Plaschke et al., 2020) during the analyzed time range. We conclude that most of small and medium sized jets got detected by a single spacecraft. Large jets might get detected by two or more spacecraft during times of little separation.

2.3. Analysis Methods

In order to study how the jet occurrence behaves during large-scale SW events, we follow a three-step procedure as described in the following.

Step 1: Quantifying the amount of available data. We checked the total time of magnetosheath observations as well as the number of jets that overlap with times of large-scale SW structures (SIR + HSS, CME-sheath, CME-ME). Little overlap of magnetosheath data with SW disturbances lead to high uncertainties in the subsequent analysis. To determine whether the duration or number of jets is changed during disturbances, we quantify the jet mean and median time length for each type of event. We visualize the distribution of jet durations for each type of disturbances as well as quiet SW times (all times where neither SIR nor CME interacts with Earth) by using boxplot statistics.

Step 2: First order estimate of jet occurrence rate during CME and SIR times. We define a "jet percentage" during a specific time range, given by the total duration of jet time divided by the total duration of magnetosheath measurement within that given time range. This is calculated for all SIRs + HSSs, for all CME-sheaths, and for all CME-MEs. We also calculate the jet percentage during quiet SW time, and over the entire available time range (including both quiet SW times and times of SW structures), which we call the "overall jet percentage". The values are given individually for each spacecraft, to cross-check for instrumental and orbital effects. We also calculate the mean number of measured jets per hour to check, how the value for each type of event is changing compared to the jet percentage. The jet percentage is codependent on the size and speed of jets, while jet occurrence does not take that into account. We mainly focused on the jet percentage to make conclusions based on the total jet observation time. In addition to that, the jet percentage is not drastically influenced by short jets that barely meet our defined threshold. This makes the results more robust against uncertainties in the jet criteria definition.

Step 3: In detailed analysis of jet occurrence during CME and SIR times. We used a superposed epoch analysis (SEA) to determine at which time in the CME or SIR profile the jet occurrence rate changes. For SIRs + HSSs, we set the zero epoch, that is, 0 hours, at the start of the SIR (defined as the onset of the velocity and density increase) and the end time to the mean SIRs + HSSs duration in hours (see Table 1). For CME-sheath and CME-ME, we use a 3-point SEA to analyze both parts of the CME separately. The length of each individual event varies largely, therefore we have normalized each CME-sheath and CME-ME to their respective mean duration (see Table 1). We set the zero epoch for the CME-sheath to be the CME-shock arrival time and its end to the mean time length for CME-sheath (11.7 hr, see Table 1). The arrival of the CME-ME marks the zero epoch time for the CME-ME part. It ends after the mean time length of all associated CME-MEs. Both SEA are then joined together where the CME-sheath time ends and the CME-ME begins to form the 3-point SEA. The mid-point time of magnetosheath intervals and jet intervals are converted to the new SEA timeline. The individual jet duration as well as most sheath measurements are short compared to CME and SIR timescales. Therefore, we bin the time axis in 1 hr duration bins and sum up the duration of each jet and sheath in the associated bin. Each interval is

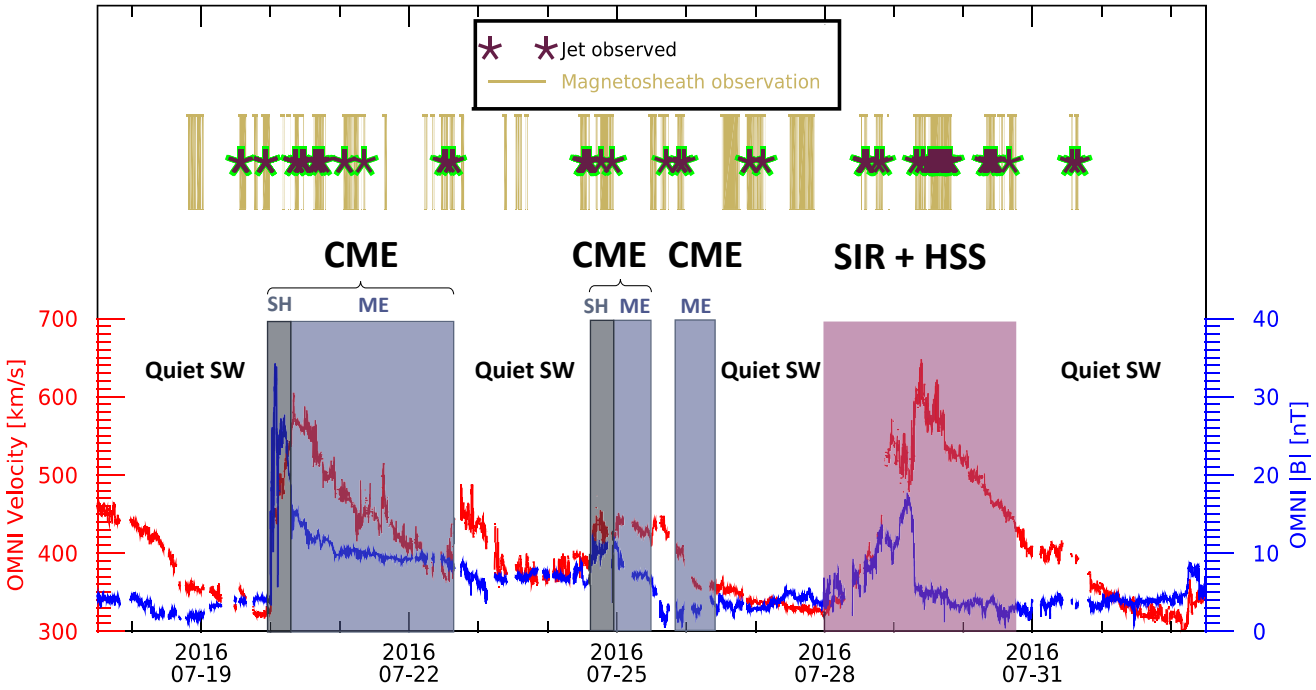

Figure 2. Timeline plot of July 2016 showing an example of observed jets by THEMIS A, D, and E (indicated as star symbols) during CME sheath (SH), CME magnetic ejecta (ME), SIR and quiet SW times. Time ranges of available magnetosheath observations by any spacecraft are plotted in gold. The bottom panel shows OMNI total velocity and total magnetic field during the time range.

summed up in the bin in which the interval mid-point falls in the new SEA timeline. The original sheath and jet interval durations are used for the sum in each bin. Otherwise, intervals measured in short SW structures would be stretched and over-represented. Intervals during shorter structures would have been compressed and thus under-represented for each bin, the jet percentages are calculated. The jets are sporadic events, therefore, a running average of the final percentage per time is necessary. We apply a running average using a sliding window with a length of 50 hr for the SIRs + HSSs and 10 hr for the CME-sheath + ME plots. We applied the SEA for SIR + HSS and for CME-sheath + ME. CME-MEs without a sheath are not analyzed using SEA because of the small number of available events. Only CMEs that show both a sheath and a ME were considered to find conclusions for both individual parts of the structure.

The final result yields a jet percentage time evolution for the mean CME-sheath + ME and SIR + HSS structures. We used a bootstrapping approach to check the robustness of the result and to give very conservative error estimates. We redo the analysis and randomly select (and replace) a sample covering only 50% of all sheath observations for each spacecraft. We repeated this 100 times for each event type, resulting in 100 different profiles of jet percentage evolution and their related mean jet percentages. The standard deviation of the derived jet percentages are given as uncertainties. This method puts the results from the second step into perspective and enables us to make general conclusions on the temporal evolution of jets during SW structures. We compare the jet percentage evolution with the quiet jet percentage that we defined in method. We used the bootstrapping method to get an error estimate for the mean quiet value as well.

We address the results of each spacecraft individually. By not mixing the jet results, we can make clear statements and conclusions about the relative change in detected jets for different solar wind time periods for each spacecraft, independent of possible calibration or orbital differences. With that we also avoid the possible issue of double-counting jets that might have been detected by several spacecraft due to times of similar orbits.

Figure 2 shows the visualization of a time range to give an example of the available data. We have magnetosheath observations by THEMIS overlapping with both CME and SIR structures hitting the Earth in the given time range. Observed jets, which are very short in time compared to the displayed time range, are displayed as stars in this figure. The CME structures are divided into the CME-sheath and the CME-ME. To show the SW conditions,

Table 3
Total Time (in Days) of Magnetosheath Observation by Each Spacecraft During Each Type of Events

	Observation time in Magnetosheath (# of individual events)			
	Total time (days)	SIR + HSS (days)	CME-Sheath (days)	CME-ME (days)
THEMIS A	156.3	52.6 (85)	3.4 (28)	9.0 (49)
THEMIS B	3.4	1.0 (12)	0.1 (1)	0.1 (1)
THEMIS C	11.1	3.8 (18)	0.0 (1)	0.0 (0)
THEMIS D	127.8	42.4 (83)	3.8 (29)	8.4 (45)
THEMIS E	157.9	54.7 (87)	3.3 (25)	9.9 (47)
Total	456.6	154.5 (105)	10.6 (39)	27.4 (55)
Percentage of total time	100%	33.8%	2.3%	6.0%

Note. The number of individual SW events that overlap with magnetosheath measurements are given in parentheses.

the OMNI data for the total velocity and the total magnetic field is plotted. The CMEs show a distinct strong magnetic field, while the SIR and HSS show the typical profile of high SW velocity over several days.

3. Results

3.1. Step 1 Results

Table 3 shows the total time (given in days) of available magnetosheath data during each type of SW events. The number of individual events is also given. The results are highly influenced by the orbits of each spacecraft. THEMIS B and C show only little magnetosheath dwell time overall compared to the other spacecraft. There is almost no magnetosheath observation during CMEs for both spacecraft. Therefore the focus in the further statistics are put on the spacecraft A, D, and E.

Table 4 and Table 5 show the number of detected jets during each type of events for the upstream jet and the local jet list, respectively. THEMIS B and C show fewer detected jets compared to the other spacecraft, which is a result of the little magnetosheath dwell time. With several thousand jets, we observed the most jets during SIR and HSS structures. Comparing with the total number of detected jets, we see that roughly 40% of all jets are observed during SIRs and HSS times. This is valid for all spacecraft surveyed. The number drops by an order of magnitude when looking at the CME-sheath revealing roughly 100 observed jets for each spacecraft. In comparison, the number of jets increases slightly for the CME-ME times, with a maximum of 316 jets for THEMIS E. We see that in both jet lists, THEMIS E shows the most jets of all five spacecraft.

Next, we calculate the mean and median duration of jets during SIRs + HSSs and CMEs. This helps to determine, whether the production or duration of the jets is more affected by each type of event. Figure 3 shows the distribution of the jet time length for each event using box plots for the upstream jet and local jet definition. The box shows the interquartile range, which is the range between the first and the third quartile. Therefore, 50% of the jet lengths are within the box. The middle line in the box shows the median length of jets in each case. The whiskers show the upper and lower limit of the distribution. Outliers are defined as all values beyond three times the length of the interquartile range. They are displayed as black stars in the plots. The median values and interquartile ranges for jets during SIRs + HSSs, CME-sheaths and CME-MEs are fairly comparable for each spacecraft and jet definition. The jet lengths between spacecraft are more comparable using the local jet criteria. The duration of jets during CME-sheaths tend to be shorter compared to the other structures in the local jet criteria. On the other hand, the duration of jets during quiet SW times seem to slightly exceed

Table 4
Number of Detected Jets During Large-Scale SW Events for the Upstream Jet List

Upstream jet definition	Total	Jets during SIRs + HSS	Jets during CME - sheath	Jets during CME - ME
THEMIS A	4,147	1,783	70	86
THEMIS B	147	53	2	1
THEMIS C	586	216	0	0
THEMIS D	3,801	1,563	106	107
THEMIS E	7,813	3,705	114	199

Table 5
Number of Detected Jets During Large-Scale SW Events for the Local Jet List

Local jet definition	Total	Jets during SIRs	Jets during CME - sheath	Jets during CME - ME
THEMIS A	5,405	2,184	96	236
THEMIS B	118	59	1	0
THEMIS C	506	200	0	0
THEMIS D	5,001	2,241	109	188
THEMIS E	7,778	3,562	118	316

the jets during structured SW. In general, the interquartile ranges overlap in every category. We see that the range of outliers is drastically greater for the upstream jet definition and go far beyond the displayed range here. For each boxplot, the number of outliers range between 2% and 4% of the total number of detected jets. The number of outliers appear to be proportional to the number of detections and not dependent on the type of event. Overall, we see that the duration of jets are not drastically influenced by different SW structures. Therefore, the results calculated in step 2 and step 3 are primarily influenced by the number of jets produced during SW structures.

3.2. Step 2 Results

The resulting jet percentage and the mean number of jets per hour during specific time ranges (all times, quiet SW, SIR + HSS, CME-sheath, CME-ME) is shown in Table 6 for the upstream jet definition and in Table 7 for the local jet definition. As previously mentioned, we differentiate between results for THEMIS A, D, and E. The difference in jet percentage between the spacecraft is smaller for the local jet definition. Overall, the range of values for the local jet list is significantly smaller compared to the upstream jet list. The percentages of jets during quiet SW conditions are fairly comparable with the overall mean values. The jet percentage for THEMIS E exceeds both

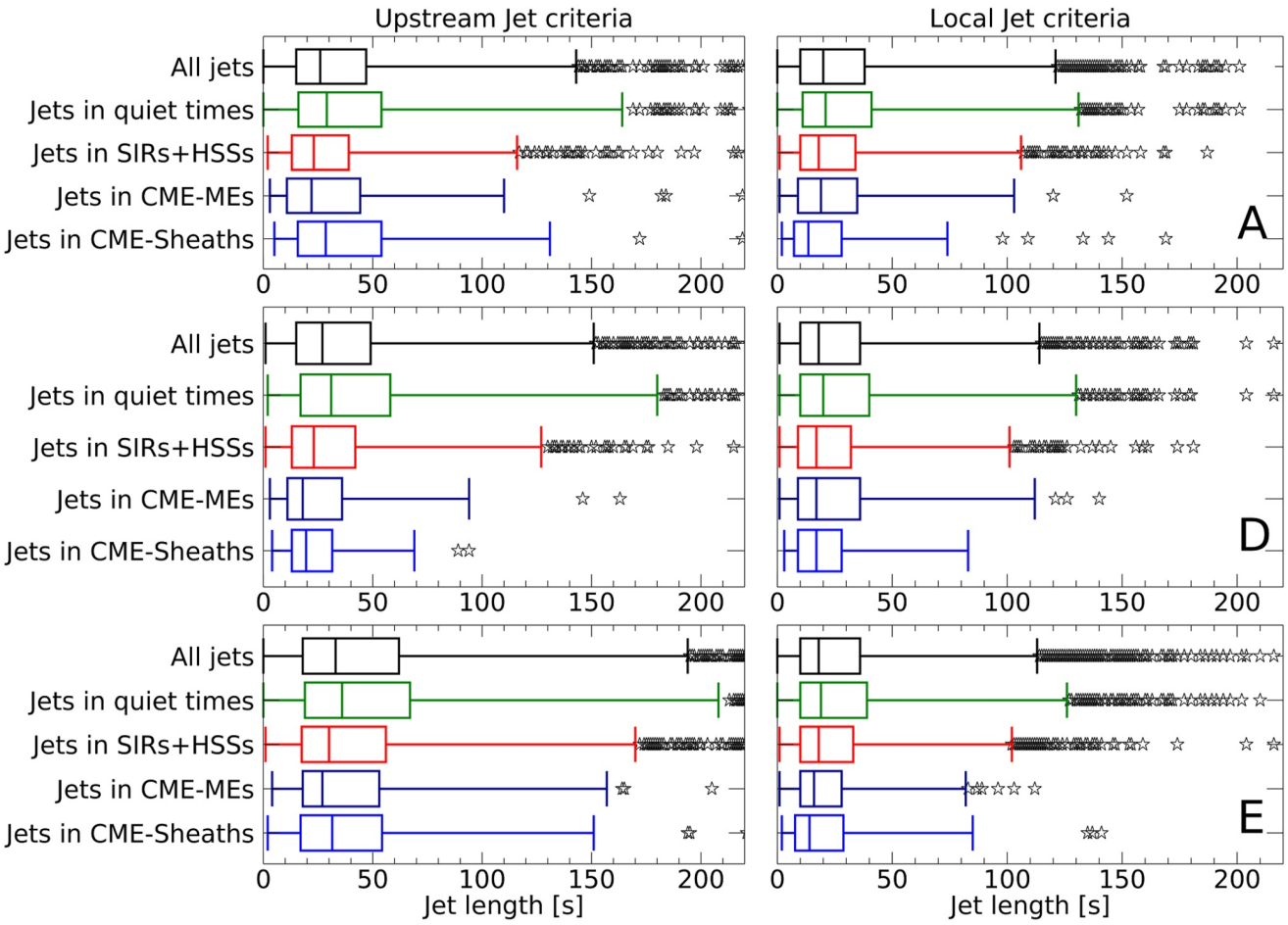

Figure 3. Statistical boxplot for the upstream and local jet lists, giving the jet duration for all jets and for jets that occurred during SW quiet times, SIRs + HSSs, CME-sheaths, and CME-MEs. The rows, from top to bottom, correspond to data from THEMIS A, D, and E. Each box shows the interquartile range. The middle line in the box shows the median length of jets in each case. The outliers, which are represented by black stars, are defined as all values beyond three times the length of the interquartile range.

Table 6
Mean Jet Percentages and Jets Per Hour During Each Event Type for the Upstream Jet List

	Jet percentages—upstream jet criteria				
	Overall	Quiet SW	SIR + HSS	CME-sheath	CME-ME
THEMIS A	1.19%	1.22%	1.26%	1.24%	0.56%
THEMIS D	1.39%	1.54%	1.37%	0.82%	0.44%
THEMIS E	2.96%	2.75%	3.69%	1.81%	1.35%
	Jets per hour—upstream jet criteria				
THEMIS A	1.1	1.0	1.4	0.8	0.4
THEMIS D	1.2	1.2	1.5	1.2	0.5
THEMIS E	2.1	1.8	2.8	1.4	0.8

other spacecraft in every category for both jet definitions. We suspect that a calibration feature may cause this difference in the data.

We find that, in general, the percentage as well as the number of jets per hour is increased while a SIR + HSS is passing the Earth. Exceptions are found in the upstream list for THEMIS A and D, where the SIR + HSS percentage is close to the overall value. However, the number of jets per hour is still increased in both cases. The increase of jets per hour for SIR + HSS times is roughly between 20% and 50%. For CME-sheath times, we see a general trend of a jet percentage and jets per hour drop. Only THEMIS A in the upstream jet list shows no drop in the CME-sheath compared to the mean value. However, the number of jets per hour still decreases. The drop in jets per hour is roughly between 0% and 30%. For the CME-ME times, we see a clear drop of jet percentage and jets per hour for every spacecraft for both jet definitions. The drop in jets per hour is roughly between 20% and 60%.

The following trend is visible for all spacecraft in both definitions: jet percentage during SIR + HSS ≥ jet percentage during CME-sheath ≥ jet percentage during CME-ME. The same findings hold for the calculated jets per hour.

3.3. Step 3 Results

The evolution of the jet percentage over the mean SIR + HSS and CME-sheath + ME times is shown in Figure 4 and Figure 5 for the upstream and local jet list, respectively. The mean SW parameters during SIR + HSS and CME-sheath + ME are plotted in the first row. The second row of each figure corresponds to THEMIS A data, the second row to THEMIS D, and the third row to THEMIS E. The mean jet percentage value of the quiet SW is plotted for comparison in black. The results for SIRs + HSSs are shown in the left column. The jet percentage at the start of the SIR roughly coincides with the mean quiet value. The jet percentage shows an increase after the SIR start. This finding is valid for each spacecraft surveyed for both jet definitions. The peak of the jet percentage is visible at roughly 75–90 hr after the zero epoch for most spacecraft. Only THEMIS A in the upstream jet criteria shows the peak after the end of the HSS. The decrease in percentage seems to continue after the defined ending of the HSS. The associated uncertainties are lower compared to the CME results, because the number of available SIRs that overlap with magnetosheath data is larger.

The results for CME-sheaths + MEs are shown in the right column of Figures 4 and 5. Each jet percentage datapoint in both figures is equivalent to a 1-hr bin. On average, each bin has roughly 12 hr of magnetosheath data during SIRs and 8.5 hr of data during CME-sheath and CME-ME. The jet percentage during the CME-sheath time is monotonically decreasing for each spacecraft surveyed for both jet definitions. The jet percentage during the CME-ME is lower than the mean value for each spacecraft surveyed for both jet definitions. The jet percentages recover sharply after the end of the CME-ME. The estimated uncertainties are higher compared to the SIR SEA. This is the result of the low number of CME-sheaths + MEs that overlap with Earth's magnetosheath measurements, as was previously mentioned. In addition to that, the restriction to analyze each spacecraft individually enlarges the uncertainty for each single analysis. Still, every spacecraft shows the same general trend within the SW structures in each analysis. This improves the confidence in our results.

Table 7
Mean Jet Percentages and Jets Per Hour During Each Event Type for the Local Jet List

	Jet percentages—local jet criteria				
	Overall	Quiet SW	SIR + HSS	CME-sheath	CME-ME
THEMIS A	1.18%	1.17%	1.28%	0.79%	0.80%
THEMIS D	1.27%	1.23%	1.51%	0.72%	0.72%
THEMIS E	1.60%	1.51%	1.93%	0.98%	0.85%
	Jets per hour—local jet criteria				
THEMIS A	1.4	1.3	1.7	1.2	1.1
THEMIS D	1.6	1.4	2.2	1.2	0.9
THEMIS E	2.1	1.8	2.7	1.5	1.3

When we compare the jet percentages of SIR + HSS, CME-sheath and CME-ME profiles with each other, we see the same picture over all spacecraft and jet definition: Jet percentages start to rise strongly during the SIR passage reaching a peak after the HSS reached its maximum speed. The jet percentage is decreasing sharply during the passage of the CME-sheath with

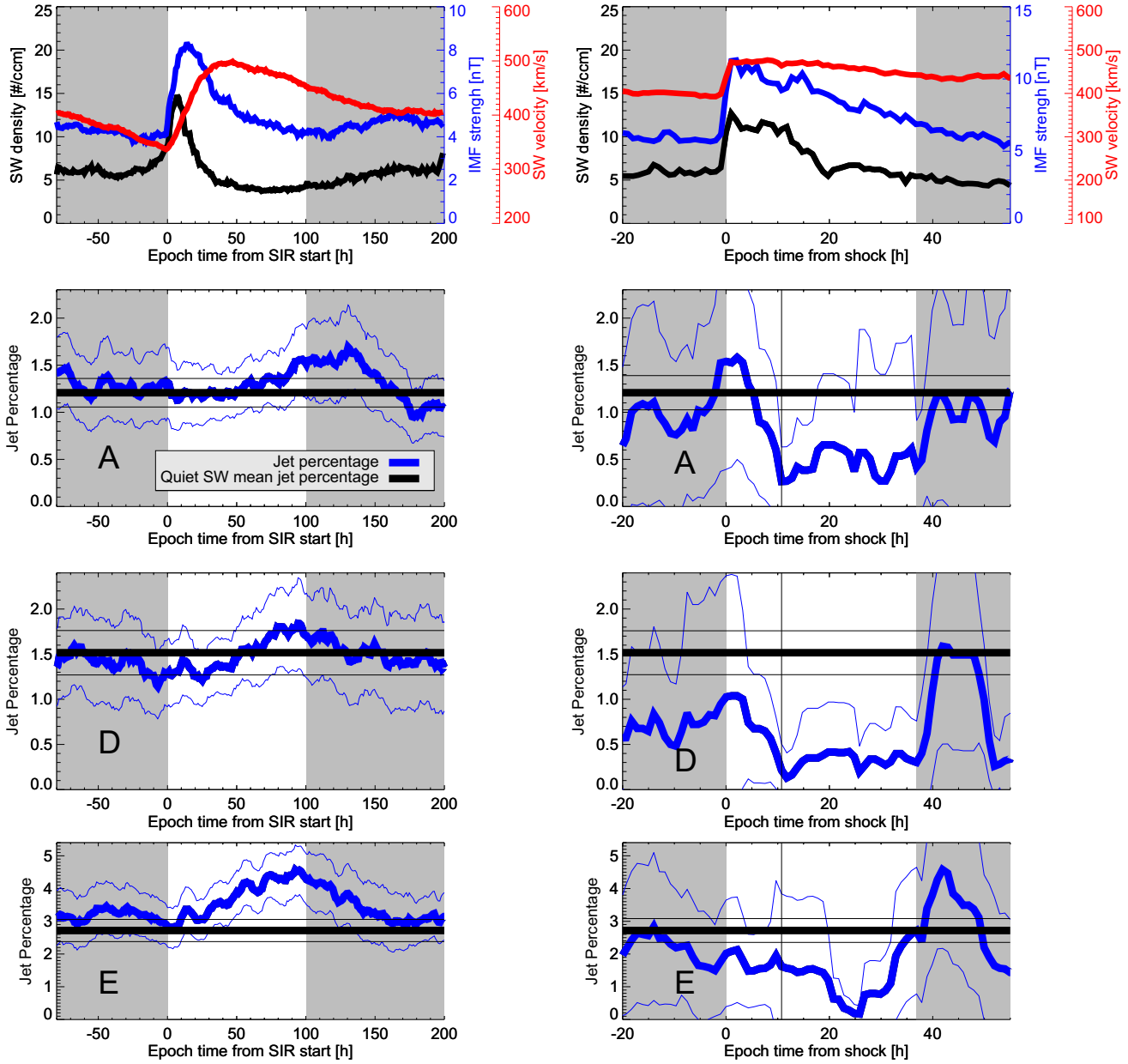

Figure 4. Mean SW parameters (first row) and jet percentages for THEMIS A, D, and E (row 2–4) using the upstream jet definition. The left column shows the values for the SIR + HSS times, the right column shows the values for the CME-sheath and CME-ME times. The mean SW velocity (black), IMF strength (blue), and SW density (red) is plotted. The jet percentages are plotted using a bold blue line. The faint blue lines are the error estimations. The bold black line shows the quiet mean value (Table 6) and the faint black lines show the error estimations.

low values close to the transition from sheath to CME-ME structure. During the entire CME-ME time, the percentages stay at a low level and recover as the CME-ME structure ends.

4. Discussion

4.1. Diminished Jet Numbers During CME Passing

Previous studies found a clear correlation of jet production downstream of Earth's bow shock with a steady IMF that is quasi-parallel to the bow shock normal (Archer & Horbury, 2013; Plaschke et al., 2013; Vuorinen

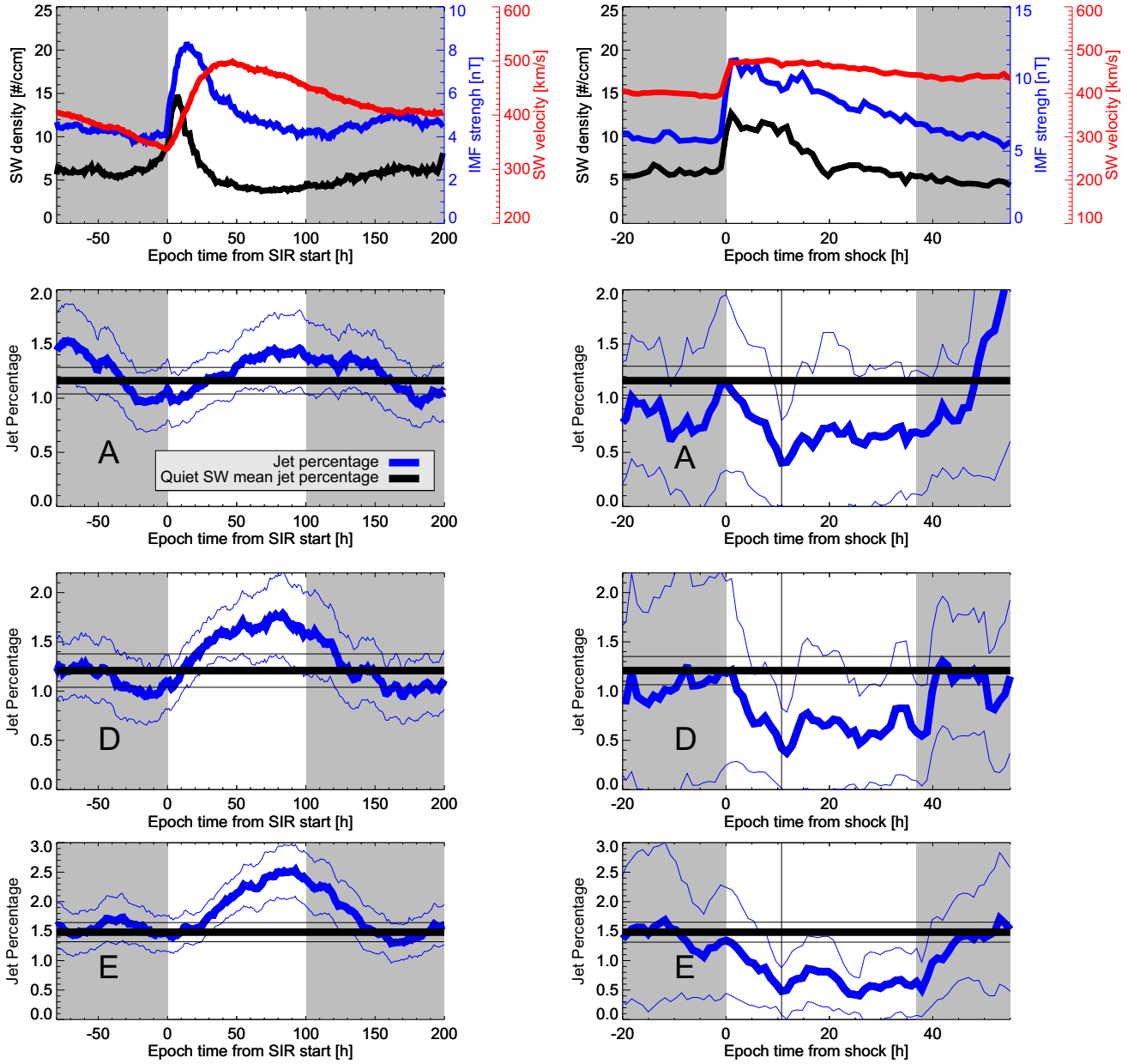

Figure 5. Same as Figure 4 but for the local jet definition.

et al., 2019). The IMF usually becomes highly variable during CME-sheaths (e.g., Jian et al., 2006b), which could disrupt a stable foreshock. This in turn results in fewer jets that get produced. On the other hand, the highly dynamic plasma in the CME-sheath may cause a new rippling in the bow shock. In our study we derive, regardless of spacecraft, that the jet percentage is clearly dropping during the passing of the CME-sheath (see Figures 4 and 5). Further analysis on a case-to-case basis of these regions will enable us to better understand the physical processes behind.

The IMF angle drastically changes within the CME-ME, and hence, the position of the quasi-parallel shock front (and the foreshock). However, the timescale of the changing IMF angle is much longer (several hours) compared to the timescale of jet generation (several minutes). The IMF in the CME-ME is steady for timescales of roughly 10 min, which is expected to be a favorable condition for jet production. This might indicate that the presence of a strong IMF itself is a key factor that inhibits jet generation. We find in our study that the number of jets is

very much lowered during the CME-ME but still covers a significant number of jets. We may speculate that these jets are different compared to the jets observed during quiet SW times as the bow shock region where jets get produced might change during the CME passage. Raptis et al. (2020) performed statistical analysis of jets and differences in their parameters downstream of the quasi-parallel and quasi-perpendicular shocks. They concluded that jets downstream of the quasi-parallel shock front occur more frequently and possess higher dynamic pressure and duration compared to jets found downstream of the quasi-perpendicular shock. They also noted the existence of "encapsulated jets", which show properties similar to quasi-parallel jets but are found behind the quasi-perpendicular shock front. Raptis et al. (2020) suggested that these jets may originate from the flanks of the bow shock during large IMF cone angles. Further investigation might reveal whether we see the same effect in the properties of jets that are observed during the CME-ME.

From our detailed analysis using SEA, we find that the number of jets seem to recover as the CME-ME ends. The wakes of CMEs might possess radial IMF for an extended period of time (Neugebauer et al., 1997), which would benefit the production of jets. However, at this point we did not exclude multiple CME events (this would have lowered our statistics). We infer that the SW conditions in the trailing region of the CME might play an important role in the jet production rate. As sequences of CMEs would change these conditions, they should be taken into account. Hence, the shown results are inconclusive whether the sharp increase of jets after the CME is due to favorable SW conditions or due to the recovering of the mean jet production rate.

A constant extremely high dynamic pressure level within the individual parts of the CME (especially sheaths) may cause non-detection, because the jet detection threshold could be increased beyond the usual dynamic pressure value of jets. On the other hand, we find in our study an increase of jet percentage during SIRs, which is related to a moderately higher dynamical pressure too (Jian et al., 2006a). The effect of CMEs compressing the bow shock and the magnetopause (Sibeck & Gosling, 1996) has not yet been considered in the statistics. This could cause the spacecraft to temporarily change the position within the magnetosheath regarding the distance to the bow shock. Because jets are more frequently observed in the close proximity to the bow shock, this plays a role in studying jet statistics (LaMoury et al., 2021; Plaschke et al., 2013; Vuorinen et al., 2019). There are three possible outcomes of this compression regarding the relative position of the spacecraft: First, the spacecraft is positioned within the magnetosheath and the distance to the bow shock shrinks during compression. This would cause an increase in detected jets. Second, the spacecraft is close to the bow shock and crosses the shock during the compression, causing the spacecraft to be in the SW. This would first lead to an increased number of jets at the beginning, and a decrease in sheath data during the compression. Third, the spacecraft is within the magnetosphere close to the magnetopause, and the compression causes the spacecraft to cross the magnetopause, causing the spacecraft to be within the magnetosheath. This would lead to no sheath data at the beginning, and low jet numbers after during the compression. However, the mean time that THEMIS spacecraft spend in the magnetosheath during each revolution around the Earth is several hours shorter compared to the duration of most SW structures. This suggests that the positioning in the magnetosheath might be more affected by the orbit of the spacecraft even during a simultaneous compression of the magnetosphere. A case-by-case future study could help to study effects in detail.

The list by Cane and Richardson (2003); Richardson and Cane (2010) uses times for the ejecta part measured by ACE at L1 rather than the arrival time at the Earth. We find that this issue has little influence on our statistics and no change on our general conclusions. The time shift is expected to be roughly in the range of 1 hr, which is rather small compared to the mean length of the ME (between 20 and 30 hr, Table 1). The influence on the SEA results are also negligible because the running average window is significantly larger than the time shift.

4.2. Increased Jet Numbers During SIR + HSS Passing

A fast SW appears to be somewhat correlated to a higher numbers of jets according to LaMoury et al. (2021). Specifically, LaMoury et al. (2021) found that both slow and fast SW are beneficial for jet generation at the bow shock, and jets are more likely to reach the magnetopause during high SW velocities. Overall, fast SW appears to be a favorable factor for the number of jets found within the magnetosheath. Our results of enhanced jet percentages during SIR + HSS passing agree with these results. We clearly observe that the jet percentage monotonically increases after the zero epoch (defined as onset of the SIR velocity and density increase), independent of jet definition and spacecraft surveyed. The maximum of the jet percentage is reached after the maximum speed during

the HSS is reached, hence, close to the defined end of the HSS (see Figures 4 and 5). This corresponds to mean SW conditions with low density, low IMF strength, and high (although decreasing) SW velocity. The percentage reaches mean values roughly 50–75 hr after the defined end of the HSS. At this time, the SW conditions are also supposed to be back to quiet mean conditions.

Similar to the CME times, the effect of SIRs compressing the bow shock and the magnetopause has not yet been considered in the statistics. In principle, the same impacts that we previously discussed in Section 4.1 apply. Both SIRs + HSSs and CMEs have compressing effects on the bow shock and magnetopause. In particular, SIRs and CME-sheaths often show very similar SW parameters that can affect the standoff distances (rapidly changing IMF strength and direction, velocity and density increase), but they show the exact opposite effects in the jet percentage. This rules out the possibility that the results are mainly caused by differences in the compression of the bow shock and magnetopause. There is a difference in the time profiles of increased dynamic pressure for both types of events, but both timescales are significantly longer than the timescales expected for jet generation.

4.3. Different Jet Definitions

The number and time length of detected jets vary significantly depending on the definition. The jet threshold based on upstream conditions can be a source for errors when sudden events are impacting the Earth. This would suddenly change the jet threshold and therefore bias our results during SW disturbances. In addition to that, small scale SW structures measured at L1 can differ significantly from the structures that actually arrive at the magnetosheath (Borovsky, 2020). This would again change the upstream dynamic pressure threshold to a value that should not be compared to the dynamic pressure measured in the Earth's magnetosheath. Therefore, we compiled the second jet list using local magnetosheath dynamic pressure. We see that the median time lengths of jets detected by the local criteria are more uniform during different types of SW structures (Figure 3). We find that the number of extreme outliers in the jet data is considerably lower for the local jet list compared to the upstream jet list. While the upstream jet list is certainly valid for quiet and undisturbed SW times, we conclude that the local jet criteria are more reliable when analyzing times of SW disturbances. We find that the general trends in our results are the same for both jet definitions even with the previously mentioned shortcomings.

5. Summary and Conclusion

In this work we studied the connection between large-scale SW structures and magnetosheath jets. To achieve this goal, we analyze the overlapping times of magnetosheath observation from THEMIS with times of SW events. We compile two jet lists by applying upstream and local threshold definitions using THEMIS magnetosheath observations. Sudden changes in SW parameters can suddenly change the detection threshold. Therefore, two jet definitions help us mitigate errors arising from a bias in the jet detection. We use a CME list compiled by Richardson and Cane (2010) for the start and end times of CME-sheath and CME-magnetic ejecta. For SIRs and HSSs we compile, unify, and expand times from several sources (Geyer et al., 2021; Grandin et al., 2019; Jian et al., 2011). The final SIR and HSS list includes SIR start times, HSS peak times, and HSS end times from 1995 to 2020.

First we check, how many detected jets are overlapping with large-scale SW structures. Based on this analysis, we look at each spacecraft individually. In the second step, we calculate how the total time of observed magnetosheath jets time change during SW events. We look at SIR + HSS, CME-sheath, and CME-ME individually. In the last step, we use SEA analysis to determine, how the jet occurrence changes during SW events in general.

We find a relative difference in jet percentage during different types of large-scale SW events. This is primarily a result of differences in jet numbers rather than due to a difference in mean jet duration. The number of observed jets within the Earth's magnetosheath increases during the passage of SIR and HSS by up to 50%. The number of jets decreases during the passing of a CME-ME and its associated sheath by roughly 50%. Both our jet lists focus on dynamic pressure enhancements in the GSE-X direction only. Therefore, these jets are more likely to reach the magnetopause, where they can potentially be geoeffective. This suggests that the number of geoeffective jets can be increased during SIR and HSS. For CMEs, while usually being significantly geoeffective themselves, the number of associated geoeffective jets seems to be low. Further statistical analysis to check differences in SW parameters for jets during each type of event is necessary. In addition to that, case studies will help us to gain

in-depth knowledge on individual effects happening in the magnetosheath during the passage of these types of events.

Data Availability Statement

We thank C. W. Carlson and J. P. McFadden for use of ESA data. We acknowledge the use of NASA/GSFC's Space Physics Data Facility's OMNI data and web services (https://omniweb.gsfc.nasa.gov/html/omni_min_data.html). THEMIS and OMNI data were accessed using the SPEDAS software (Angelopoulos et al., 2019). Both original jet lists covering the time ranges of 2008–2012 and 2012–2018 are available online https://osf.io/gf732/ (Plaschke, Hietala, & Angelopoulos, 2020), https://osf.io/7rjs4/ (Plaschke, Hietala, & LaMoury, 2020). We provide the new jet lists (upstream and local criteria) as well as the magnetosheath times at https://osf.io/6ywjz/ (Koller et al., 2021).

Acknowledgments
F.K., M.T., L.P., O.R., and F.P. gratefully acknowledge the Austrian Science Fund (FWF): P 33285 for supporting this project. L.K.J. thanks the support of NASA Living with a Star (LWS) and Heliophysics Support Research (HSR) programs. H.H. and A.T.L. were supported by Royal Society awards URF\R1\180671 and RGF\EA\181090. We acknowledge NASA contract NAS5-02099 and V. Angelopoulos for use of data from the THEMIS Mission. Specifically we thank K.H. Glassmeier, H.U. Auster and W. Baumjohann for the use of FGM data provided under the lead of the Technical University of Braunschweig and with financial support through the German Ministry for Economy and Technology and the German Center for Aviation and Space (DLR) under contract 50 OC 0302.

References

Angelopoulos, V. (2008). The THEMIS mission. *Space Science Reviews*, *141*(1–4), 5–34. https://doi.org/10.1007/s11214-008-9336-1
Angelopoulos, V. (2011). The ARTEMIS mission. *Space Science Reviews*, *165*(1–4), 3–25. https://doi.org/10.1007/s11214-010-9687-2
Angelopoulos, V., Cruce, P., Drozdov, A., Grimes, E. W., Hatzigeorgiu, N., King, D. A., et al. (2019). The space physics environment data analysis system (SPEDAS). *Space Science Reviews*, *215*(1), 9. https://doi.org/10.1007/s11214-018-0576-4
Archer, M. O., & Horbury, T. S. (2013). Magnetosheath dynamic pressure enhancements: Occurrence and typical properties. *Annales Geophysicae*, *31*(2), 319–331. https://doi.org/10.5194/angeo-31-319-2013
Archer, M. O., Horbury, T. S., & Eastwood, J. P. (2012). Magnetosheath pressure pulses: Generation downstream of the bow shock from solar wind discontinuities. *Journal of Geophysical Research*, *117*(A5), A05228. https://doi.org/10.1029/2011JA017468
Auster, H. U., Glassmeier, K. H., Magnes, W., Aydogar, O., Baumjohann, W., Constantinescu, D., et al. (2008). The THEMIS Fluxgate Magnetometer. *Space Science Reviews*, *141*(1–4), 235–264. https://doi.org/10.1007/s11214-008-9365-9
Baumjohann, W., & Treumann, R. A. (1996). Basic space plasma Physics. *World Scientific*. https://doi.org/10.1142/p015
Borovsky, J. E. (2020). What magnetospheric and ionospheric researchers should know about the solar wind. *Journal of Atmospheric and Solar-Terrestrial Physics*, *204*, 105271. https://doi.org/10.1016/j.jastp.2020.105271
Cane, H. V., & Richardson, I. G. (2003). Interplanetary coronal mass ejections in the near-Earth solar wind during 1996-2002. *Journal of Geophysical Research*, *108*(A4), 1156. https://doi.org/10.1029/2002JA009817
Chapman, S., & Bartels, J. (1940). *Geomagnetism* (Vol. I). Geomagnetic and Related Phenomena.
Fairfield, D. H. (1971). Average and unusual locations of the Earth's magnetopause and bow shock. *Journal of Geophysical Research*, *76*(28), 6700–6716. https://doi.org/10.1029/JA076i028p06700
Geyer, P., Temmer, M., Guo, J., & Heinemann, S. G. (2021). Properties of stream interaction regions at Earth and Mars during the declining phase of SC 24. *Astronomy and Astrophysics*, *649*, A80. https://doi.org/10.1051/0004-6361/202040162
Good, S. W., Kilpua, E. K. J., LaMoury, A. T., Forsyth, R. J., Eastwood, J. P., & Möstl, C. (2019). Self-similarity of ICME flux ropes: Observations by radially aligned spacecraft in the inner heliosphere. *Journal of Geophysical Research*, *124*(7), 4960–4982. https://doi.org/10.1029/2019JA026475
Grandin, M., Aikio, A. T., & Kozlovsky, A. (2019). Properties and geoeffectiveness of solar wind high-speed streams and stream interaction regions during solar cycles 23 and 24. *Journal of Geophysical Research*, *124*(6), 3871–3892. https://doi.org/10.1029/2018JA026396
Harten, R., & Clark, K. (1995). The design features of the GGS wind and polar spacecraft. *Space Science Reviews*, *71*(1–4), 23–40. https://doi.org/10.1007/BF00751324
Hietala, H., Phan, T. D., Angelopoulos, V., Oieroset, M., Archer, M. O., Karlsson, T., & Plaschke, F. (2018). In situ observations of a magnetosheath high-speed jet triggering magnetopause reconnection. *Geophysics Research Letters*, *45*(4), 1732–1740. https://doi.org/10.1002/2017GL076525
Hietala, N., Partamies, N., Laitinen, T. V., Clausen, L. B. N., Facskó, G., Vaivads, A., et al. (2012). Supermagnetosonic subsolar magnetosheath jets and their effects: From the solar wind to the ionospheric convection. *Annales Geophysicae*, *30*(1), 33–48. https://doi.org/10.5194/angeo-30-33-2012
Jian, L., Russell, C. T., & Luhmann, J. G. (2011). Comparing solar minimum 23/24 with historical solar wind records at 1 AU. *Solar Physics*, *274*(1–2), 321–344. https://doi.org/10.1007/s11207-011-9737-2
Jian, L., Russell, C. T., Luhmann, J. G., & Skoug, R. M. (2006b). Properties of interplanetary coronal mass ejections at one AU during 1995 - 2004. *Solar Physics*, *239*(1–2), 393–436. https://doi.org/10.1007/s11207-006-0133-2
Jian, L., Russell, C. T., Luhmann, J. G., & Skoug, R. M. (2006a). Properties of stream interactions at one AU during 1995 - 2004. *Solar Physics*, *239*(1–2), 337–392. https://doi.org/10.1007/s11207-006-0132-3
Karlsson, T., Kullen, A., Liljeblad, E., Brenning, N., Nilsson, H., Gunell, H., & Hamrin, M. (2015). On the origin of magnetosheath plasmoids and their relation to magnetosheath jets. *Journal of Geophysical Research*, *120*(9), 7390–7403. https://doi.org/10.1002/2015JA021487
Kilpua, E., Koskinen, H. E. J., & Pulkkinen, T. I. (2017). Coronal mass ejections and their sheath regions in interplanetary space. *Living Reviews in Solar Physics*, *14*(1), 5. https://doi.org/10.1007/s41116-017-0009-6
King, J. H., & Papitashvili, N. E. (2005). Solar wind spatial scales in and comparisons of hourly Wind and ACE plasma and magnetic field data. *Journal of Geophysical Research*, *110*(A2), A02104. https://doi.org/10.1029/2004JA010649
Koller, F., Plaschke, F., Temmer, M., & Preisser, L. (2021). *Themis local and upstream magnetosheath jet data 2008-2020*. OSF. Retrieved from https://osf.io/6ywjz
LaMoury, A. T., Hietala, H., Plaschke, F., Vuorinen, L., & Eastwood, J. P. (2021). Solar wind control of magnetosheath jet formation and propagation to the magnetopause. *Journal of Geophysical Research: Space Physics*, *126*(9), e2021JA029592. https://doi.org/10.1029/2021ja029592
McFadden, J. P., Carlson, C. W., Larson, D., Ludlam, M., Abiad, R., Elliott, B., et al. (2008). The THEMIS ESA plasma instrument and in-flight calibration. *Space Science Reviews*, *141*(1–4), 277–302. https://doi.org/10.1007/s11214-008-9440-2
Němeček, Z., Šafránková, J., Přech, L., Sibeck, D. G., Kokubun, S., & Mukai, T. (1998). Transient flux enhancements in the magnetosheath. *Geophysics Research Letters*, *25*(8), 1273–1276. https://doi.org/10.1029/98GL50873

Neugebauer, M., Goldstein, R., & Goldstein, B. E. (1997). Features observed in the trailing regions of interplanetary clouds from coronal mass ejections. *Journal of Geophysical Research*, *102*(A9), 19743–19751. https://doi.org/10.1029/97JA01651

Norenius, L., Hamrin, M., Goncharov, O., Gunell, H., Opgenoorth, H., Pitkänen, T., et al. (2021). Ground-based magnetometer response to impacting magnetosheath jets. *Journal of Geophysical Research: Space Physics*, *126*(8), e2021JA029115. https://doi.org/10.1029/2021JA029115

Nykyri, K., Bengtson, M., Angelopoulos, V., Nishimura, Y., & Wing, S. (2019). Can enhanced flux loading by high-speed jets lead to a substorm? Multipoint detection of the Christmas day substorm onset at 08:17 UT, 2015. *Journal of Geophysical Research: Space Physics*, *124*(6), 4314–4340. https://doi.org/10.1029/2018JA026357

Plaschke, F., Hietala, H., & Angelopoulos, V. (2013). Anti-sunward high-speed jets in the subsolar magnetosheath. *Annales Geophysicae*, *31*(10), 1877–1889. https://doi.org/10.5194/angeo-31-1877-2013

Plaschke, F., Hietala, H., & Angelopoulos, V. (2020). *Anti-sunward high-speed jets in the subsolar magnetosheath: Data sets*. OSF. Retrieved from https://osf.io/gf732

Plaschke, F., Hietala, M., Archer, M., Blanco-Cano, X., Kajdič, P., Karlsson, T., et al. (2018). Jets downstream of collisionless shocks. *Space Science Reviews*, *214*(5), 81. https://doi.org/10.1007/s11214-018-0516-3

Plaschke, F., Hietala, H., & LaMoury, A. T. (2020). *Themis magnetosheath jet data set 2012-2018. OSF*. Retrieved from https://osf.io/7rjs4

Plaschke, F., Hietala, H., & Vörös, Z. (2020). Scale sizes of magnetosheath jets. *Journal of Geophysical Research: Space Physics*, *125*(9), e2020JA027962. https://doi.org/10.1029/2020JA027962

Preisser, L., Blanco-Cano, X., Kajdič, P., Burgess, D., & Trotta, D. (2020). Magnetosheath jets and plasmoids: Characteristics and formation mechanisms from Hybrid Simulations. *The Astrophysical Journal Letters*, *900*(1), L6. https://doi.org/10.3847/2041-8213/abad2b

Raptis, S., Karlsson, T., Plaschke, F., Kullen, A., & Lindqvist, P.-A. (2020). Classifying magnetosheath jets using MMS: Statistical properties. *Journal of Geophysical Research: Space Physics*, *125*(11), e2019JA027754. https://doi.org/10.1029/2019JA027754

Richardson, I. G. (2018). Solar wind stream interaction regions throughout the heliosphere. *Living Reviews in Solar Physics*, *15*(1), 1. https://doi.org/10.1007/s41116-017-0011-z

Richardson, I. G., & Cane, H. V. (2010). Near-Earth interplanetary coronal mass ejections during solar cycle 23 (1996-2009): Catalog and summary of properties. *Solar Physics*, *264*(1), 189–237. https://doi.org/10.1007/s11207-010-9568-6

Rouillard, A. P. (2011). Relating white light and in situ observations of coronal mass ejections: A review. *Journal of Atmospheric and Solar-Terrestrial Physics*, *73*(10), 1201–1213. https://doi.org/10.1016/j.jastp.2010.08.015

Samsonov, A. A., Sibeck, D. G., & Imber, J. (2007). MHD simulation for the interaction of an interplanetary shock with the Earth's magnetosphere. *Journal of Geophysical Research*, *112*(A12), A12220. https://doi.org/10.1029/2007JA012627

Savin, S., Amata, E., Budaev, V., Zelenyi, L., Kronberg, E. A., Buechner, J., et al. (2014). On nonlinear cascades and resonances in the outer magnetosphere. *Soviet Journal of Experimental and Theoretical Physics Letters*, *99*(1), 16–21. https://doi.org/10.1134/S002136401401010X

Shue, J. H., Song, P., Russell, C. T., Steinberg, J. T., Chao, J. K., Zastenker, G., et al. (1998). Magnetopause location under extreme solar wind conditions. *Journal of Geophysical Research*, *103*(A8), 17691–17700. https://doi.org/10.1029/98JA01103

Sibeck, D. G., & Gosling, J. T. (1996). Magnetosheath density fluctuations and magnetopause motion. *Journal of Geophysical Research*, *101*(A1), 31–40. https://doi.org/10.1029/95JA03141

Smith, E. J., & Wolfe, J. H. (1976). Observations of interaction regions and corotating shocks between one and five AU: Pioneers 10 and 11. *Geophysical Research Letters*, *3*(3), 137–140. https://doi.org/10.1029/GL003i003p00137

Spreiter, J. R., Summers, A. L., & Alksne, A. Y. (1966). Hydromagnetic flow around the magnetosphere. *Planetary and Space Science*, *14*(3), 223IN1251–250IN2253. https://doi.org/10.1016/0032-0633(66)90124-3

Stone, E. C., Frandsen, A. M., Mewaldt, R. A., Christian, E. R., Margolies, D., Ormes, J. F., & Snow, F. (1998). The advanced composition explorer. *Space Science Reviews*, *86*, 1–22. https://doi.org/10.1023/A:1005082526237

Tátrallyay, M., Erdös, G., Németh, Z., Verigin, M. I., & Vennerstrom, S. (2012). Multispacecraft observations of the terrestrial bow shock and magnetopause during extreme solar wind disturbances. *Annales Geophysicae*, *30*(12), 1675–1692. https://doi.org/10.5194/angeo-30-1675-2012

Temmer, M. (2021). Space weather: The solar perspective. *Living Reviews in Solar Physics*, *18*(1), 4. https://doi.org/10.1007/s41116-021-00030-3

Tsurutani, B. T., Gonzalez, W. D., Gonzalez, A. L. C., Guarnieri, F. L., Gopalswamy, N., Grande, M., et al. (2006). Corotating solar wind streams and recurrent geomagnetic activity: A review. *Journal of Geophysical Research*, *111*(A7), A07S01. https://doi.org/10.1029/2005JA011273

Vuorinen, L., Hietala, H., & Plaschke, F. (2019). Jets in the magnetosheath: IMF control of where they occur. *Annales Geophysicae*, *37*(4), 689–697. https://doi.org/10.5194/angeo-37-689-2019

Wang, B., Nishimura, Y., Hietala, L., Angelopoulos, V., Plaschke, F., Weatherwax, A., et al. (2018). Impacts of magnetosheath high-speed jets on the magnetosphere and ionosphere measured by optical imaging and satellite observations. *Journal of Geophysical Research*, *123*(6), 4879–4894. https://doi.org/10.1029/2017JA024954

Wilson, I., Lynn, B., Brosius, A. L., Gopalswamy, N., Nieves-Chinchilla, T., Szabo, A., et al. (2021). A quarter century of wind spacecraft discoveries. *Reviews of Geophysics*, *59*(2), e2020RG000714. https://doi.org/10.1029/2020RG000714

Wu, C.-C., & Lepping, R. P. (2002). Effect of solar wind velocity on magnetic cloud-associated magnetic storm intensity. *Journal of Geophysical Research*, *107*(A11), 1346. https://doi.org/10.1029/2002JA009396

Paper 2

4

Magnetosheath Jet Formation Influenced by Parameters in Solar Wind Structures

Florian Koller[1] , Ferdinand Plaschke[2], Manuela Temmer[1] , Luis Preisser[3], Owen W. Roberts [3], and Zoltan Vörös[3,4]

[1] Institute of Physics, University of Graz, Graz, Austria
[2] Institut für Geophysik und extraterrestrische Physik, TU Braunschweig, Braunschweig, Germany
[3] Space Research Institute, Austrian Academy of Sciences, Graz, Austria
[4] Institute of Earth Physics and Space Science, ELRN, Sopron, Hungary

The following article is published in the Journal of Geophysical Research: Space Physics, Volume 128, Issue 4, article id. e2023JA031339 (2023). The pdf document is available in the online version of this journal and embedded one-to-one in this thesis. My own contribution to this work was 80%.

JGR Space Physics

RESEARCH ARTICLE
10.1029/2023JA031339

Special Section:
Fifteen Years of THEMIS Mission

Magnetosheath Jet Formation Influenced by Parameters in Solar Wind Structures

Florian Koller[1], Ferdinand Plaschke[2], Manuela Temmer[1], Luis Preisser[3], Owen W. Roberts[3], and Zoltan Vörös[3,4]

[1]Institute of Physics, University of Graz, Graz, Austria, [2]Institut für Geophysik und Extraterrestrische Physik, TU Braunschweig, Braunschweig, Germany, [3]Space Research Institute, Austrian Academy of Sciences, Graz, Austria, [4]Institute of Earth Physics and Space Science, ELRN, Sopron, Hungary

Key Points:

- We show how plasma parameters in solar wind structures are related with jet occurrence
- High cone angles and low Alfvén Mach numbers associated with the magnetic ejecta of coronal mass ejections presumably reduce the generation of jets
- We found that plasma parameters in high-speed streams represent the most favorable physical condition for jet generation

Correspondence to:
F. Koller,
florian.koller@uni-graz.at

Citation:
Koller, F., Plaschke, F., Temmer, M., Preisser, L., Roberts, O. W., & Vörös, Z. (2023). Magnetosheath jet formation influenced by parameters in solar wind structures. *Journal of Geophysical Research: Space Physics*, *128*, e2023JA031339. https://doi.org/10.1029/2023JA031339

Received 20 JAN 2023
Accepted 23 MAR 2023

Author Contributions:
Conceptualization: Florian Koller, Ferdinand Plaschke, Manuela Temmer, Luis Preisser, Owen W. Roberts
Data curation: Florian Koller
Formal analysis: Florian Koller
Funding acquisition: Ferdinand Plaschke, Manuela Temmer, Owen W. Roberts
Investigation: Florian Koller, Luis Preisser
Methodology: Florian Koller, Ferdinand Plaschke, Zoltan Vörös
Project Administration: Manuela Temmer, Owen W. Roberts

Abstract Magnetosheath jets are dynamic pressure enhancements observed in the terrestrial magnetosheath. Their generation mechanisms are currently debated but the majority of jets can be linked to foreshock processes. Recent results showed that jets are less numerous when coronal mass ejections (CMEs) cross the magnetosheath and more numerous when stream interaction regions (SIRs) cross it. Here, we show for the first time how the pronounced substructures of CMEs and SIRs are related to jet production. We distinguish between compression and magnetic ejecta (ME) regions for the CME as well as compression region associated with the stream interface and high-speed streams (HSSs) for the SIR. Based on THEMIS and OMNI data covering 2008–2021, we show the 2D probability distribution of jet occurrence using the cone angle and Alfvén Mach number. We compare this distribution with the values within each solar wind (SW) structure. We find that both high cone angles and low Alfvén Mach numbers within CME-MEs are unfavorable for jet production as they may inhibit a well-defined foreshock region. 1D histograms of all parameters show, which SW parameters govern jet occurrence in each SW structure. In terms of the considered parameters the most favorable conditions for jet generation are found for HSSs due to their associated low cone angles, low densities, and low magnetic field strengths.

Plain Language Summary The Sun produces a constant outflow of particles and magnetic field called the solar wind (SW). The Earth's magnetic field diverts that flow and protects us from these particles. A shock wave is built up between the Earth's magnetic field and the SW. This leads to a turbulent region called the Earth's magnetosheath. Within the magnetosheath, we regularly find faster or denser flows of particles, which we call jets. The formation of these jets is an active area of research. In this work we look at times where the Sun bursts out huge particle clouds (coronal mass ejections [CMEs]) and times when the SW is faster and piles up plasma like a snowplow. We look at how the particle clouds and the fast SW affect the jet generation. We compare conditions in the SW with CMEs and fast SW flow. We also examine the SW conditions during jet generation. CMEs decrease jet generation due to their strong magnetic fields and their magnetic field angles. This leads to changes in the properties of the bow shock unfavorable for jet generation mechanisms. The conditions in fast SW are more favorable, leading to more jet generation.

1. Introduction

The magnetosheath is the region of shocked solar wind (SW) plasma sunward of the Earth's magnetosphere. Němeček et al. (1998) first reported that the magnetosheath regularly shows structures with dynamic pressure enhancements, which we shall call jets in the present work. Jets can show an increase in dynamic pressure up to 15 times compared to the surrounding plasma (Plaschke et al., 2013). Their median size is estimated to be 0.1 R_e but can reach up to more than 2 R_e (Plaschke et al., 2016, 2020). Large jets in particular can be geoeffective (Hietala et al., 2018; Norenius et al., 2021; Nykyri et al., 2019) and appear several times per hour (Plaschke et al., 2016).

Recently, several generation mechanisms were proposed to explain the occurrence of magnetosheath jets (Plaschke et al., 2018). Most mechanisms explain jets as a result of different processes in the foreshock region and are therefore associated with the quasi-parallel bow shock. The foreshock can only build up due to back-streaming ions from a super-critical bow shock and is therefore dependent on a high Alfvén Mach number (Balogh & Treumann, 2013), which is defined as $M_A = v_{sw}/v_A$, with v_{sw} denoting the SW velocity, and $v_A = B/\sqrt{\mu_0 \rho}$ (with

Software: Florian Koller, Ferdinand Plaschke
Supervision: Ferdinand Plaschke, Manuela Temmer, Owen W. Roberts
Validation: Florian Koller
Visualization: Florian Koller, Manuela Temmer
Writing – original draft: Florian Koller, Manuela Temmer
Writing – review & editing: Florian Koller, Ferdinand Plaschke, Manuela Temmer, Luis Preisser, Owen W. Roberts, Zoltan Vörös

B being the magnetic field strength, μ_0 the magnetic permeability and ρ the SW density, respectively) defining the Alfvén velocity. The foreshock is formed upstream of the quasi-parallel shock front and therefore requires a low shock normal angle Θ_{Bn} (Eastwood et al., 2005). The interplanetary magnetic field (IMF) cone angle ($\arccos|B_x|/|B|$, with B_x denoting the magnetic field strength in GSE-X, with GSE being the geocentric solar ecliptic coordinate system) is often used as a good approximation for Θ_{Bn} for the subsolar region (see e.g., Plaschke et al., 2013; Raptis et al., 2020; Vuorinen et al., 2019). Θ_{Bn} is identical to the cone angle at the subsolar point at the nose of the bow shock. Bow shock models are required to get Θ_{Bn} at positions far away of the subsolar point due to the curved geometry of the shock.

It has been shown that jets appear more often during low cone angle periods (Gutynska et al., 2015; LaMoury et al., 2021; Plaschke et al., 2013; Vuorinen et al., 2019). Different phenomena in the foreshock can cause ripples in the bow shock (Balogh & Treumann, 2013). The way in which the SW is processed by the rippled shock has been proposed to be the cause for jet generation (Hietala et al., 2009; Hietala & Plaschke, 2013; Preisser et al., 2020). At the ripple, the local oblique shock front may cause the deceleration of the incoming SW plasma to be less efficient in the GSE-X direction in comparison to the less oblique shock surroundings. It would create a flow (jet) in the downstream side of the shock that is faster than the surrounding shocked and decelerated plasma. This effect as well as the integration of fast foreshock flows into the magnetosheath might also be a consequence of short large-amplitude magnetic field structures (SLAMS) forming in the foreshock (Karlsson et al., 2015; Palmroth et al., 2018b; Schwartz & Burgess, 1991). The latest simulations have shown that the majority of jets can be related to foreshock compressional structures (Suni et al., 2021). Recently, Raptis, Karlsson, Vaivads, Pollock, et al. (2022) presented evidence that jets can be generated as a consequence of the bow shock reformation process at the quasi-parallel shock front itself. This has been also proposed to be a mechanism for the formation of paramagnetic embedded plasmoids based on hybrid simulations (Preisser et al., 2020). Hietala and Plaschke (2013) estimated that the majority (97%) of jets can be associated to bow shock rippling. A subset of jets can be explained by other mechanisms. For example, Archer et al. (2012) suggested that rotational discontinuities in the magnetic field cause pressure pulses in the magnetosheath when there is a change from the quasi-parallel to the quasi-perpendicular shock region and vice-versa.

In a recent statistical study Koller et al. (2022) analyzed jet occurrence within large scale SW structures, such as coronal mass ejections (CMEs) and stream interaction regions (SIRs) together with their high-speed streams (HSSs). It was found that jets are less frequent when the magnetic ejecta (ME) region of the CME passes Earth.

In comparison to quiet SW conditions and compressed SW for SIRs, CMEs and their ME regions present "laboratories" with very different SW conditions. Typically, when CMEs exceed the speed of the fast magnetosonic wave they drive a shock and behind it the CME-sheath region is built up showing an increase in velocity, density and magnetic field (see e.g., Kilpua et al., 2017). Recent results revealed, that the sheath region covers two separate density structures of compressed and piled up SW, namely the sheath and leading edge (LE) (see Temmer & Bothmer, 2022), which is driven by the strong and smoothly rotating magnetic flux rope. The CME compression region (sheath and LE) is, in contrast to the flux rope, very turbulent and the cone angle can change rapidly within a short time. Figure 1 shows a CME example measured by the Active Composition Explorer (ACE, Stone et al., 1998). In the present work, we therefore investigate on the basis of these recent results the physical mechanism of the decrease in jet occurrence of jets. The results will give us a better understanding of jet production mechanisms. We hypothesize that the conditions inside the CME-ME pose difficulties for the building of a foreshock in the subsolar region that can produce highly non-linear structures. Due to the twisted magnetic field lines in the flux rope inside of the ME, the cone angle could differ greatly from radial IMF conditions. Based on cone angle measurements, Turc et al. (2016) showed that during the majority of magnetic clouds that arrived at Earth, the subsolar bow shock configuration is quasi-perpendicular. Radial IMF lines however seem to be a necessary condition to generate a quasi-parallel shock region that builds the foreshock. In addition to that, the high magnetic field strength and low density inside a CME-ME cause an increase in Alfvén velocity. Thus, the Alfvén Mach number decreases, causing a decrease in the strength of the bow shock (see Lavraud & Borovsky, 2008). The sum of all these effects generated by the arrival of the CME-ME to the bow shock could inhibit the building of a foreshock region that can efficiently generate jets near the subsolar point.

Similar to CME-sheaths, SIRs consist of compressed SW due to HSSs originating from coronal holes (Jian et al., 2006; Temmer, 2021). Figure 2 shows an example of a SIR and its HSS using OMNI data (King & Papitashvili, 2005). The SIR compression region is turbulent with strongly increased density and magnetic field.

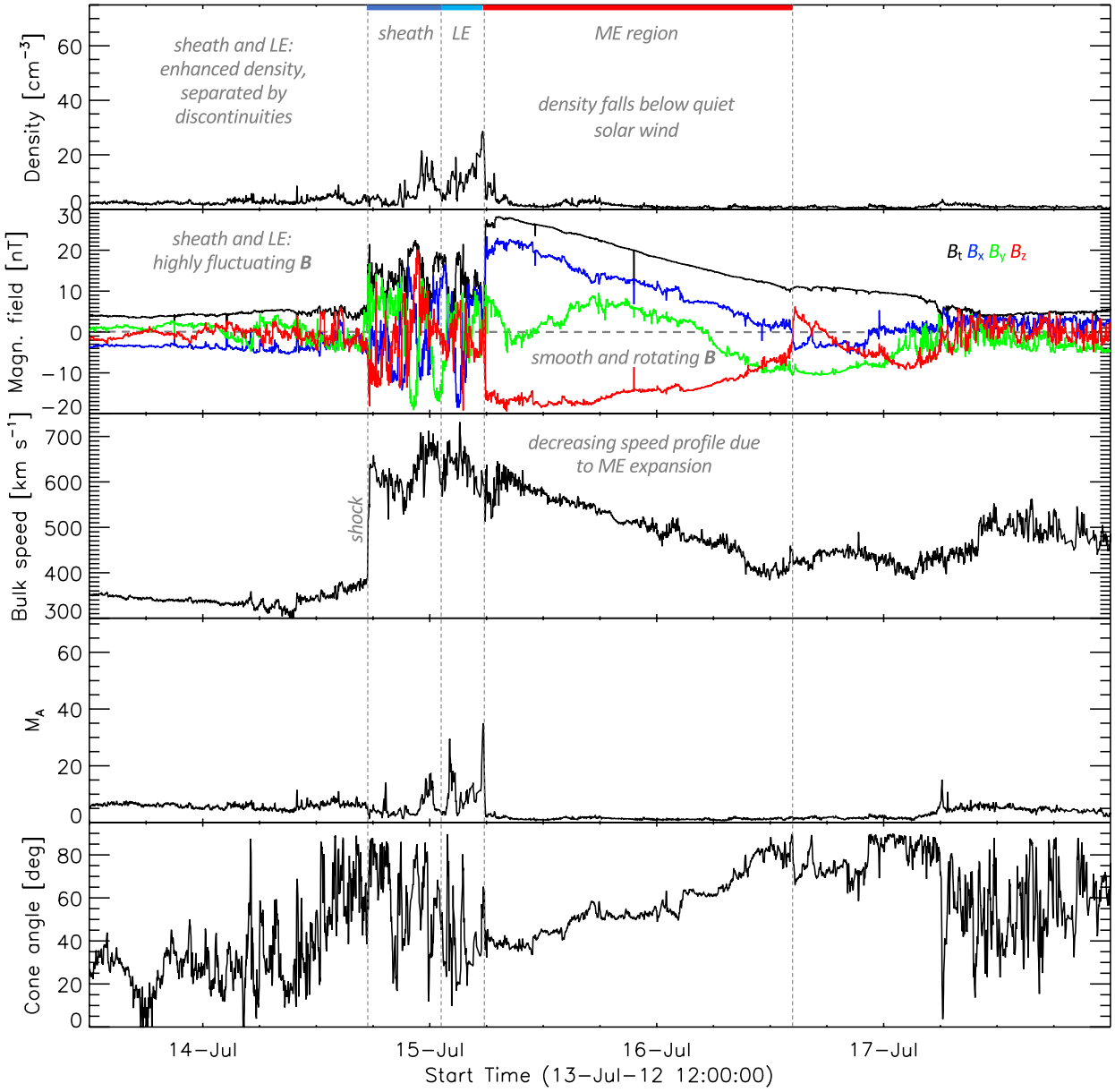

Figure 1. Example of a coronal mass ejection (CME) from active composition explorer measurements. The three panels from top to bottom show the measured proton density, total magnetic field and vector components in geocentric solar ecliptic coordinates (see legend), and the proton bulk speed. This CME clearly reveals the typical structures, shock, two density enhancements—sheath (dark blue) and leading edge (LE, light blue)—separated from each other by discontinuities and forming the highly turbulent compression region. The LE is followed by the magnetic ejecta (ME) with the twisted magnetic field components. The next two panels give the Alfvén Mach number and the cone angle (see more details in the text).

HSSs that drive the compression show a fast flow speed and low density. Unlike CME-MEs, the magnetic field strength inside HSSs does not exhibit an exceptionally enhanced structure. Because of this combination of parameters, high Mach numbers are expected within the HSSs. Low cone angles are statistically expected to appear more often compared to quiet SW due to the fast flow speed. SIRs last for several days and are often reoccurring after a Solar rotation (which is then called a co-rotating interaction region). The conditions for building up a foreshock near the subsolar point should be met often inside HSSs. Koller et al. (2022) found that the occurrence of jets is increased especially after the velocity peak of the HSS.

In the following we investigate jets detected by THEMIS spacecraft between 2008 and 2021 and compare the SW conditions during these times. In this way, we will identify which parameters govern jet production in each

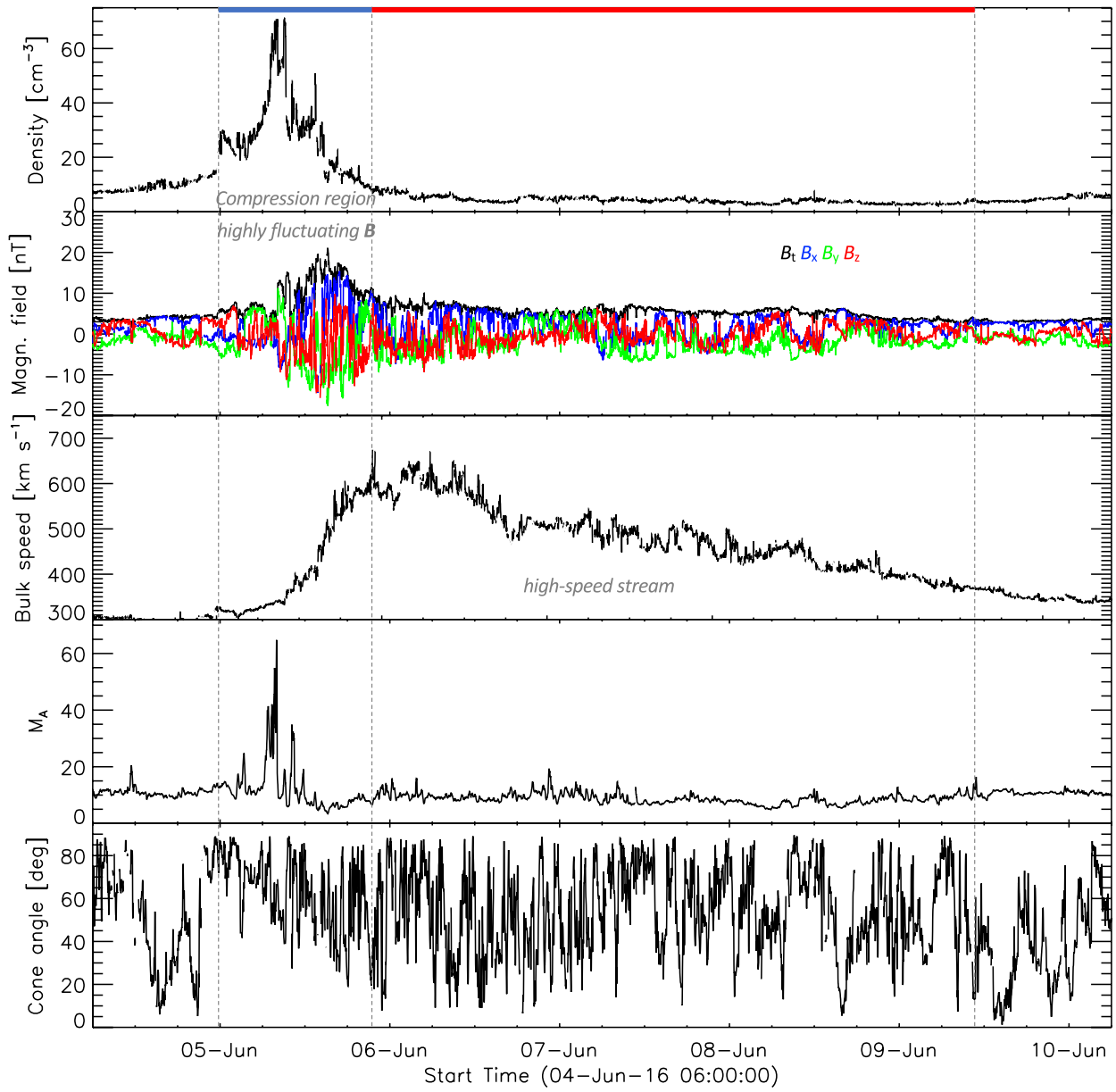

Figure 2. Example of an stream interaction region and high-speed stream from OMNI measurements. The panels show the same parameters as the previous figure.

SW structure. Initially we consider two parameters that are indicative for the existence of the foreshock near the subsolar point: cone angle and Alfvén Mach number. We then extend and complete the analysis by covering other SW parameters such as velocity, magnetic field strength, density, dynamic pressure (defined as $p_{dyn} = 0.5\rho v^2$), plasma beta, magnetosonic Mach number, and temperature and interpret the results.

2. Data

We compare in situ SW plasma and magnetic field data from OMNI during times when jets are observed with the SW measured during CMEs and as a reference during all times when magnetosheath data were available. We use 1-min resolution OMNI velocity, magnetic field, and density data. Our data covers the time range between January 2008 and December 2021.

Data from the THEMIS spacecraft (Angelopoulos, 2008) are used to detect intervals of jets in the magnetosheath. Specifically, we use the reduced ion moments (ion velocity, density, temperature, and energy flux) from the

THEMIS Electrostatic Analyzer (ESA; McFadden et al., 2008). Ion moments are available from ESA with a time resolution of 3 s. We use magnetic field measurements from the Fluxgate Magnetometer (FGM; Auster et al., 2008).

Magnetosheath intervals are determined by the same criteria used in Plaschke et al. (2013) and Koller et al. (2022): The spacecraft GSE position is restricted to 7–18 R_e and has to be within a 30° Sun-centered cone with tip at the Earth. To ensure that the spacecraft is within the magnetosheath, the ion density has to be at least twice as dense as the upstream SW. The energy flux of the 10 keV ions has to be less than those of the 1 keV ions. The magnetosheath intervals are required to be longer than 2 min. All measurements are interpolated to the same 1 s time cadence for the subsequent detection of magnetosheath jets.

Jets were defined using the criteria of (Koller et al., 2022): $p_{\mathrm{dyn,x}} > 3 \times \langle p_{\mathrm{dyn,x}} \rangle_{\mathrm{20min}}$. Here, $\langle p_{\mathrm{dyn,x}} \rangle_{\mathrm{20min}}$ denotes the 20-min running average of the magnetosheath dynamic pressure in GSE-X direction. Therefore, enhancements of the GSE-X dynamic pressure larger than three times of the surrounding plasma within 20 min are declared as jets. As additional criterion, the jet velocity has to be negative in GSE-X, and the magnetosheath GSE-X velocity 1 min before and after the jet has to be above half of the measured GSE-X velocity during the pressure peak of the jet. Magnetosheath intervals shorter than 20 min are not considered for jet detection. Jets were restricted to only those with a duration of more than 10 s. Using these criteria, we detected a total of 9704 jets within the given time range and the defined subsolar region of the magnetosheath. The number is smaller in comparison to the work by Koller et al. (2022) due to the jet duration restriction of 10 s and due to the usage of the reduced ion moments. The intervals of magnetosheath and jet times are provided at https://osf.io/s32yf/ (Koller et al., 2023).

Arrival times of ICMEs at Earth are collected from an online catalog maintained by Richardson and Cane (Cane & Richardson, 2003; Richardson & Cane, 2010). It includes a variety of information on near-Earth CMEs that have been detected since 1996. We use the start and end times of CME-MEs (labeled as ICME Plasma/Field Start, End) in our work, which are the times that were measured by ACE. We also use the time of the associated geomagnetic storm sudden commencement at Earth, which is associated with the arrival of the CME-driven shock. We define the interval between the shock arrival and the start of the CME-ME as the crossing time of the CME-sheath, covering both compression regions, sheath and LE.

The list of SIR and HSS events described in Koller et al. (2022) was used in our work. It covers the start and end times of SIRs and HSSs from 1995 until the end of 2021 based on previously published lists (Geyer et al., 2021; Grandin et al., 2019; Jian et al., 2011) which were then extended. The start times of SIRs is defined as the start of increase in density and velocity, and its end is given by the time of the peak velocity. The HSS interval time is defined by the time between the peak SW velocity and the time, when the velocity drops below the defined threshold of each list as described in Koller et al. (2022).

3. Analysis

We use OMNI data during jet intervals and during all times when we have simultaneously magnetosheath observations by THEMIS. The latter is used as a reference to determine, how the SW parameters are distributed during jet detection times. For each second of magnetosheath data, we calculate the corresponding SW Alfvén Mach number and the cone angle. Both THEMIS ion moments and OMNI data are interpolated to 1 s resolution for that purpose. We start the analysis with these parameters as they directly influence the existence of the foreshock. To check how important these parameters are for the jet occurrence, we plot a 2-dimensional (2D) histogram with the cone angle on the *x*-axis and the Alfvén Mach number on the *y*-axis. All histograms are normalized to the peak value. Bin sizes of 4.286° for the *x*-axis and 1.3 for the *y*-axis were chosen. These bin sizes ensure reliable amounts of data as well as reasonable resolution for our analysis.

We then determine the jet probability distribution as a function of Alfvén Mach number and cone angle. We do this by dividing the SW conditions that we find during jets by the overall SW conditions. The jet probability distributions shows, how the jet occurrence is related to the physical parameters, while the measured distribution during jets shows a bias toward parameter ranges with the most measurements. The result is a 2D histogram plot, where the jet probability given in percent is color-coded in each bin. As a final analysis we check, how this jet probability distribution compares to the SW conditions that we find within CME-sheaths, CME-MEs, SIRs and HSSs.

The analysis is extended to a wider set of SW parameters by using 1D histograms similar to LaMoury et al. (2021) and Plaschke et al. (2013). We investigate how the conditions differ in each type of SW structure as well as in the non-structured SW. We compare these conditions with the jet probability in percent for each SW parameter using histograms. We show the correlation matrix of the SW parameter to give context to the dependence of every parameter with each other.

We give uncertainty estimations for the jet probability in both 2D histograms and 1D histograms. We use bootstrapping to infer the uncertainties and to check, how robust the results are: A random subsample of the overall distribution is taken and the jet occurrence is evaluated with this subsample. This process is repeated 100 times, resulting in 100 different results. For each bin, we take the standard deviation of the resulting range as our measure of error. The size of the random subsample is 1/300th of the original dataset. Our dataset is using 1 min-OMNI values that were interpolated to a resolution of 1 s. Therefore, a random subsample of 1/300th of the original sample size roughly corresponds to 20% of the measured OMNI distribution. The uncertainties are displayed as an additional plot for the 2D histograms and as errrorbars in the 1D histograms.

4. Results

Figure 3a shows the 2D histogram distribution for the SW condition during all times when we have magnetosheath observations. The SW condition peak at cone angles of 40–90° and Alfvén Mach numbers around 5–12. This distribution serves as a reference for the further analysis. The white contour indicates all bins where we have more than 5 hr/20 hr of measurements available. The distribution of SW conditions during jets is shown in Figure 3b. We find that jets appear dominantly during cone angles of 20–50 and Alfvén Mach numbers of 6–11.

Figure 3c shows the jet probability in percent. Here, the distribution of SW conditions during jets is divided by the reference SW distribution. All bins with less than 5 hr of data outside of the white contour in Figure 3a were omitted. Table 7 in Koller et al. (2022) gives a mean value of roughly 1–3 jets per hour. Therefore, we can expect at least 5–15 jets for each bin within the given 5 hr contour. Figure 3d shows the corresponding uncertainties for each bin of Figure 3c. As expected, jets are found predominantly at lower cone angles, mostly at values lower than 40°. Jets are rarely detected during intervals with high cone angles (>60°). The jet probability decreases drastically for cone angles between 40–60°, with a slight trend of decreasing jet percentage for lower Alfvén Mach numbers. During these conditions, the probability to detect jets is roughly 9–15 times lower compared to times of low cone angle (<40°) and high Alfvén Mach numbers (>5). This value is similar or slightly higher to the probability of detecting jets downstream of the quasi-parallel shock compared to the quasi-perpendicular shock found by Archer and Horbury (2013). Figure 3c hints that the jet probability at low Alfvén Mach numbers (<5) is decreasing even for intermediate cone angles (40–50°), albeit with a low amount of data available in this regime.

This distribution is compared with the conditions found within SW structures given by Figure 4. Black contours in each panel indicate where we have more than 2 or 10 hr of available data per bin. Figure 4a shows the mean SW distribution for cone angle and Alfvén Mach number in CME-sheaths. The distribution is mostly confined to cone angles higher than 65° and Alfvén Mach numbers between 3 and 9. It matches the area of lowest jet probability from Figure 3c.

The mean SW conditions that we can find during CME-MEs is shown in Figure 4b. The same bin sizes from the previous plot were chosen. The distribution is mostly confined to cone angles higher than 60° and Alfvén Mach numbers between 2 and 5. It is similar to the CME-driven sheaths, with the major difference being the lower Alfvén Mach numbers. It again matches with the parameter distribution least likely to show jet occurrence.

Figure 4c shows the mean SW distribution for cone angle and Alfvén Mach number for SIRs. The data shows a broader range compared to the distributions associated with CMEs. The distribution is confined mostly to the area at cone angles between 30 and 85° and Alfvén Mach numbers between 3 and 11.

Figure 4d shows the mean SW distribution for cone angle and Alfvén Mach number for HSSs. A narrow distribution is seen for the Alfvén Mach number, ranging from 6 to 13, while the cone angle covers a wide range with values between 15 and 90°. Comparing with the probability distribution for jets seen in Figure 3c, HSSs show the most overlap with conditions that are favorable for the jet generation.

Figure 5 shows 1D histograms for other SW parameters when jets were detected, during all times of simultaneous magnetosheath measurements and the probability distribution for jet occurrence. The plasma beta in

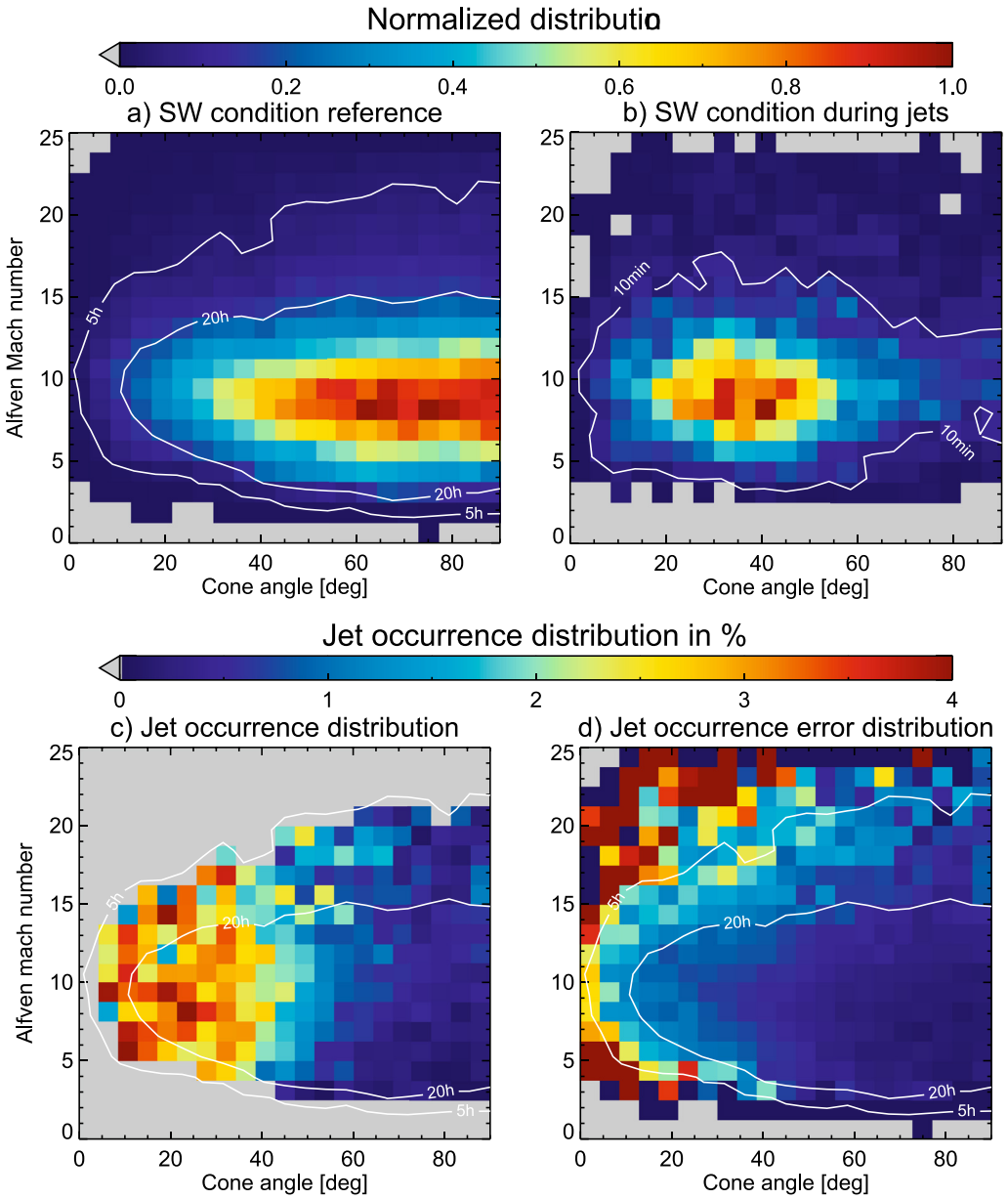

Figure 3. 2D histogram showing normalized distributions of cone angle and Alfvén Mach number. Plot (a) shows the overall distribution of both parameter in the solar wind (SW) during all observation times. Plot (b) shows the SW parameter distribution during jet detection. Plot (c) shows the jet probability depending on both parameters, where the percentage of detecting a jet is color coded. The data was restricted to all times with more than 5 hr of available data, as indicated by the white contour in panel (a). Plot (d) shows the uncertainty estimation for each bin in plot (c) using the same range of value.

panel (f) is defined as $\beta = 2\mu_0 n k_B T/B^2$, with μ_0 being the vacuum magnetic permeability, n the number density, k_B the Boltzmann constant, and T the temperature. The magnetosonic Mach number in panel (h) is defined as $M_M = v_{SW}/\sqrt{v_A^2 + c_s^2}$, with c_s being the speed of sound in the SW. The Y-Axis for the jet probability is the same for each panel in Figure 5. This helps to visualize and compare the impact of each parameter on the jet probability. Uncertainties for the jet probability are shown as errorbars in each panel. The trends for the jet probability at high and low values for each parameter are summarized in Table 1. The jet probabilities for a defined lower and upper range for each SW parameter are given. The cone angle shows the largest influence on the probability. Plasma beta, Alfvén Mach number, and magnetosonic Mach number see a drop in percentage at low values. A drop in jet percentage is notable for high magnetic field strengths. Both density and dynamic pressure have a higher jet

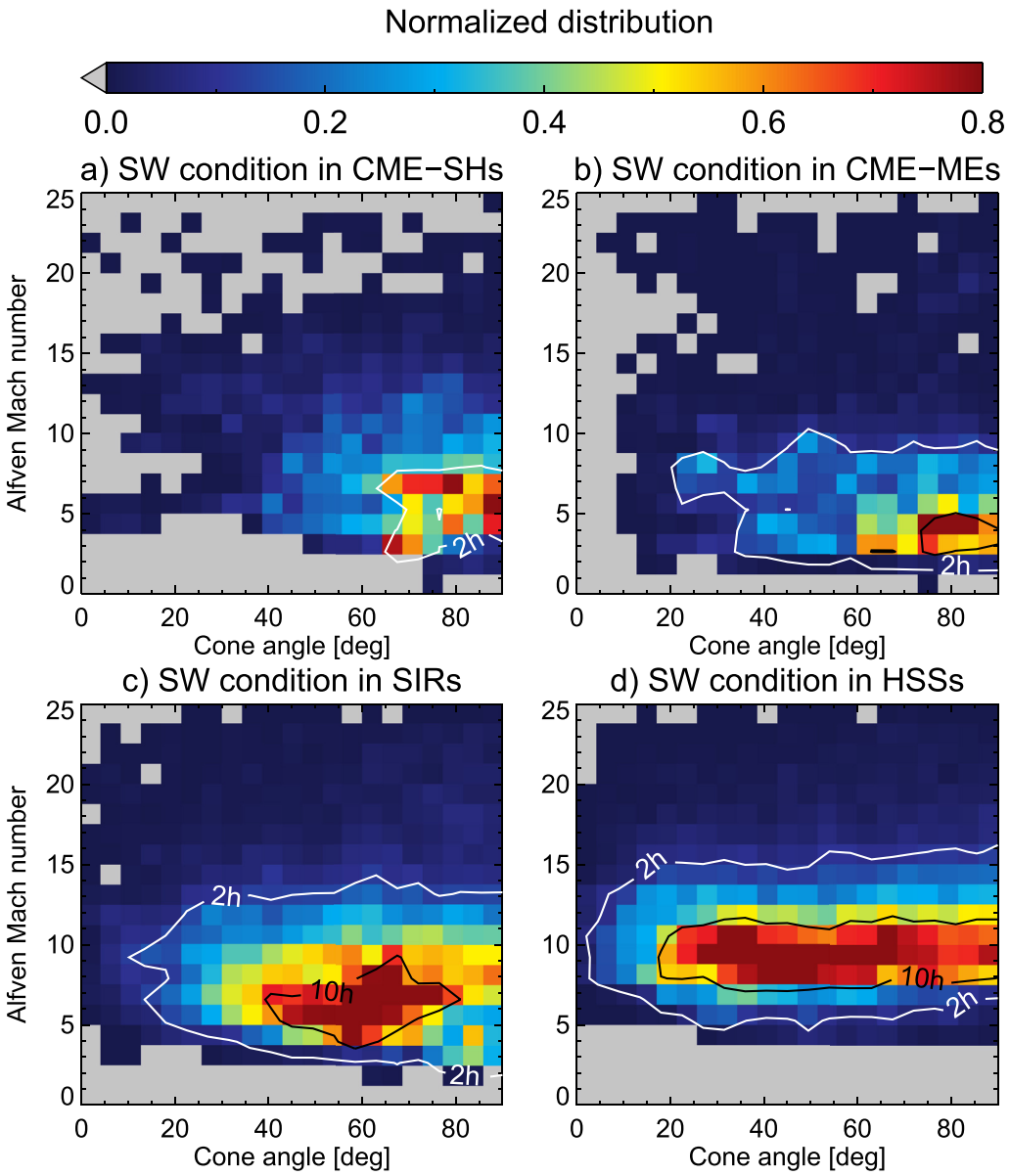

Figure 4. 2D histogram showing normalized distributions of cone angle and Alfvén Mach number for each type of solar wind (SW) structure: (a) during coronal mass ejection (CME)-sheaths, (b) during CME-magnetic ejectas (MEs), (c) during stream interaction regions (SIRs) and (d) during high-speed streams (HSSs). Contours indicate the number of available hours for each bin. The maximum value of the color scale is set to 0.8 to increase the visibility of the distribution.

percentage at lower values, while the total velocity shows a jet percentage increase at higher values. The SW temperature seems to be the parameter with the least influence, showing moderately higher jet percentages at high values. These results largely agree with the results given in LaMoury et al. (2021, dashed line in Figure 4).

The Spearman correlation coefficients between each parameter in the SW is given in Figure 6 to give context to the previous figure. Some of these parameters are revealed to be highly correlated. This analysis uses the overall SW without differentiation between each structure and we derive some of well-known relations. SW velocity is anti-correlated with density (−0.61) and plasma beta (−0.41) and correlated with temperature (0.76), magneto-sonic Mach number (0.32), magnetic field strength (0.22), and dynamic pressure (0.21). The cone angle has the weakest correlation with the other given parameters (0.17 with magnetic field strength, −0.16 for temperature, 0.11 for dynamic pressure and −0.1 for velocity). The magnetic field is anti-correlated with the Alfvén Mach number (−0.86), plasma beta (−0.78), and magnetosonic Mach number (−0.68) and shows some correlation

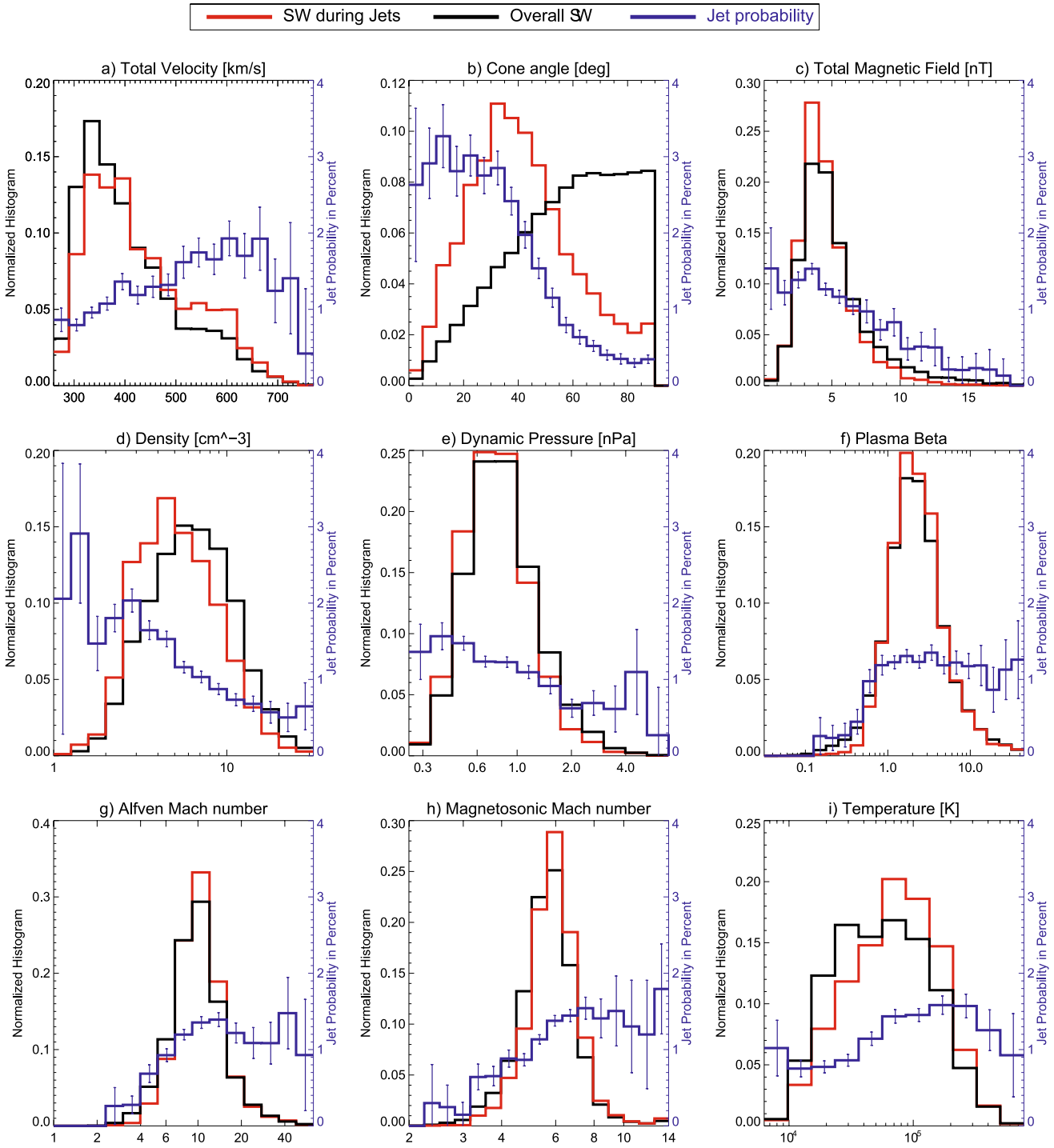

Figure 5. 1D parameter histograms showing solar wind parameter distributions during jet detection (red) and during all available sheath times (black). The jet probability distribution in percent is given in blue. Estimations for the uncertainties in the jet probability distribution are derived using bootstrapping.

with dynamic pressure (0.4) and temperature (0.28). The SW density correlates with dynamic pressure (0.6) and plasma beta (0.33) and is anti-correlated with temperature (−0.43) and magnetosonic Mach number (−0.23). Plasma beta is strongly correlated with the Alfvén Mach number (0.9), correlates with magnetosonic Mach number (0.52), and is anti-correlated with temperature (−0.28). The Alfvén Mach number correlates with the magnetosonic Mach number (0.82).

Table 1
Mean Jet Probability at Low and High Ranges for Each Solar Wind Parameter Given in Figure 5

	Low range	Jet probability	High range	Jet probability
Total velocity	<400	1.0	>500	1.7
Cone angle	<40	2.8	>60	0.4
Total magnetic field	<6	1.3	>10	0.4
Density	<4	1.8	>10	0.6
Dynamic Pressure	<0.6	1.46	>2	0.7
Plasma beta	<0.5	0.3	>0.5	1.2
Alfvén Mach number	<5	0.5	>7	1.3
Magnetosonic Mach number	<3	0.2	>6	1.5
Temperature	<60,000	0.9	>60,000	1.5

Figures 7 and 8 show 1D histograms for SW parameter during each type of large-scale SW structure analyzed in this work. In addition to that, Figure 9 shows the distribution for non-structured SW. The overall jet probability from Figure 5 is displayed in each case to connect the parameters with the jet occurrence.

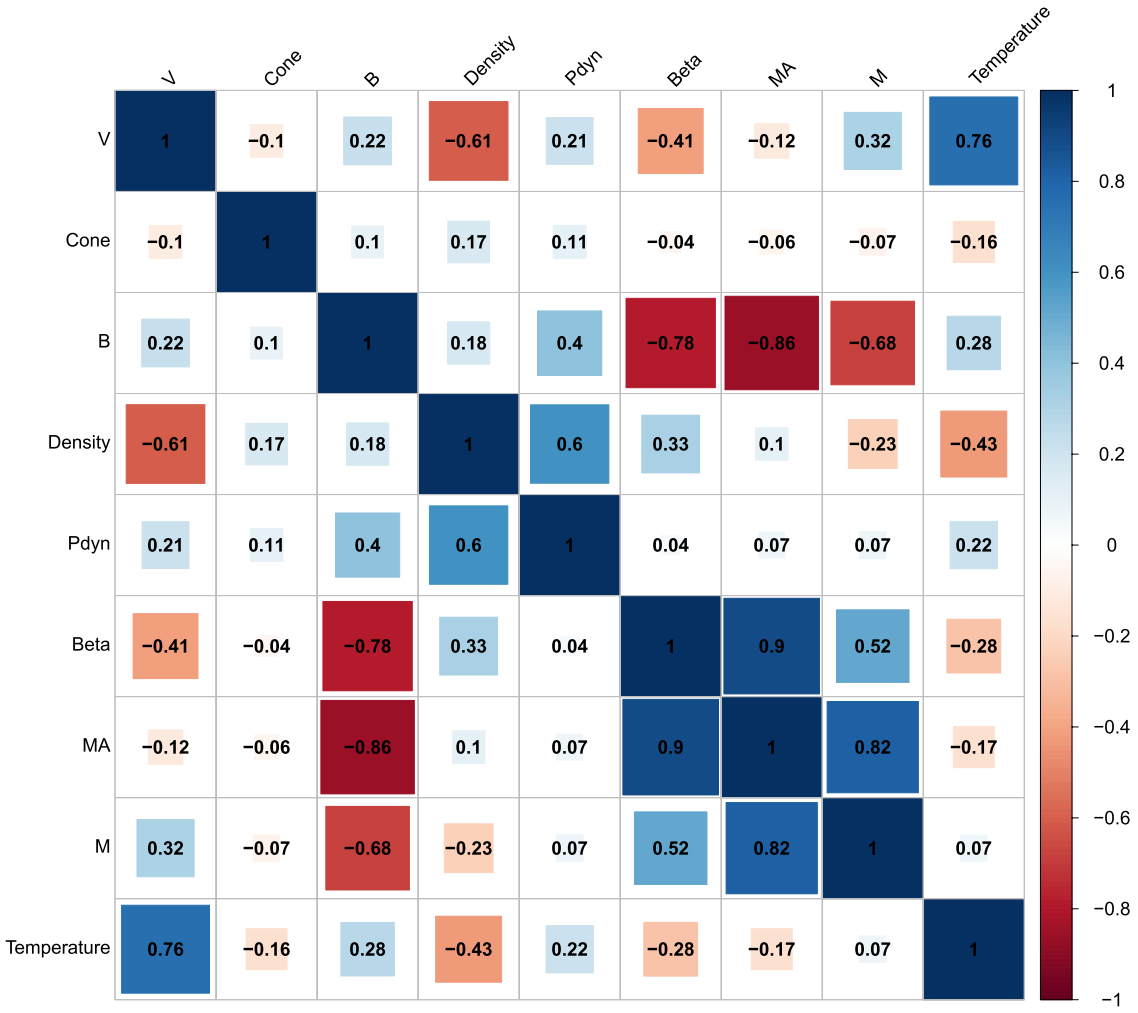

Figure 6. Spearman correlation coefficients for the nine solar wind parameters displayed in Figures 5–9. The correlation coefficients are calculated using OMNI data during all times of simultaneous magnetosheath measurements by THEMIS.

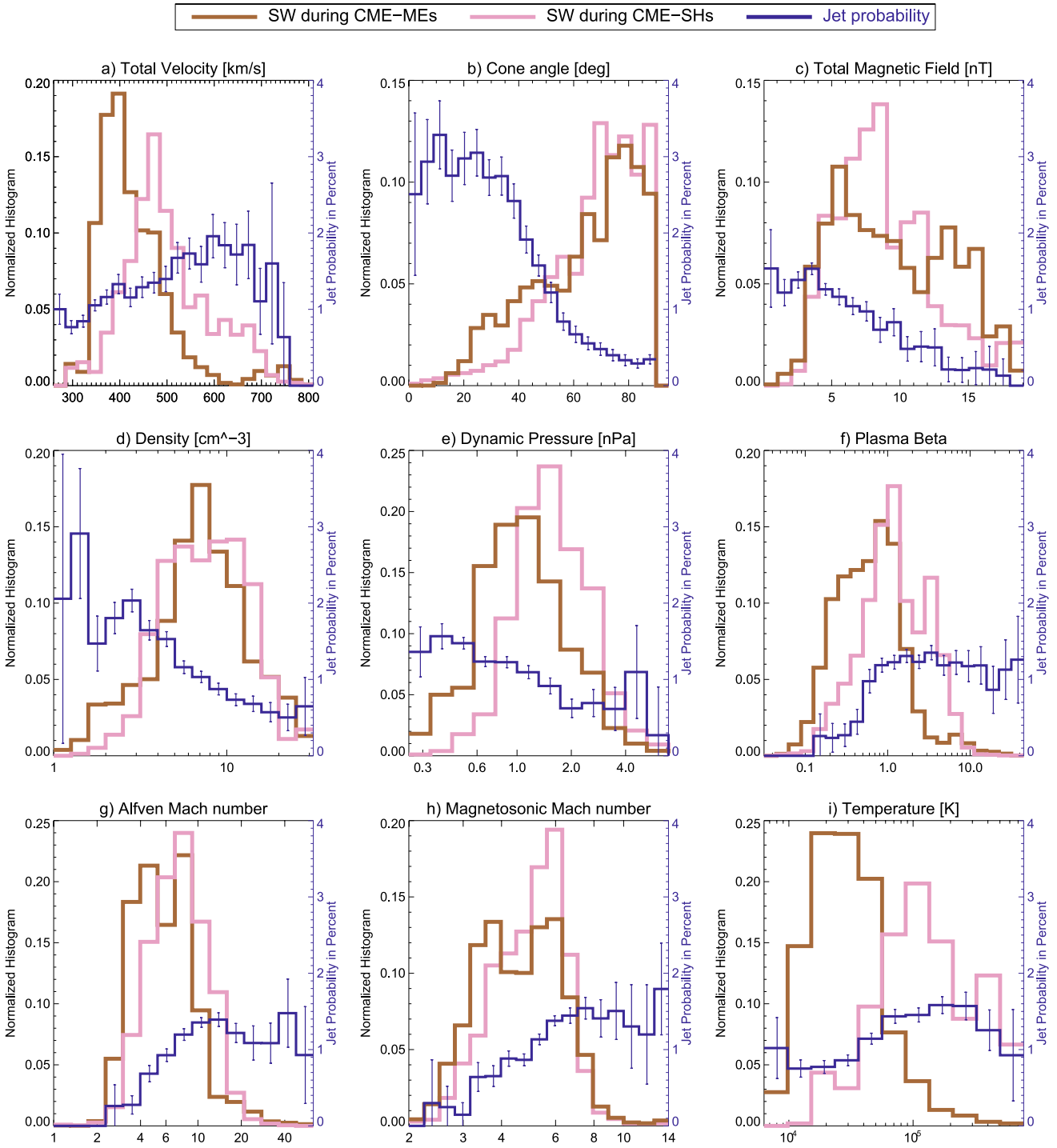

Figure 7. 1D parameter histograms for the solar wind distribution in coronal mass ejection (CME)-sheaths and CME-magnetic ejecta (ME) compared to the overall jet probability distribution.

Histograms of CME-ME and CME-sheath show a variety of parameter distributions unfavorable for jet occurrence as seen in Figure 7. Particularly, their high cone angles, high magnetic field strength, low plasma beta, and low Alfvén Mach number match with the decrease in jet occurrence. The velocity is increased in both structures (especially in the CME-sheath) compared to mean SW conditions, which usually favors jet occurrence. CME-sheaths show higher dynamic pressure than CME-MEs, which is statistically less favorable for jets. On

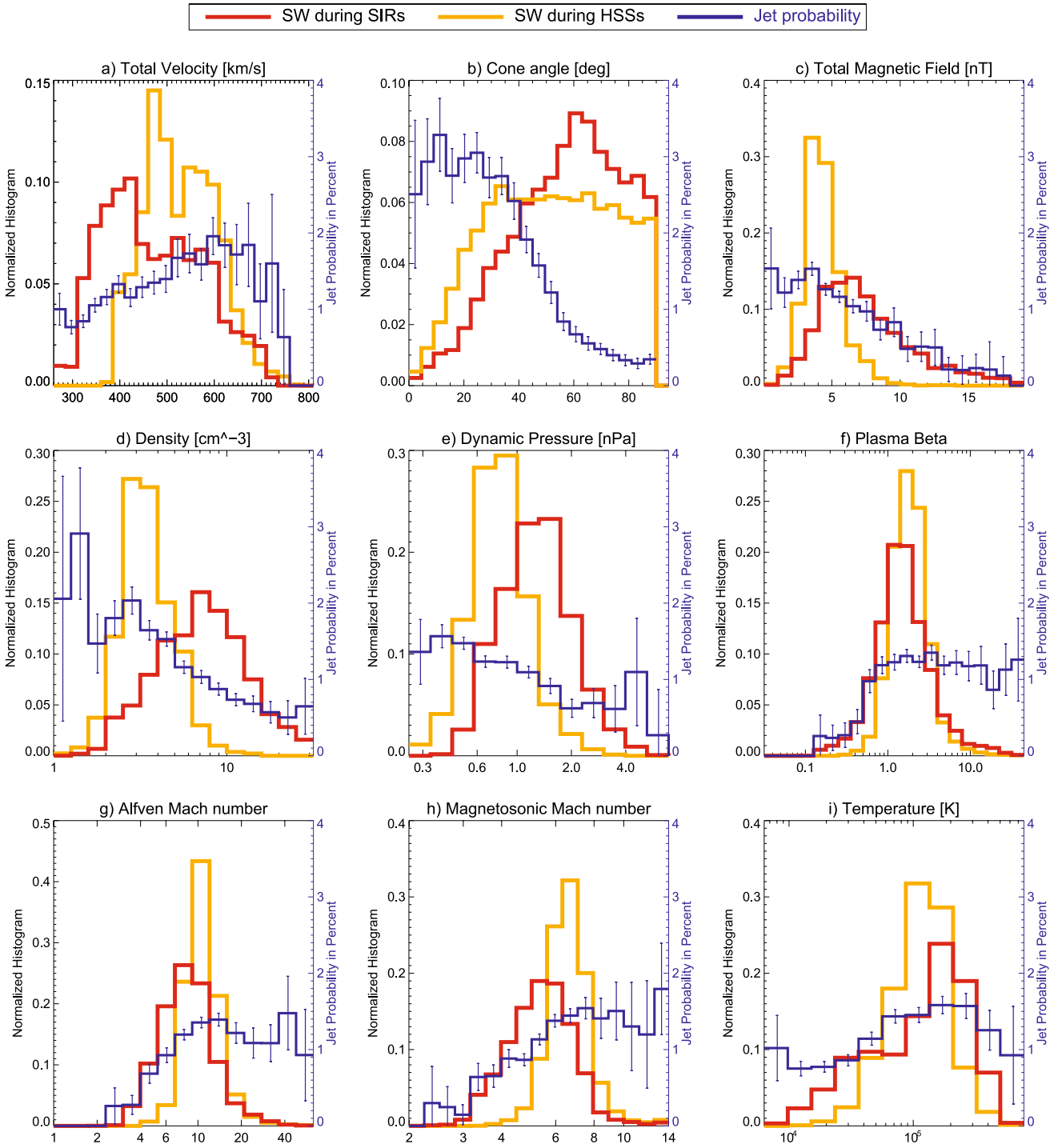

Figure 8. 1D parameter histograms for the solar wind distribution in stream interaction regions and high-speed streams compared to the overall jet probability distribution.

the other hand, CME-MEs have less favorable conditions in plasma beta, Alfvén Mach number, and temperature compared to CME-sheaths.

Figure 8 shows the distribution of parameters found in HSSs and SIRs. The parameter distribution in HSSs in particular co-align with an increase in jet occurrence in every single parameter. In particular the tendency toward low cone angles, the consistent low magnetic field strength, low density, and high velocity results in a higher jet

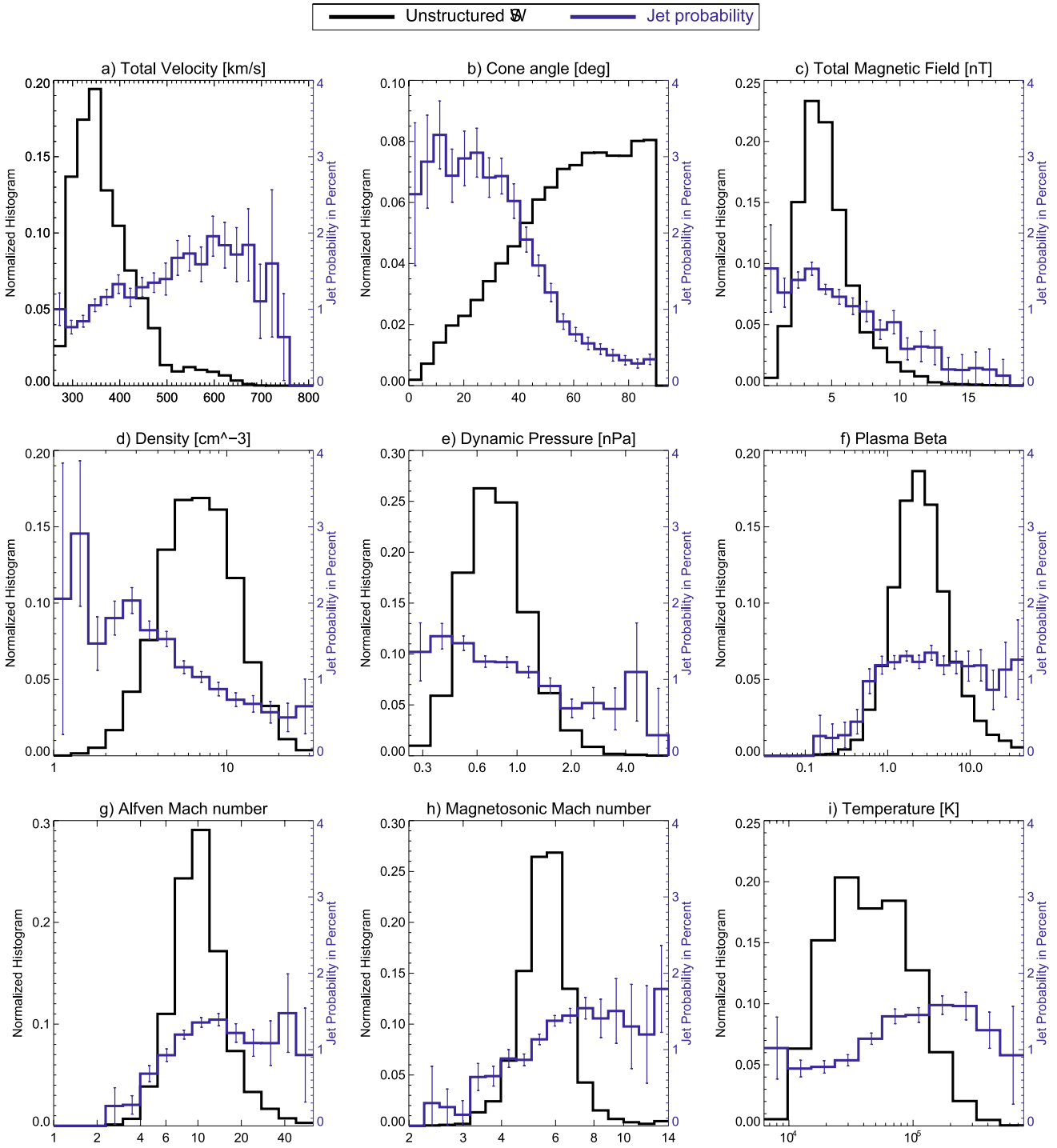

Figure 9. 1D parameter histograms for the solar wind (SW) distribution during non-structured SW compared to the overall jet probability distribution.

occurrence in HSSs compared to every other SW structure. SIRs show favorable conditions for jets in velocity and temperature compared to the mean SW. However, the cone angle distribution is skewed toward higher angles and the magnetic field, density, and dynamic pressure are increased, which is less favorable for jet occurrence.

The distribution of non-structured SW is given in Figure 9. It mostly shows the slow SW because all time periods of high velocity come from structured SW. The unstructured SW shows more favorable distributions for jet generation in several parameters compared to some other SW structures. The distribution in cone angle, magnetic

field strength, dynamic pressure, plasma beta, Alfvén Mach number, and magnetosonic Mach number favors jet occurrence during quiet SW times over CME-MEs and CME-sheaths. Slow SW, high density, high cone angle and low temperature show less favorable distributions for non-structured SW.

5. Discussion and Conclusion

We analyze in detail how the distinct conditions within SW large-scale structures such as SIRs and CMEs influence the parameters necessary to generate jets efficiently. According to the results in Figure 8, HSSs coming from solar coronal holes appear to be the ideal condition under which jets can form. They have a high probability to show low cone angles, high velocity, sufficiently high Alfvén Mach number and plasma beta, low magnetic field strength, and low density. In fact, numerous case studies analyzed magnetosheath jets that were generated during times of SW HSSs (see Archer et al., 2019; Escoubet et al., 2020; Hietala et al., 2009, 2012, 2018; Nykyri et al., 2019; Němeček et al., 1998; Raptis, Karlsson, Vaivads, Lindberg, et al., 2022). The SW parameter distributions in HSSs are very narrow by definition due to the high SW speeds and consequently low SW density. HSSs can have long durations and are rather stable, lasting for several days.

SIRs show a wide range of SW conditions due to our definition of their start-and end time: they start at the onset of density + velocity increase and end at the peak of SW velocity. Within this time, the density increases to a sharp peak and drops down to a minimum value, which should roughly coincide with the peak velocity. Therefore, these time ranges cover a range of density from low to very high values and velocities from quiet SW up to the peak velocity. With the compressed SW, an increase in magnetic field strength is expected as well as an increase in temperature due to the compression. The cone angle distribution, especially below 45°, is similar to non-structured SW, thus the overall effect on jet generation will be governed by other parameters. The increased velocity in SIRs favor jet generation, while the increased mean magnetic field strength works against it. The net effect on jet generation based on these statistics appears to be roughly zero, which is in agreement with the findings shown in Koller et al. (2022). There is still the possibility to generate jets through sudden changes in the orientation of the magnetic field due to the compression region, which needs further investigation using case studies.

The lowest number of jets is found within CME-MEs (Koller et al., 2022) and can be explained by the high cone angle that renders the building of a foreshock difficult. With Θ_{Bn} (and as proxy the cone angle) having the most influence on the jet production, the foreshock would build up at positions far away from the Earth-Sun line (as sketched in Figure 1 by Vuorinen et al., 2019). The Foreshock and its properties have been observed at positions far away from the subsolar region in recent studies (Turner et al., 2020; Vu et al., 2022) as well as simulations (e.g., in Palmroth et al., 2018a). In addition to this, sufficiently weak Alfvén Mach numbers might hinder the backstreaming of ions and thus the building of the foreshock and the reformation of the quasi-parallel bow shock. Alfvén Mach numbers below 5 are rare considering the overall distribution of the SW. However, low Alfvén Mach numbers are very common conditions found within CME-MEs. Turc et al. (2018) analyzed foreshock properties during enhanced IMF strength similar to CME-MEs in hybrid-Vlasov simulations. They found that foreshock structures have smaller scales in CME-ME- like conditions. They also discuss that the shock rippling may occur at smaller scales as well, which directly connects to proposed jet generation mechanisms. Our findings regarding the jet occurrence in relation to SW conditions are further supported by simulation results done recently by Tinoco-Arenas et al. (2022). The appearance of jets ceased at shocks with very low Alfvén Mach numbers. Similarly, high Θ_{Bn} angles (here as a proxy we use the cone angle at the subsolar point) caused a reduction of jet production in their simulations.

A higher number of jets in CME-sheaths compared to CME-MEs are reported in Koller et al. (2022). However, both CME-sheath and CME-ME show cone angles dominantly in the range of 70–90°. In fact, the cone angle distribution for CME-sheaths is even more inclined toward high cone angles than CME-MEs as seen in Figure 7. This indicates that other parameters dominate the enhanced jet generation within CME-sheaths. Differences between CME-sheath and CME-ME are found for the mean Alfvén Mach number, plasma beta, velocity, and temperature that are higher for CME-sheaths. The jets during CME-sheaths might also be caused by the rapidly changing cone angle due to the turbulent compressed plasma, which might cause pressure pulses in the magnetosheath similar to the ones proposed in Archer et al. (2012). However, this needs further investigation in specific case studies.

As all events are restricted to times where THEMIS spacecraft were in the magnetosheath, the orbit and time of the year is an implicit factor in the given distribution of the SW parameters. CME-MEs and CME-sheath are

more short-lived compared to SIRs and HSSs, which reduces the amount of data for the analysis (see Table 1 in Koller et al., 2022). This might explain statistical differences between the parameter distribution given in this work compared to other statistical works on SW parameters (Yermolaev et al., 2021).

While the number of detected jets is significantly lower within CMEs (Koller et al., 2022), there is still a non-vanishing amount of them. Whether CME generated jets are different compared to those occurring during low- cone angle and high-Alfvén conditions will give more insight in their generation mechanisms. According to Hietala and Plaschke (2013), 97% of all jets are generated by the bow shock rippling at the quasi-parallel shock. Kajdič et al. (2021) discussed jets that appeared behind the quasi-perpendicular shock. They showed four different cases: magnetic flux tubes in the magnetosheath that are connected to the quasi-parallel section of the shock, nonreconnecting current sheets at its upstream edge, reconnection exhausts due to a single IMF discontinuity, and mirror-mode waves. The overall probability distribution of jets that were only detected during CME-MEs (not shown) follows the same probability distribution as shown in Figure 3c. The only significant difference being that the favorable conditions for the jet generation are rarer within CME-MEs. By using a large dataset of plasma measurements that spans over more than a decade, there is also the possibility that some of these residual jets are caused by uncertainties or errors in the data. The detection threshold is based on a 20 min average value and might introduce a small number of jets in case of sudden changes in the dynamic pressure within the magnetosheath. The OMNI data might have errors or might not match the values that were measured at the spacecraft position in the magnetosheath. This would result in inaccurate SW conditions during jet detection. In-depth analysis of jet properties during CME-MEs are needed to resolve individual causes for jets behind the quasi-parallel shock.

At the planet Mercury, we also find low Alfvén Mach numbers similar to what we find within CME-MEs at 1 AU. Karlsson et al. (2016) analyzed isolated magnetic field structures within the Hermean magnetosheath (Anderson et al., 2010) as possible analogs to terrestrial jets. However, the analyzed structures had no dependence on the Θ_{Bn} distribution, and without sufficient ion moment measurements the connection to the classical magnetosheath jets detected at Earth remains uncertain. Sundberg et al. (2015) suggested that at low Mach numbers the backstreaming ions might not be sufficient for the self-reformation of the quasi-parallel shock, and therefore prohibits the formation of strongly non-linear structures like SLAMS. This could be similar to what we see at the Earth's bow shock during CME-MEs. Based on our result, we postulate that the number of jets within the Hermean magnetosheath would be low. The BepiColombo mission will insert into an orbit around Mercury between December 2025 and March 2026 (Milillo et al., 2020). This mission will give new insights on the jet occurrence and generation at the Hermean magnetosheath and foreshock.

In summary, we show the distribution of SW parameters in CME-MEs, CME-sheaths, SIRs, and HSSs in the context of parameters that influence the jet generation. The mix of high cone angles and low Mach numbers are unfavorable SW conditions, hence, decreasing the production of jets in the magnetosheath. The condition within CME-MEs is similar to this condition, which gives context to the low detection number of jets in this structure as was reported by Koller et al. (2022). Without a foreshock that generates strongly non-linear structures near the subsolar region, the proposed jet generation mechanisms for the majority of jets is not applicable. Further investigation into the exact details is necessary to conclude, how the CME is disrupting the foreshock. Future case studies as well as simulations on the interaction of CMEs with the bow shock can complement our statistical work. The SW conditions that govern jet occurrence in SIRs, HSSs and unstructured SW are mostly governed by cone angle, density, and magnetic field. HSSs show the highest probability of jet occurrence in every SW parameter compared to all other SW structures, which is in agreement with the results by Koller et al. (2022). A next step is to analyze, whether the jets found during different structures have statistically distinctive differences in their properties. Cluster analysis using several SW parameters could give more insights in which combination of SW parameters can generate jets.

Data Availability Statement

We thank C. W. Carlson and J. P. McFadden for use of ESA data. We acknowledge the use of NASA/GSFC's Space Physics Data Facility's OMNI data and web services (https://omniweb.gsfc.nasa.gov/html/omni_min_data.html). THEMIS and OMNI data were accessed using the SPEDAS software (Angelopoulos et al., 2019). We provide the jet lists as well as the magnetosheath times at https://osf.io/s32yf/.

Acknowledgments
F.K., M.T., L.P., O.R., and F.P. gratefully acknowledge the Austrian Science Fund (FWF): P 33285-N for supporting this project. We acknowledge NASA contract NAS5-02099 and V. Angelopoulos for use of data from the THEMIS Mission. Specifically we thank K.H. Glassmeier, H.U. Auster and W. Baumjohann for the use of FGM data provided under the lead of the Technical University of Braunschweig and with financial support through the German Ministry for Economy and Technology and the German Center for Aviation and Space (DLR) under contract 50 OC 0302. F.P. acknowledges the support by the Deutsches Zentrum für Luft- und Raumfahrt under contract 50 OC 2201.

References

Anderson, B. J., Acuña, M. H., Korth, H., Slavin, J. A., Uno, H., Johnson, C. L., et al. (2010). The magnetic field of Mercury. *Space Science Reviews*, *152*(1–4), 307–339. https://doi.org/10.1007/s11214-009-9544-3

Angelopoulos, V. (2008). The THEMIS mission. *Space Science Reviews*, *141*(1–4), 5–34. https://doi.org/10.1007/s11214-008-9336-1

Angelopoulos, V., Cruce, P., Drozdov, A., Grimes, E. W., Hatzigeorgiu, N., King, D. A., et al. (2019). The space physics environment data analysis system (SPEDAS). *Space Science Reviews*, *215*(1), 9. https://doi.org/10.1007/s11214-018-0576-4

Archer, M. O., Hietala, H., Hartinger, M. D., Plaschke, F., & Angelopoulos, V. (2019). Direct observations of a surface Eigenmode of the dayside magnetopause. *Nature Communications*, *10*(1), 615. https://doi.org/10.1038/s41467-018-08134-5

Archer, M. O., & Horbury, T. S. (2013). Magnetosheath dynamic pressure enhancements: Occurrence and typical properties. *Annales Geophysicae*, *31*(2), 319–331. https://doi.org/10.5194/angeo-31-319-2013

Archer, M. O., Horbury, T. S., & Eastwood, J. P. (2012). Magnetosheath pressure pulses: Generation downstream of the bow shock from solar wind discontinuities. *Journal of Geophysical Research*, *117*(A5), A05228. https://doi.org/10.1029/2011JA017468

Auster, H. U., Glassmeier, K. H., Magnes, W., Aydogar, O., Baumjohann, W., Constantinescu, D., et al. (2008). The THEMIS fluxgate magnetometer. *Space Science Reviews*, *141*(1–4), 235–264. https://doi.org/10.1007/s11214-008-9365-9

Balogh, A., & Treumann, R. A. (2013). *Physics of collisionless shocks* (Vol. 12). Springer. https://doi.org/10.1007/978-1-4614-6099-2

Cane, H. V., & Richardson, I. G. (2003). Interplanetary coronal mass ejections in the near-Earth solar wind during 1996-2002. *Journal of Geophysical Research*, *108*(A4), 1156. https://doi.org/10.1029/2002JA009817

Eastwood, J. P., Lucek, E. A., Mazelle, C., Meziane, K., Narita, Y., Pickett, J., & Treumann, R. A. (2005). The foreshock. *Space Science Reviews*, *118*(1–4), 41–94. https://doi.org/10.1007/s11214-005-3824-3

Escoubet, C. P., Hwang, K. J., Toledo-Redondo, S., Turc, L., Haaland, S. E., Aunai, N., et al. (2020). Cluster and MMS simultaneous observations of magnetosheath high speed jets and their impact on the magnetopause. *Frontiers in Astronomy and Space Sciences*, *6*, 78. https://doi.org/10.3389/fspas.2019.00078

Geyer, P., Temmer, M., Guo, J., & Heinemann, S. G. (2021). Properties of stream interaction regions at Earth and Mars during the declining phase of SC 24. *Astronomy and Astrophysics*, *649*, A80. https://doi.org/10.1051/0004-6361/202040162

Grandin, M., Aikio, A. T., & Kozlovsky, A. (2019). Properties and geoeffectiveness of solar wind high-speed streams and stream interaction regions during solar cycles 23 and 24. *Journal of Geophysical Research: Space Physics*, *124*(6), 3871–3892. https://doi.org/10.1029/2018JA026396

Gutynska, O., Sibeck, D. G., & Omidi, N. (2015). Magnetosheath plasma structures and their relation to foreshock processes. *Journal of Geophysical Research: Space Physics*, *120*(9), 7687–7697. https://doi.org/10.1002/2014JA020880

Hietala, H., Laitinen, T. V., Andréeová, K., Vainio, R., Vaivads, A., Palmroth, M., et al. (2009). Supermagnetosonic jets behind a collisionless quasiparallel shock. *Physical Review Letters*, *103*(24), 245001. https://doi.org/10.1103/PhysRevLett.103.245001

Hietala, H., Partamies, N., Laitinen, T. V., Clausen, L. B. N., Facskó, G., Vaivads, A., et al. (2012). Supermagnetosonic subsolar magnetosheath jets and their effects: From the solar wind to the ionospheric convection. *Annales Geophysicae*, *30*(1), 33–48. https://doi.org/10.5194/angeo-30-33-2012

Hietala, H., Phan, T. D., Angelopoulos, V., Oieroset, M., Archer, M. O., Karlsson, T., & Plaschke, F. (2018). In situ observations of a magnetosheath high-speed jet triggering magnetopause reconnection. *Geophysics Research Letters*, *45*(4), 1732–1740. https://doi.org/10.1002/2017GL076525

Hietala, H., & Plaschke, F. (2013). On the generation of magnetosheath high−speed jets by bow shock ripples. *Journal of Geophysical Research: Space Physics*, *118*(11), 7237–7245. https://doi.org/10.1002/2013JA019172

Jian, L., Russell, C. T., & Luhmann, J. G. (2011). Comparing solar minimum 23/24 with historical solar wind records at 1 AU. *Solar Physics*, *274*(1–2), 321–344. https://doi.org/10.1007/s11207-011-9737-2

Jian, L., Russell, C. T., Luhmann, J. G., & Skoug, R. M. (2006). Properties of stream interactions at one AU during 1995 – 2004. *Solar Physics*, *239*(1–2), 337–392. https://doi.org/10.1007/s11207-006-0132-3

Kajdič, P., Raptis, S., Blanco-Cano, X., & Karlsson, T. (2021). Causes of jets in the quasi-perpendicular magnetosheath. *Geophysical Research Letters*, *48*(13), e93173. https://doi.org/10.1029/2021GL093173

Karlsson, T., Kullen, A., Liljeblad, E., Brenning, N., Nilsson, H., Gunell, H., & Hamrin, M. (2015). On the origin of magnetosheath plasmoids and their relation to magnetosheath jets. *Journal of Geophysical Research: Space Physics*, *120*(9), 7390–7403. https://doi.org/10.1002/2015JA021487

Karlsson, T., Liljeblad, E., Kullen, A., Raines, J. M., Slavin, J. A., & Sundberg, T. (2016). Isolated magnetic field structures in Mercury's magnetosheath as possible analogues for terrestrial magnetosheath plasmoids and jets. *Planetary and Space Science*, *129*, 61–73. https://doi.org/10.1016/j.pss.2016.06.002

Kilpua, E., Koskinen, H. E. J., & Pulkkinen, T. I. (2017). Coronal mass ejections and their sheath regions in interplanetary space. *Living Reviews in Solar Physics*, *14*(1), 5. https://doi.org/10.1007/s41116-017-0009-6

King, J. H., & Papitashvili, N. E. (2005). Solar wind spatial scales in and comparisons of hourly wind and ACE plasma and magnetic field data. *Journal of Geophysical Research*, *110*(A2), A02104. https://doi.org/10.1029/2004JA010649

Koller, F., Plaschke, F., Temmer, M., Preisser, L., Roberts, O. W., & Vörös, Z. (2023). *Themis magnetosheath and jet intervals 2008-2021*. OSF. Retrieved from osf.io/s32yf

Koller, F., Temmer, M., Preisser, L., Plaschke, F., Geyer, P., Jian, L. K., et al. (2022). Magnetosheath jet occurrence rate in relation to CMEs and SIRs. *Journal of Geophysical Research: Space Physics*, *127*(4), e2021JA030124. https://doi.org/10.1029/2021JA030124

LaMoury, A. T., Hietala, H., Plaschke, F., Vuorinen, L., & Eastwood, J. P. (2021). Solar wind control of magnetosheath jet formation and propagation to the magnetopause. *Journal of Geophysical Research: Space Physics*, *126*(9), e2021JA029592. https://doi.org/10.1029/2021JA029592

Lavraud, B., & Borovsky, J. E. (2008). Altered solar wind-magnetosphere interaction at low Mach numbers: Coronal mass ejections. *Journal of Geophysical Research*, *113*(A9), A00B08. https://doi.org/10.1029/2008JA013192

McFadden, J. P., Carlson, C. W., Larson, D., Ludlam, M., Abiad, R., Elliott, B., et al. (2008). The THEMIS ESA plasma instrument and in-flight calibration. *Space Science Reviews*, *141*(1–4), 277–302. https://doi.org/10.1007/s11214-008-9440-2

Milillo, A., Fujimoto, M., Murakami, G., Benkhoff, J., Zender, J., Aizawa, S., et al. (2020). Investigating Mercury's environment with the two-spacecraft BepiColombo mission. *Space Science Reviews*, *216*(5), 93. https://doi.org/10.1007/s11214-020-00712-8

Němeček, Z., Šafránková, J., Přech, L., Sibeck, D. G., Kokubun, S., & Mukai, T. (1998). Transient flux enhancements in the magnetosheath. *Geophysics Research Letters*, *25*(8), 1273–1276. https://doi.org/10.1029/98GL50873

Norenius, L., Hamrin, M., Goncharov, O., Gunell, H., Opgenoorth, H., Pitkänen, T., et al. (2021). Ground-based magnetometer response to impacting magnetosheath jets. *Journal of Geophysical Research: Space Physics*, *126*(8), e29115. https://doi.org/10.1029/2021JA029115

Nykyri, K., Bengtson, M., Angelopoulos, V., Nishimura, Y., & Wing, S. (2019). Can enhanced flux loading by high-speed jets lead to a substorm? Multipoint detection of the christmas day substorm onset at 08:17 UT, 2015. *Journal of Geophysical Research: Space Physics*, *124*(6), 4314–4340. https://doi.org/10.1029/2018JA026357

Palmroth, M., Ganse, U., Pfau-Kempf, Y., Battarbee, M., Turc, L., Brito, T., et al. (2018a). Vlasov methods in space physics and astrophysics. *Living Reviews in Computational Astrophysics*, *4*(1), 1. https://doi.org/10.1007/s41115-018-0003-2

Palmroth, M., Hietala, H., Plaschke, F., Archer, M., Karlsson, T., Blanco-Cano, X., et al. (2018b). Magnetosheath jet properties and evolution as determined by a global hybrid-Vlasov simulation. *Annales Geophysicae*, *36*(5), 1171–1182. https://doi.org/10.5194/angeo-36-1171-2018

Plaschke, F., Hietala, H., & Angelopoulos, V. (2013). Anti-sunward high-speed jets in the subsolar magnetosheath. *Annales Geophysicae*, *31*(10), 1877–1889. https://doi.org/10.5194/angeo-31-1877-2013

Plaschke, F., Hietala, H., Angelopoulos, V., & Nakamura, R. (2016). Geoeffective jets impacting the magnetopause are very common. *Journal of Geophysical Research: Space Physics*, *121*(4), 3240–3253. https://doi.org/10.1002/2016JA022534

Plaschke, F., Hietala, H., Archer, M., Blanco-Cano, X., Kajdič, P., Karlsson, T., et al. (2018). Jets downstream of collisionless shocks. *Space Science Reviews*, *214*(5), 81. https://doi.org/10.1007/s11214-018-0516-3

Plaschke, F., Hietala, H., & Vörös, Z. (2020). Scale sizes of magnetosheath jets. *Journal of Geophysical Research: Space Physics*, *125*(9), e27962. https://doi.org/10.1029/2020JA027962

Preisser, L., Blanco-Cano, X., Kajdič, P., Burgess, D., & Trotta, D. (2020). Magnetosheath jets and plasmoids: Characteristics and formation mechanisms from hybrid simulations. *The Astrophysical Journal Letters*, *900*(1), L6. https://doi.org/10.3847/2041-8213/abad2b

Raptis, S., Karlsson, T., Plaschke, F., Kullen, A., & Lindqvist, P.-A. (2020). Classifying magnetosheath jets using MMS: Statistical properties. *Journal of Geophysical Research: Space Physics*, *125*(11), e27754. https://doi.org/10.1029/2019JA027754

Raptis, S., Karlsson, T., Vaivads, A., Lindberg, M., Johlander, A., & Trollvik, H. (2022). On magnetosheath jet kinetic structure and plasma properties. *Geophysical Research Letters*, *49*(21), e2022GL100678. https://doi.org/10.1029/2022GL100678

Raptis, S., Karlsson, T., Vaivads, A., Pollock, C., Plaschke, F., Johlander, A., et al. (2022). Downstream high-speed plasma jet generation as a direct consequence of shock reformation. *Nature Communications*, *13*(1), 598. https://doi.org/10.1038/s41467-022-28110-4

Richardson, I. G., & Cane, H. V. (2010). Near-Earth interplanetary coronal mass ejections during solar cycle 23 (1996 – 2009): Catalog and summary of properties. *Solar Physics*, *264*(1), 189–237. https://doi.org/10.1007/s11207-010-9568-6

Schwartz, S. J., & Burgess, D. (1991). Quasi-parallel shocks: A patchwork of three-dimensional structures. *Geophysical Research Letters*, *18*(3), 373–376. https://doi.org/10.1029/91GL00138

Stone, E. C., Frandsen, A. M., Mewaldt, R. A., Christian, E. R., Margolies, D., Ormes, J. F., & Snow, F. (1998). The advanced composition explorer. *Space Science Reviews*, *86*(1/4), 1–22. https://doi.org/10.1023/A:1005082526237

Sundberg, T., Boardsen, S. A., Burgess, D., & Slavin, J. A. (2015). Coherent wave activity in Mercury's magnetosheath. *Journal of Geophysical Research: Space Physics*, *120*(9), 7342–7356. https://doi.org/10.1002/2015JA021499

Suni, J., Palmroth, M., Turc, L., Battarbee, M., Johlander, A., Tarvus, V., et al. (2021). Connection between foreshock structures and the generation of magnetosheath jets: Vlasiator results. *Geophysical Research Letters*, *48*(20), e95655. https://doi.org/10.1029/2021GL095655

Temmer, M. (2021). Space weather: The solar perspective. *Living Reviews in Solar Physics*, *18*(1), 4. https://doi.org/10.1007/s41116-021-00030-3

Temmer, M., & Bothmer, V. (2022). Characteristics and evolution of sheath and leading edge structures of interplanetary coronal mass ejections in the inner heliosphere based on Helios and Parker Solar Probe observations. *Astronomy and Astrophysics*, *665*, A70. https://doi.org/10.1051/0004-6361/202243291

Tinoco-Arenas, A., Kajdič, P., Preisser, L., Blanco-Cano, X., Trotta, D., & Burgess, D. (2022). Parametric study of magnetosheath jets in 2D local hybrid simulations. *Frontiers in Astronomy and Space Sciences*, *9*, 5. https://doi.org/10.3389/fspas.2022.793195

Turc, L., Escoubet, C. P., Fontaine, D., Kilpua, E. K. J., & Enestam, S. (2016). Cone angle control of the interaction of magnetic clouds with the Earth's bow shock. *Geophysical Research Letters*, *43*(10), 4781–4789. https://doi.org/10.1002/2016GL068818

Turc, L., Ganse, U., Pfau-Kempf, Y., Hoilijoki, S., Battarbee, M., Juusola, L., et al. (2018). Foreshock properties at typical and enhanced interplanetary magnetic field strengths: Results from hybrid-Vlasov simulations. *Journal of Geophysical Research: Space Physics*, *123*(7), 5476–5493. https://doi.org/10.1029/2018JA025466

Turner, D. L., Liu, T. Z., Wilson, L. B., Cohen, I. J., Gershman, D. G., Fennell, J. F., et al. (2020). Microscopic, multipoint characterization of foreshock bubbles with magnetospheric multiscale (MMS). *Journal of Geophysical Research: Space Physics*, *125*(7), e27707. https://doi.org/10.1029/2019JA027707

Vu, A., Liu, T. Z., Zhang, H., & Pollock, C. (2022). Statistical study of foreshock bubbles, hot flow anomalies, and spontaneous hot flow anomalies and their substructures observed by MMS. *Journal of Geophysical Research: Space Physics*, *127*(2), e2021JA030029. https://doi.org/10.1029/2021JA030029

Vuorinen, L., Hietala, H., & Plaschke, F. (2019). Jets in the magnetosheath: IMF control of where they occur. *Annales Geophysicae*, *37*(4), 689–697. https://doi.org/10.5194/angeo-37-689-2019

Yermolaev, Y. I., Lodkina, I. G., Khokhlachev, A. A., Yermolaev, M. Y., Riazantseva, M. O., Rakhmanova, L. S., et al. (2021). Drop of solar wind at the end of the 20th century. *Journal of Geophysical Research: Space Physics*, *126*(9), e29618. https://doi.org/10.1029/2021JA029618

Paper 3

5

The Effect of Fast Solar Wind on Ion Distribution Downstream of Earth's Bow Shock

Florian Koller[1], Savvas Raptis[2], Manuela Temmer[1] , and Tomas Karlsson[3]

[1] Institute of Physics, University of Graz, Graz, Austria
[2] The Johns Hopkins Applied Physics Laboratory, Laurel, MD, USA
[3] KTH, Royal Institute of Technology, Division of Space and Plasma Physics, Stockholm, Sweden

The following article is published in The Astrophysical Journal Letters, Volume 964, Issue 1, article id. L5, 9pp. (2024). The pdf document is available in the online version of this journal and embedded one-to-one in this thesis. My own contribution to this work was 70%.

The Astrophysical Journal Letters, 964:L5 (9pp), 2024 March 20 https://doi.org/10.3847/2041-8213/ad2ddf

The Effect of Fast Solar Wind on Ion Distribution Downstream of Earth's Bow Shock

Florian Koller[1], Savvas Raptis[2], Manuela Temmer[1], and Tomas Karlsson[3]
[1] Institute of Physics, University of Graz, Universitätsplatz 5, 8010 Graz, Austria; florian.koller@uni-graz.at
[2] The Johns Hopkins Applied Physics Laboratory, Laurel, MD, USA
[3] KTH, Royal Institute of Technology, Division of Space and Plasma Physics, Stockholm, Sweden
Received 2024 January 30; revised 2024 February 26; accepted 2024 February 27; published 2024 March 18

Abstract

The solar wind gets thermalized and compressed when crossing a planetary bow shock, forming the magnetosheath. The angle between the upstream magnetic field and the shock normal vector separates the quasi-parallel from the quasi-perpendicular magnetosheath, significantly influencing the physical conditions in these regions. A reliable classification between both magnetosheath regions is of utmost importance since different phenomena and physical processes take place on each. The complexity of this classification is increased due to the origin and variability of the solar wind. Using measurements from the Time History of Events and Macroscale Interactions during Substorms mission and OMNI data between 2008 and 2023, we demonstrate the importance of magnetosheath classification across various solar wind plasma origins. We focus on investigating the ion energy fluxes in the high-energy range for each solar wind type, which typically serves as an indicator for foreshock activity and thus separating the quasi-parallel from quasi-perpendicular magnetosheath. Dividing the data set into different regimes reveals that fast solar wind plasma originating from coronal holes causes exceptionally high-energy ion fluxes even in the quasi-perpendicular environment. This stands in stark contrast to all other solar wind types, highlighting that magnetosheath classification is inherently biased if not all types of solar wind are considered in the classification. Combining knowledge of solar wind origins and structures with shock and magnetosheath research thus contributes to an improved magnetosheath characterization. This is particularly valuable in big-data machine-learning applications within heliophysics, which requires clean and verified data sets for optimal performance.

Unified Astronomy Thesaurus concepts: Planetary bow shocks (1246); Space plasmas (1544); Heliosphere (711); Fast solar wind (1872); Solar coronal holes (1484); Solar wind (1534); Plasma astrophysics (1261); Plasma physics (2089); Solar-terrestrial interactions (1473); Interplanetary medium (825); Shocks (2086); Space weather (2037)

1. Introduction

The solar wind plasma gets shocked as it encounters the magnetic field of the Earth, forming the bow shock and the downstream magnetosheath region. The interplanetary magnetic field (IMF), which is convected with the solar wind, determines the behavior of the plasma surrounding the shock. The IMF angle at the shock surface θ_{Bn} divides the shock into a quasi-parallel ($\theta_{Bn} < 45°$) and quasi-perpendicular ($\theta_{Bn} > 45°$) region. The behavior of the magnetosheath exhibits notable distinctions behind the quasi-parallel and quasi-perpendicular shock. The quasi-parallel plasma region is strongly affected by the foreshock upstream of the shock, which is characterized by a mixture of incoming and backstreaming plasma and induces waves, decelerates solar wind, and forms nonlinear structures (Eastwood et al. 2005). Due to the presence of the foreshock, the downstream region displays a heightened energy flux as well as increased magnetic field variations. The quasi-perpendicular shock shows an increase in temperature anisotropy while lacking high ion energy fluxes. The subsequent impact on Earth's magnetic field and geoeffectiveness is fundamentally different in both regions. Figure 1 shows an overview of the dayside terrestrial magnetosheath.

Typical in situ classification of the magnetosheath relies on ion plasma moments. By measuring the energy flux one can infer the spacecraft's position in either the quasi-parallel or quasi-perpendicular magnetosheath (Raptis et al. 2020b). Karlsson et al. (2021) provide a framework for classifying magnetosheath based on Cluster (Escoubet et al. 1997) spacecraft observations using nine sample times between 2003 and 2009. They used cases with one spacecraft in the upstream solar wind and one in the downstream magnetosheath to confirm the angle Θ_{Bn}, restricting all measurements close to the shock. They used the integrated energy flux of the highest four energy bins of the Cluster Ion Spectrometer (CIS) Hot Ion analyzer (HIA) (Reme et al. 1997). Based on this data set, they defined thresholds to differentiate between quasi-parallel and quasi-perpendicular magnetosheath. They also differentiated the magnetosheath based on the magnetic field component standard deviation and ion temperature anisotropy.

While in situ properties can provide a classification as mentioned above, it should be noted that the upstream solar wind, which is responsible for the sheath formation, can also be classified into different types based on its origin on the Sun. The magnetosheath classification efforts discussed above have not taken different solar wind sources into account, which can significantly impact the results as we will show throughout this work. We follow the classification by Xu & Borovsky (2015) of four solar wind classes named after their origin: ejecta, coronal hole, sector reversal, and streamer belt. These categories can be associated to solar wind structures detected at Earth. Coronal mass ejections can be linked to ejecta, which usually describes low plasma beta, low Alfvén Mach number, high magnetic field strength with little fluctuation, and a non–

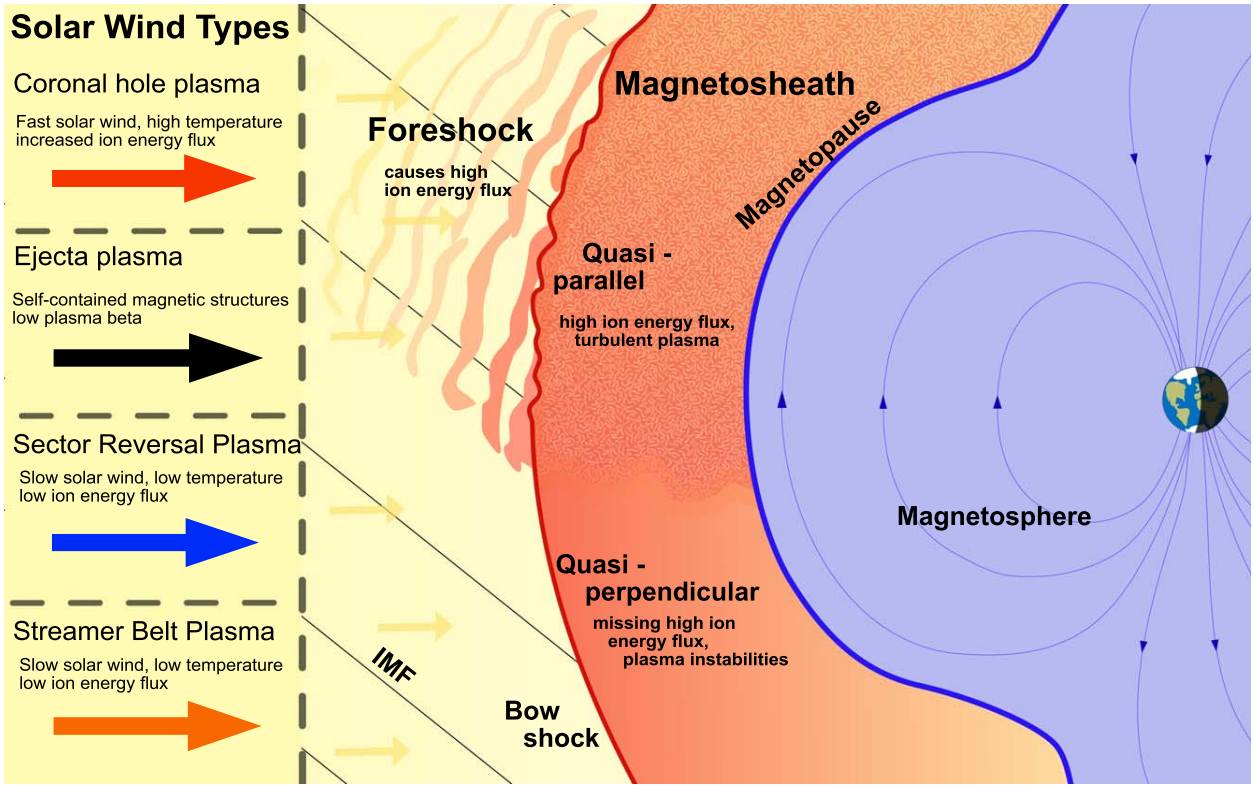

Figure 1. Schematic of the dayside magnetosphere and magnetosheath of the Earth. The system is affected by different incoming solar wind types (left side).

Parker spiral IMF angle. High-speed streams emanate from coronal holes (open magnetic field lines in the solar corona) and generate stream interaction regions when interacting with slow solar wind. This plasma is characterized by its high velocity, high temperature, and a low O^{7+}/O^{6+} ratio as well as an IMF orientation following the Parker spiral. The slow solar wind corresponds mainly to sector reversal or streamer belt plasma. Sector reversal plasma is associated with plasma coming from the top of helmet streamers (cusp-like magnetic loops in the solar corona) and has very low velocity, a high O^{7+}/O^{6+} ratio, high Alfvén Mach number, little fluctuations, and a non–Parker spiral IMF angle. Streamer belt plasma is connected to regions between coronal holes and helmet streamers or loop arcades between coronal holes of same polarities (Xu & Borovsky 2015) with low velocity, intermediate Alfvén velocity, intermediate Alfvén Mach number, and the IMF angle following the Parker spiral. The occurrence of each type of solar wind structure changes significantly throughout a solar cycle (e.g., Temmer 2021).

A reliable categorization of the magnetosheath environment holds significant importance for related investigations. The quasi-parallel magnetosheath frequently exhibits dynamic pressure enhancements (so-called "jets"; Plaschke et al. 2018). Studies analyzed the connection between the occurrence of jets and upstream solar wind conditions (Vuorinen et al. 2019; Raptis et al. 2020b; LaMoury et al. 2021), solar wind structures (Koller et al. 2022, 2023), and long-term influence by the solar cycle (Vuorinen et al. 2023). Sorting the plasma environment into quasi-parallel and quasi-perpendicular is crucial to analyze jet generation, evolution, and properties (e.g., Raptis et al. 2020a, 2020b). Upstream foreshock mesoscale transients present in the quasi-parallel magnetosheath can also strongly affect Earth's environment (Zhang et al. 2022a). The quasi-perpendicular magnetosheath is prone to plasma mirror mode or ion cyclotron instabilities (Soucek et al. 2015) while the presence of current sheets and turbulence is also different between each region (Yordanova et al. 2020; Gurchumelia et al. 2022). Processes connected to the radial distance are influenced as well, i.e., magnetosheath plasma can charge exchange with neutral hydrogen of Earth's outer exosphere close to the magnetopause (Fahr et al. 2018). This is largely controlled by solar wind parameter (Sokółet al. 2023) and shows dependencies on IMF orientation as well (Starkey et al. 2022).

This study demonstrates that different solar wind classes have a statistical influence on magnetosheath classification, primarily due to differences in high ion energy fluxes among solar wind types. Fast solar wind correlates with high ion energies, making the downstream plasma classification challenging. We investigate these effects in order to initiate improvements for future magnetosheath separation algorithms. This work utilizes data from Time History of Events and Macroscale Interactions during Substorms (THEMIS; Angelopoulos 2008), which spans more than a full solar cycle. The abundance of THEMIS measurements (year 2008–now) enables a statistically robust connection between specific solar wind types and magnetosheath plasma, which is now made possible by the growing data set of subsolar magnetosheath measurements.

2. Data

Our study utilizes OMNI data (King & Papitashvili 2005) to classify the solar wind and THEMIS data from the terrestrial magnetosheath covering the period from the beginning of 2008 to the end of 2022. We specifically use the THEMIS

Electrostatic Analyzer (ESA; McFadden et al. 2008) and Fluxgate Magnetometer (Auster et al. 2008) instruments in our analysis. THEMIS spacecraft are required to be within a 30° cone around the Sun–Earth line to restrict to subsolar dayside regions. Intervals of magnetosheath times were automatically detected using the method by Plaschke et al. (2013): the plasma density is required to be 2 times denser than the OMNI solar wind density and the 10 keV ion energy flux needs to be lower than the 1 keV ion energy flux. Only magnetosheath intervals $\geqslant$30 minutes were considered. As the study is based on broad statistics, we interpolated all measurements used in the statistical analysis to 1 minute resolution. In the following analysis, we connect the magnetosheath measurements to the associated solar wind class defined by OMNI measurements.

The highest ESA ion energy flux bins were used, similar to Karlsson et al. (2021). There are in total four energy bins with values around 10 keV or greater, with the lowest starting at 8.1 keV. The uppermost energy flux that provides valid measurements in ESA usually shows a maximum energy level of up to 24.4 keV. The highest two to four bins were integrated as follows:

$$F_{\mathrm{high},N} = \sum_{i=1}^{N} F_i^* \Delta E_i, \quad (1)$$

with F_i being the differential energy flux at channel i (with $i = 1$ being the highest channel) and ΔE_i being the width of the energy bin i. The energy bin width follows the width of logarithmically spaced energy flux steps. Thus, $F_{\mathrm{high},1}$ denotes the flux of the highest bin, $F_{\mathrm{high},2}$ the integrated flux of the two highest bins, and so on. The Cluster CIS-HIA energy fluxes used in Karlsson et al. (2021) have a higher upper range in the ion energy spectrum. Therefore, a one-to-one comparison of the integrated flux measure using the highest four bins would not quantitatively yield similar results between both missions. The highest three bins from THEMIS ESA have similar energy ranges and widths as the highest two to four energy bins in Cluster CIS-HIA, which is the largest overlap of energy range in this work and the measure used in Karlsson et al. (2021).

Utilizing the classification scheme established by Xu & Borovsky (2015) with a temporal resolution of 1 hr, we apply the methodology proposed by Camporeale et al. (2017) for solar wind classification through machine learning. The solar wind is categorized into four distinct origins: ejecta, coronal hole, sector reversal, and streamer belt. By using the same training set and a Gaussian process supervised learning model as Camporeale et al. (2017), we classified the 1 hr OMNI data set up to 2023. This method provides a probability per hour for each of the four classes instead of unambiguously putting events into one category. This allows the usage of a confidence level for selecting classes as described below. It should be noted that our statistical results were cross-validated for the periods obtained up to 2017 in the original paper with full agreement. This suggests that the rest of the classification period (2017–2023) follows the expected trends discussed in Xu & Borovsky (2015).

To ensure statistical robustness, we require that the classification probability for a single solar wind class exceeds and maintains 0.4 (40%) for a consecutive duration of at least 3 hr. We exclude the first and last hour of each solar wind class instance to avoid significant mixing of different solar wind classes. OMNI measurements are time-shifted by 2.5 minutes with respect to THEMIS measurements to statistically account for the delay of the plasma moving from the bow shock nose to the spacecraft further down in the sheath. This amounts to a total usable data set of 3144.2 hr (52.4 days) divided into classes as follows: 1480.6 hr of sector reversal plasma, 891.3 hr of streamer belt plasma, 610.3 hr of coronal hole plasma, and 161.9 hr of ejecta plasma.

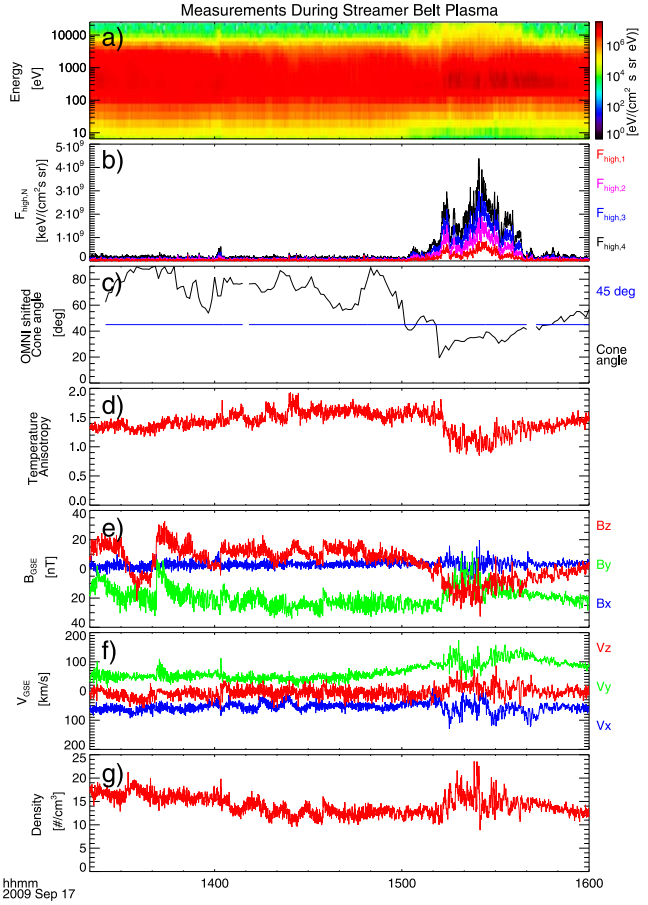

Figure 2. THEMIS A magnetosheath measurements during streamer belts origin plasma. The panels show (a) ion energy spectrum, (b) integrated top four bins of energy spectrum, (c) associated IMF cone angle, (d) temperature anisotropy, (e) magnetic field components, (f) ion velocity components, and (g) ion density.

3. Results

The presence of high-energy ions can be used as an indicator that the spacecraft is downstream of the quasi-parallel shock. Figure 2 shows roughly 3 hr of magnetosheath measurements by THEMIS during a time when the solar wind plasma originated from streamer belts. Panel (a) shows the ion energy spectrum with a clear change in the behavior around 15:30, showing an energy increase in the highest channels. Panel (b) shows the integrated flux of these top four energy bins as defined by Equation (1). The increase correlates with the decrease of the OMNI IMF cone angle (panel (c)), indicating a switch of quasi-perpendicular to quasi-parallel plasma and back associated with the change in IMF direction. Both cone angle and simple thresholds on $F_{\mathrm{high},N}$ could be effectively used to classify the magnetosheath in this event.

Figure 3 shows 4 hr of magnetosheath data during coronal hole plasma. The overall energy flux is increased: $F_{\mathrm{high},4}$ is

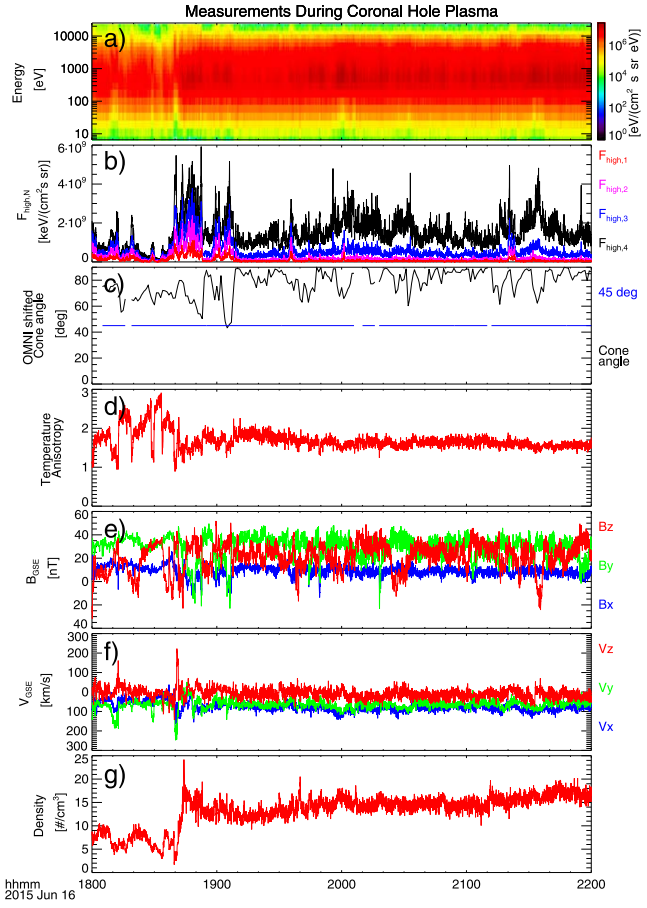

Figure 3. THEMIS A magnetosheath measurements during coronal hole origin plasma. The panels follow the same format as Figure 2.

heightened to a constant background level (black line in panel (b)). Quasi-parallel magnetosheath presence can be seen between 18:30 and 18:50, by the increase of ion flux in all higher-energy bins. This also coincides with decreasing cone angle values. However, the cone angle never falls below 45°, which makes its usage to classify the magnetosheath insufficient for this example. Using a threshold for $F_{\mathrm{high},3}$ or $F_{\mathrm{high},2}$ might work to classify the sheath, however, with little error margin compared to the clear increase visible in the streamer belt plasma example.

In order to separate the ion energy flux into high-energy regime (quasi-parallel) and low-energy regime (quasi-perpendicular), we analyze the statistical distribution of ion high-energy fluxes for each solar wind class. This corresponds to the total statistical distribution of the values shown in the examples of Figures 2(b) and 3(b). A double-peaked distribution is expected due to the difference in energy flux within the quasi-parallel and quasi-perpendicular region. Figure 4 depicts the high-energy histogram for solar wind classes for the top four integrated bins. Notably, the energy flux associated with coronal holes exceeds all other classes by a large margin in every panel. Sector reversal and streamer belt plasma show a double-peaked distribution in $F_{\mathrm{high},4}$, $F_{\mathrm{high},3}$, and less obvious in $F_{\mathrm{high},2}$. The broad distribution of coronal hole plasma in panel (a) peaks at values 2–7 times higher than the high-energy peak of other classes. The coronal hole plasma cannot be easily divided into subsections in any flux bins, only showing a slight indication of a double-peaked distribution in panels (b) and (c). Ejecta plasma shows a prolonged distribution at higher-energy fluxes instead of a peak in all panels, suggesting mostly quasi-perpendicular plasma. The overlap between the distributions of coronal hole plasma and the other classes is the largest in $F_{\mathrm{high},1}$ (panel (d)). However, other solar wind types do not show a clear distinction between high- and low-energy flux regime using $F_{\mathrm{high},1}$.

Lastly, we use cone angle characterization to explore the quasi-parallel and quasi-perpendicular plasma energy flux distributions for each solar wind type. For this purpose, we divide the $F_{\mathrm{high},3}$ distribution (Figure 4(b)) into high (>60°), intermediate ($30° < \Phi < 60°$), and low cone angle (<30°) regimes. Figure 5 shows the $F_{\mathrm{high},3}$ energy flux histograms for each solar wind class for the aforementioned cone angle regimes. Panel (a) displays the $F_{\mathrm{high},3}$ distribution under high cone angles, corresponding to low-energy quasi-perpendicular magnetosheath plasma. Panel (b) represents the cone angle histograms associated with the values in panel (a). Notably, the energy flux of quasi-perpendicular plasma in coronal holes is roughly 1 order of magnitude higher than in all other classes. Moving to the $F_{\mathrm{high},3}$ energy flux in intermediate cone angle regimes, we see a distinct bimodal distribution in ejecta, sector reversal, and streamer belt plasma. This indicates a mix of quasi-parallel and quasi-perpendicular magnetosheath plasma. A gray line at 0.2×10^9 keV cm^{-2} s^{-1} sr^{-1} is included to highlight the dip position between both peaks, serving as an approximate separator for quasi-parallel and quasi-perpendicular magnetosheath. There is no bimodal $F_{\mathrm{high},3}$ distribution visible in coronal hole plasma in intermediate cone angle regimes. Panel (e) shows the $F_{\mathrm{high},3}$ distribution at low cone angles (corresponding to panel (f)), which should statistically represent high-energy quasi-parallel magnetosheath. As expected, the $F_{\mathrm{high},3}$ distributions for sector reversal, streamer belt, and ejecta plasma have peaks at higher-energy fluxes. The small peaks at lower energies in sector reversal and streamer belt plasma likely represent a residual quasi-perpendicular plasma population due to the cone angle not correctly representing the subsolar magnetosheath. Coronal hole origin plasma distribution at low cone angles gradually increases and peaks at values roughly 3–7 times higher than other solar wind types. The broad $F_{\mathrm{high},3}$ coronal hole plasma distribution in all regimes indicates either a wide range of energy flux for quasi-parallel and quasi-perpendicular plasma or a high percentage of incorrect cone angle characterization. Using information from panels (a), (c), and (e), a separator line (red) for coronal hole plasma was inserted at 1.6×10^9 keV cm^{-2} s^{-1} sr^{-1}, approximately 8 times higher than the separator line for other classes. The gray separator line would categorize most instances of coronal hole plasma as quasi-parallel, independent of the cone angle.

4. Discussion and Conclusion

We demonstrated that magnetosheath plasma originating from coronal holes would be almost exclusively classified as quasi-parallel plasma when using an energy-flux-based threshold obtained on average solar wind conditions. Statistically, the average cone angle in coronal hole plasma is lower compared to other solar wind types (Borovsky et al. 2019; Koller et al. 2023), resulting in more times of quasi-parallel plasma in the dayside magnetosheath. Previous studies found more magnetosheath jets in solar wind high-speed streams (corresponding to coronal hole plasma), also indicating an increase in quasi-

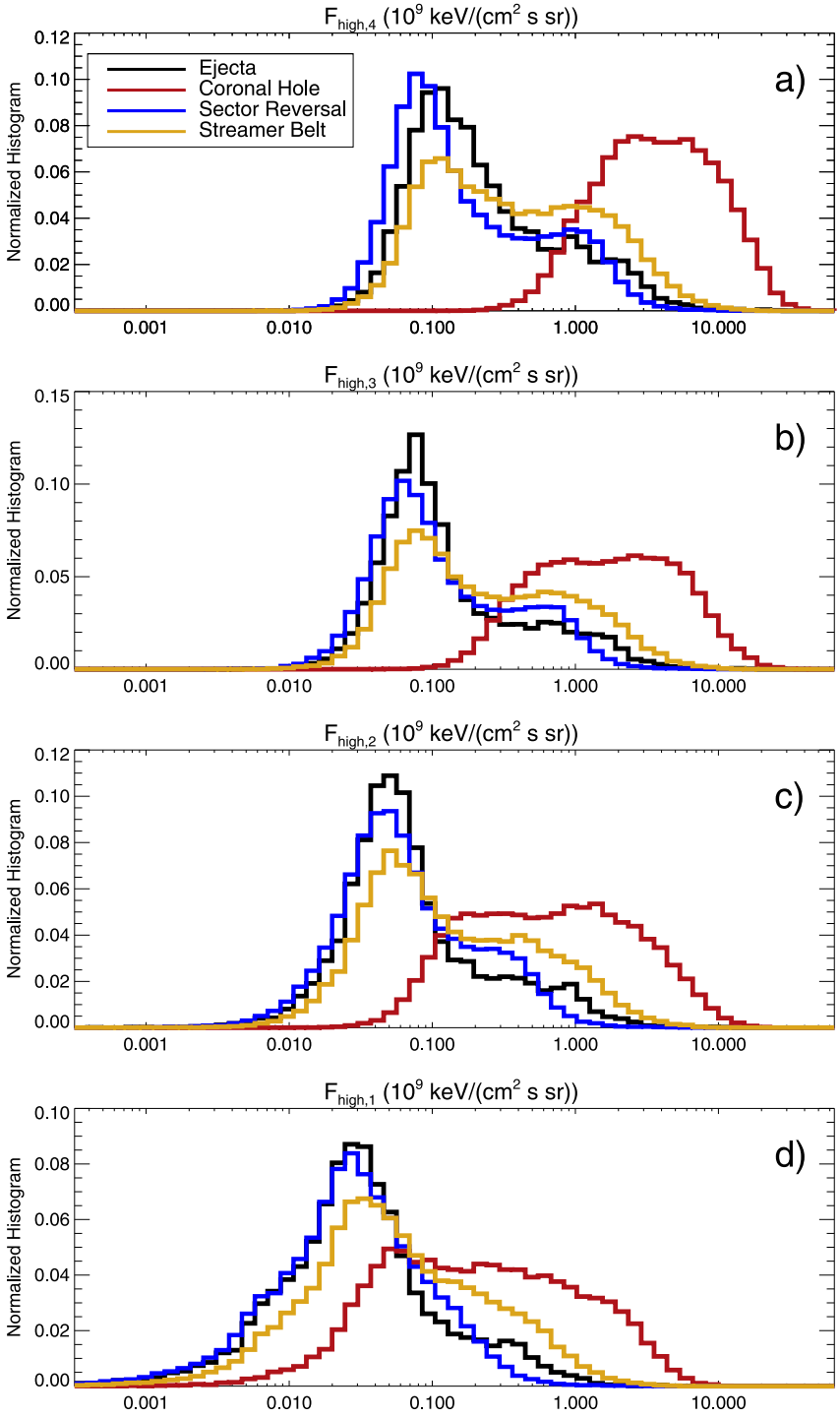

Figure 4. Normalized histograms of the highest four integrated energy flux bins given by Equation (1) for each solar wind type. Panel (a) corresponds to $F_{\mathrm{high},4}$, (b) to $F_{\mathrm{high},3}$, (c) to $F_{\mathrm{high},2}$, and (d) to $F_{\mathrm{high},1}$. The distribution of plasma originating in ejecta is given in black, coronal hole in red, sector reversal in blue, and streamer belt in orange.

parallel magnetosheath conditions (Koller et al. 2022, 2023). This could explain why classification biases might not have played an immediately visible impact in previous studies, as the increased time of quasi-parallel magnetosheath in coronal hole plasma has physical merit. However, it is unlikely that the magnetosheath environment in coronal hole plasma is in quasi-parallel condition all the time, as the cone angle distribution still peaks at values higher than 50° (Borovsky et al. 2019).

Our results indicate inherent problems when using the cone angle as a proxy for Θ_{Bn}. Even restricting the analysis to narrow angle regimes leaves residual populations of the opposite angle regime in most solar wind classes. There are several possible reasons for this mismatch. ACE and WIND spacecraft used to monitor upstream solar wind conditions are often far away from the Earth–Sun line (Borovsky 2018; Walsh et al. 2019). Solar wind structures smaller than this separation

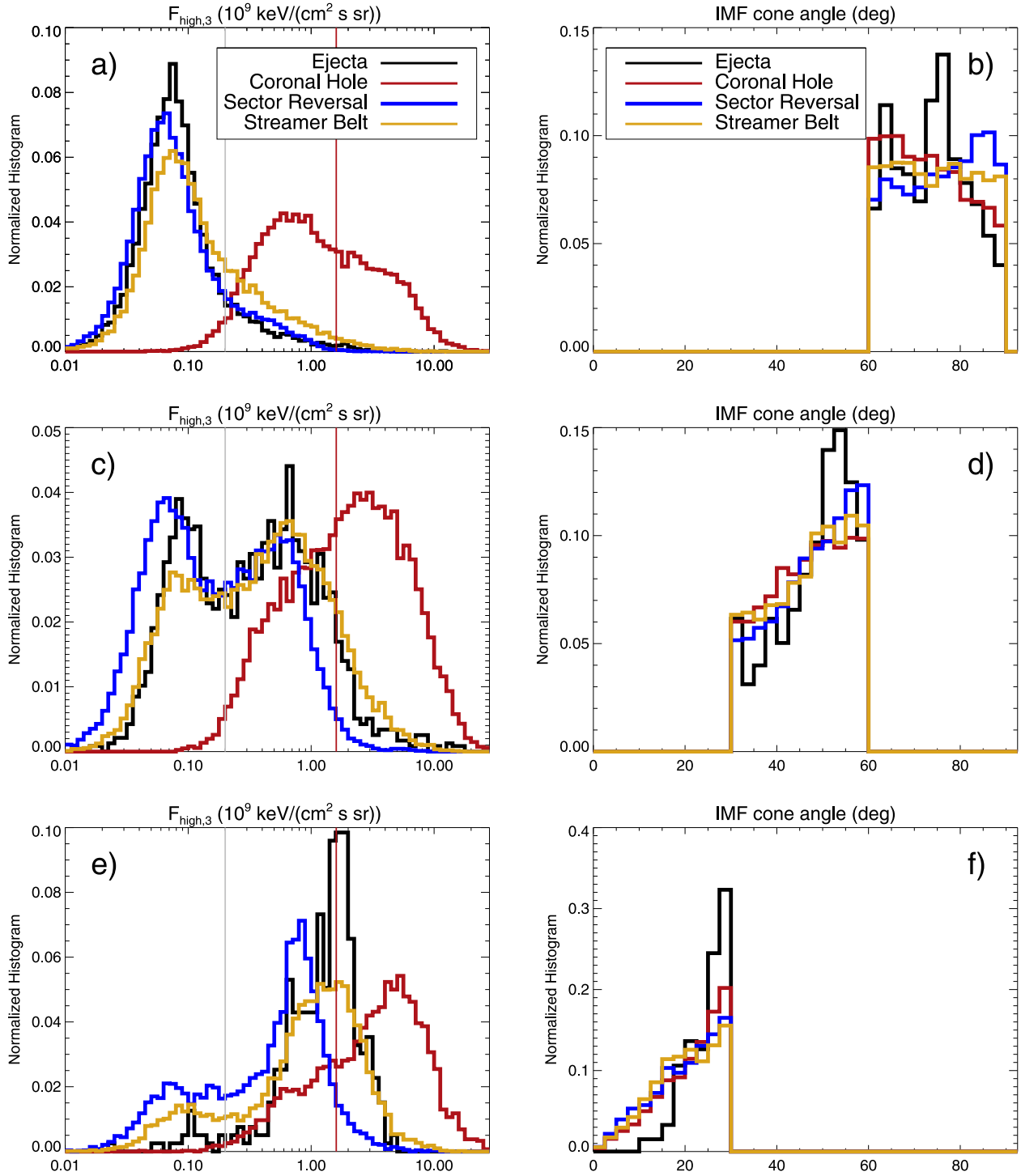

Figure 5. Normalized histograms of $F_{\mathrm{high,3}}$ in different IMF cone angle regimes for each type of solar wind. Panels (a), (b), and (c) show the distribution given in Figure 4(b) divided into high, medium, and low cone angle conditions. Panel (b) shows the high cone angle distribution corresponding to panel (a), intermediate cone angles in panel (d) correspond to panel (c), and low cone angles in panel (f) correspond to panel (e). The same color code of Figure 4 is used.

can result in incorrectly propagated plasma properties to the bow shock. This uncertainty is further increased in coronal hole plasma, as it tends to show stronger magnetic field and velocity fluctuations compared to other types (Borovsky et al. 2019). Low cone angles also induce uncertainty into the prediction of values at the magnetosheath (Walsh et al. 2019). Using bow shock models can help to approach the actual Θ_{Bn} value, while restricting to small solar zenith angles and positions close to the shock may also prove useful. Additionally, there might be a temporal offset due to the shifting of OMNI values from the bow shock nose to the actual spacecraft position in the magnetosheath. A way to mitigate propagation errors is to require stable IMF and magnetosheath conditions for the data set. However, this could rule out many events of explosive,

variable, and potentially geoeffective nature. Recent neural network efforts propagate L1 solar wind data to near-Earth space including uncertainty predictions, which could mitigate errors in future applications (e.g., O'Brien et al. 2023). Uncertainties due to mixing of different solar wind classes in coronal hole origin plasma is expected to be low, because this class has the highest likelihood of being correctly and unambiguously classified (Xu & Borovsky 2015; Camporeale et al. 2017). A different source of uncertainty is the reduction of energetic ions by processes in the magnetosheath, i.e., charge exchange with neutral, exospheric H-atoms close to the magnetopause (Fahr et al. 2018). Fuselier et al. (2020) reported that only 0.1% of the high-energy ions in the magnetosheath charge exchange; therefore we expect the statistical influence to be low.

Karlsson et al. (2021) also used the magnetic field standard deviation and plasma temperature anisotropy to differentiate quasi-parallel and quasi-perpendicular magnetosheath. These parameters should work reasonably well under ideal solar wind conditions close to the bow shock. However, they may also get affected by different solar wind classes and their properties. Strong magnetic field fluctuation often found in coronal hole plasma can persist even after crossing the bow shock: Figure 3 shows highly variable magnetic field components even within the supposedly quasi-perpendicular region. Temperature anisotropy is largely governed by the quasi-parallel and quasi-perpendicular shock. However, plasma expansion at the plasma depletion layer near the magnetopause can also cause large anisotropy values (Anderson & Fuselier 1993). As a result, the dependence of the temperature anisotropy on Θ_{Bn} is weaker close to the magnetopause (Soucek et al. 2015). Therefore, this parameter is also deemed to not be a reliable way to classify the whole magnetosheath.

Coronal hole origin plasma has a higher upper range in high-energy flux. While one can employ a threshold similar to Karlsson et al. (2021) at higher-energy levels, this might not hold for every event (see example cases in the Appendix). The usage of instruments with higher-energy levels might be beneficial for accurate classification. The THEMIS solid state telescope provides energetic ion fluxes $\geqslant$25 keV. Two instruments on the Magnetospheric Multiscale mission (Burch et al. 2016) provide higher ion energy levels: the Energetic Ion Spectrometer of the Energetic Particle Detector (Mauk et al. 2016, $\geqslant$20 keV), and the Fly's Eye Energetic Particle Spectrometer (Blake et al. 2016; $\geqslant$45 keV). Automatic classifications of plasma environments using machine-learning techniques (like the work by Olshevsky et al. 2021, for solar wind, ion foreshock, magnetosheath, and magnetosphere) might improve classifications. To adequately train neural networks, one needs to be aware that coronal hole plasma data with reliable labels have to be consciously included in the data. Crucially, the occurrence of specific solar wind origin plasma changes drastically over a solar cycle. Coronal hole origin plasma, for example, dominates the decline phase of the solar cycle in the ecliptical plane (e.g., Temmer 2021). Machine-learning approaches exclusively trained during a specific solar cycle phase thus can have intrinsic biases and may provide unreliable results during other solar cycle phases.

In summary, this study provides results of high timeliness for currently ongoing studies related to characterizing and labeling of the magnetosheath using both conventional algorithms and machine-learning techniques, which is crucial for detailed analysis of the plasma downstream of collisionless shocks. Not considering the effect of different solar wind types may result in erroneous classifications. Supervised machine-learning techniques with training sets that lack specific solar wind class input may be inherently biased and unable to properly model the output when upstream conditions change. With the upcoming peak of the solar cycle, it is vital to build awareness of these issues. The interdisciplinary nature of our work connects solar wind and magnetospheric physics communities while providing key results for addressing the coupling between solar wind and planetary magnetospheres. Finally, using different types of solar wind input can be useful for remote sensing of the magnetosheath as a consequence of charge exchange processes. Energetic neutral atoms (ENAs) form due to the interaction of magnetosheath with neutral hydrogen close to the magnetopause (Fahr et al. 2018). ENA flux is mostly governed by solar wind dynamic pressure due to the compression of the magnetopause (Sokółet al. 2023). The high-energy ENA flux range is directly governed by magnetosheath ion flux (Fuselier et al. 2020) and is increasingly correlated with solar wind velocity at higher energies (Sokół et al. 2023). Different solar wind types thus are expected to largely affect ENA production, especially fast solar wind of coronal hole origin. Soft X-ray emission due to charge exchange processes also arises near the Earth's magnetopause (Sibeck et al. 2018). This emission can be affected by different heavy ion abundances in ejecta (Zhang et al. 2022b; Zhou et al. 2023), slow and fast solar wind (Whittaker & Sembay 2016). Different local soft X-ray emission in the quasi-parallel and quasi-perpendicular sheath might arise due to different thermal velocities in both regions (discussed in Sibeck et al. 2018) or by jets indenting the magnetopause (Yang et al. 2024). Solar wind upstream context and magnetosheath classification is thus highly relevant for observations, e.g., by the upcoming SMILE mission (Branduardi-Raymont & Wang 2022).

Acknowledgments

F.K. and M.T. gratefully acknowledge the Austrian Science Fund (FWF): P 33285-N for supporting this project. S.R. acknowledges the support by Johns Hopkins University Applied Physics Laboratory independent R&D fund. S.R. acknowledges support from the NASA DRIVE Science Center for Geospace Storms (CGS) under award 80NSSC22M0163. We acknowledge NASA contract NAS5-02099 and V. Angelopoulos for use of data from the THEMIS Mission. Specifically, we thank K.H. Glassmeier, H.U. Auster, and W. Baumjohann for the use of FGM data provided under the lead of the Technical University of Braunschweig and with financial support through the German Ministry for Economy and Technology and the German Center for Aviation and Space (DLR) under contract 50 OC 0302.

Appendix
Magnetosheath Examples in Different Solar Wind Origin Plasma

Here we show example events of magnetosheath plasma connected to each of the four solar wind types used throughout this work. This puts the statistical results shown in Figures 4 and 5 into the context of actual in situ measurements. The focus of the following examples lies on quasi-perpendicular plasma, sometimes intersected with quasi-parallel plasma as well. The left panels of Figure 6 show magnetosheath measurements

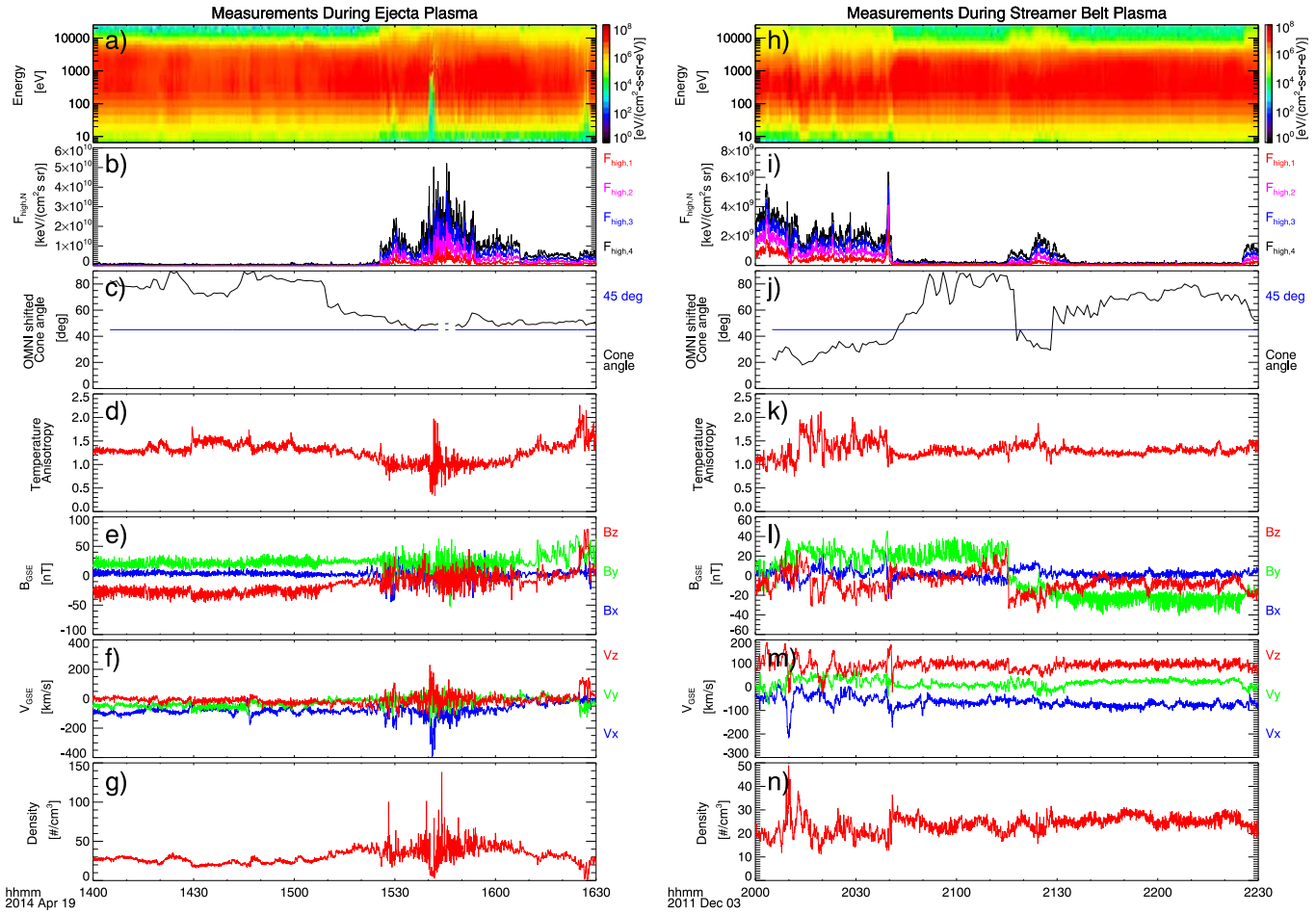

Figure 6. Example events of magnetosheath measurements by THEMIS A during ejecta (left) and streamer belt (right) plasma. The panels show ion energy spectrum (a), (h); integrated top four bins of the energy spectrum (b), (i); associated OMNI IMF cone angle (c), (j); temperature anisotropy (d), (k); magnetic field components (e), (l); ion velocity components (f), (m); and ion density (g), (n).

during plasma originating from solar ejecta. A clear interval of quasi-parallel plasma is visible starting at 15:27 UT, coinciding with an increase in $F_{\mathrm{high},N}$, a decrease in cone angle, temperature anisotropy around 1, and fluctuating magnetic field, velocity, and density values. There is a short time period of solar wind plasma visible at approximately 15:40 UT. The right panels of Figure 6 show magnetosheath measurements during streamer belt plasma. The cone angle and high-energy bins fluxes reliably indicate quasi-parallel magnetosheath plasma until 20:40 UT and between 21:15 and 21:35 UT. Unlike the example given in Figure 2, the temperature anisotropy and magnetic field fluctuations are not sufficient to detect the quasi-parallel sheath in this case.

Figure 7 (left panels) shows magnetosheath measurements at the start of a period of sector reversal plasma. Here, we see a time interval of quasi-parallel plasma around 01:20–02:20 UT, coinciding with a low IMF cone angle, decreased temperature anisotropy, and fluctuating magnetic field, velocity, and density parameters. The highest-energy bin, however, appears to almost show zero flux throughout the whole event. This is in stark contrast to the example event of coronal hole plasma in the magnetosheath (Figure 7, right panels). Here, the ion energy flux is increased to such high levels that the top integrated three and four energy bins show a constant enhancement throughout the given time interval, independent of quasi-parallel or quasi-perpendicular plasma. There are short periods of quasi-parallel magnetosheath, indicated by decreases in cone angle, temperature anisotropy values around 1, and fluctuating plasma parameters. This example also illustrates the difference between coronal hole events: the high ion energy flux is several times higher over the whole period compared to the coronal hole event in Figure 3. Specifically, the lowest values of $F_{\mathrm{high},3}$ in this event are larger than the maximum values of $F_{\mathrm{high},3}$ in Figure 3. Because of these differences, we see the broad statistical distribution of integrated ion flux for coronal hole origin plasma in Figures 4 and 5. Therefore, an energy flux threshold to classify the magnetosheath tailored to one specific event might not be valid for another one, even within the same solar wind type. On the other hand, the plasma environment in the event in Figure 7 could be reliably classified using temperature anisotropy, cone angle, and the standard deviation of the magnetic field. All of these classifications would not work for the coronal hole event in Figure 3, showcasing that the information on high ion energy flux is an essential tool for the in situ classification.

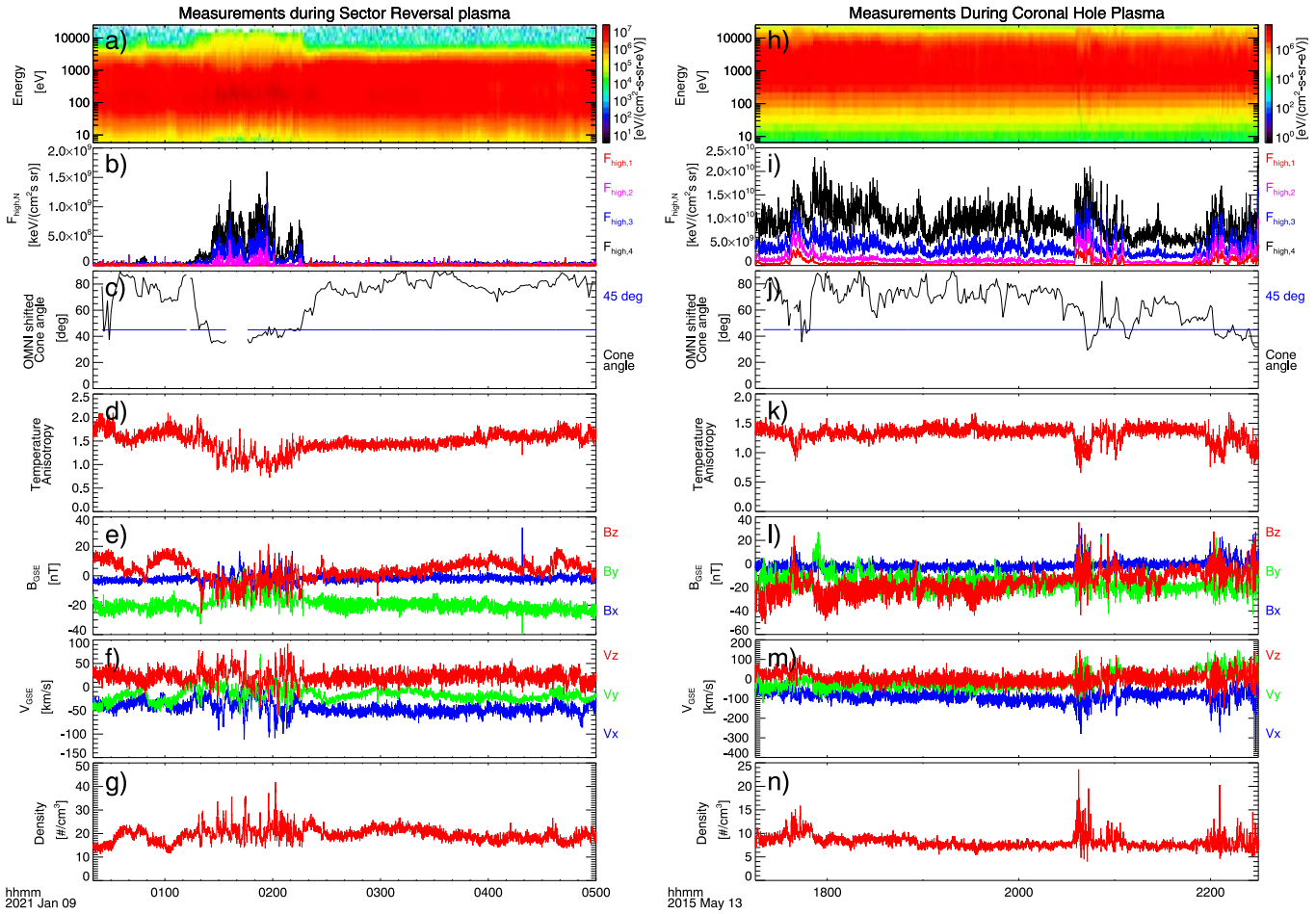

Figure 7. Example events of magnetosheath measurements by THEMIS A during sector reversal (left) and coronal hole (right) plasma. The panels follow the same structure as Figure 7.

ORCID iDs

Florian Koller https://orcid.org/0000-0002-8164-0004
Savvas Raptis https://orcid.org/0000-0002-4381-3197
Manuela Temmer https://orcid.org/0000-0003-4867-7558
Tomas Karlsson https://orcid.org/0000-0002-4546-5050

References

Anderson, B. J., & Fuselier, S. A. 1993, JGR, 98, 1461
Angelopoulos, V. 2008, SSRv, 141, 5
Auster, H. U., Glassmeier, K. H., Magnes, W., et al. 2008, SSRv, 141, 235
Blake, J., Mauk, B., Baker, D., et al. 2016, SSRv, 199, 309
Borovsky, J. E. 2018, JASTP, 177, 2
Borovsky, J. E., Denton, M. H., & Smith, C. W. 2019, JGRA, 124, 2406
Branduardi-Raymont, G., & Wang, C. 2022, in Handbook of X-ray and Gamma-ray Astrophysics, ed. C. Bambi & A. Santangelo (Singapore: Springer), 95
Burch, J. L., Moore, T. E., Torbert, R. B., & Giles, B. L. 2016, SSRv, 199, 5
Camporeale, E., Carè, A., & Borovsky, J. E. 2017, JGRA, 122, 10,910
Eastwood, J. P., Lucek, E. A., Mazelle, C., et al. 2005, SSRv, 118, 41
Escoubet, C. P., Schmidt, R., & Goldstein, M. L. 1997, SSRv, 79, 11
Fahr, H. J., Nass, U., Dutta-Roy, R., & Zoennchen, J. H. 2018, AnGeo, 36, 445
Fuselier, S. A., Dayeh, M. A., Galli, A., et al. 2020, GeoRL, 47, e89362
Gurchumelia, A., Sorriso-Valvo, L., Burgess, D., et al. 2022, FrP, 10, 903632
Karlsson, T., Raptis, S., Trollvik, H., & Nilsson, H. 2021, JGRA, 126, e2021JA029269
King, J. H., & Papitashvili, N. E. 2005, JGRA, 110, A02104
Koller, F., Plaschke, F., Temmer, M., et al. 2023, JGRA, 128, e2023JA031339
Koller, F., Temmer, M., Preisser, L., et al. 2022, JGRA, 127, e2021JA030124
LaMoury, A. T., Hietala, H., Plaschke, F., Vuorinen, L., & Eastwood, J. P. 2021, JGRA, 126, e2021JA029592
Mauk, B., Blake, J., Baker, D., et al. 2016, SSRv, 199, 471
McFadden, J. P., Carlson, C. W., Larson, D., et al. 2008, SSRv, 141, 277
O'Brien, C., Walsh, B. M., Zou, Y., et al. 2023, FrASS, 10, 1250779
Olshevsky, V., Khotyaintsev, Y. V., Lalti, A., et al. 2021, JGRA, 126, e2021JA029620
Plaschke, F., Hietala, H., & Angelopoulos, V. 2013, AnGeo, 31, 1877
Plaschke, F., Hietala, H., Archer, M., et al. 2018, SSRv, 214, 81
Raptis, S., Aminalragia-Giamini, S., Karlsson, T., & Lindberg, M. 2020a, FrASS, 7, 24
Raptis, S., Karlsson, T., Plaschke, F., Kullen, A., & Lindqvist, P. 2020b, JGRA, 125, e2019JA027754
Reme, H., Bosqued, J. M., Sauvaud, J. A., et al. 1997, SSRv, 79, 303
Sibeck, D. G., Allen, R., Aryan, H., et al. 2018, SSRv, 214, 79
Sokół, J. M., Starkey, M. J., Dayeh, M. A., et al. 2023, JGRA, 128, e2023JA031669
Soucek, J., Escoubet, C. P., & Grison, B. 2015, JGRA, 120, 2838
Starkey, M. J., Dayeh, M. A., Fuselier, S. A., et al. 2022, JGRA, 127, e2022JA030965
Temmer, M. 2021, LRSP, 18, 4
Vuorinen, L., Hietala, H., & Plaschke, F. 2019, AnGeo, 37, 689
Vuorinen, L., LaMoury, A. T., Hietala, H., & Koller, F. 2023, JGRA, 128, e2023JA031493
Walsh, B. M., Bhakyapaibul, T., & Zou, Y. 2019, JGRA, 124, 3291
Whittaker, I. C., & Sembay, S. 2016, GeoRL, 43, 7328
Xu, F., & Borovsky, J. E. 2015, JGRA, 120, 70
Yang, Z., Jarvinen, R., Guo, X., et al. 2024, E&PP, 8, 59
Yordanova, E., Vörös, Z., Raptis, S., & Karlsson, T. 2020, FrASS, 7, 2
Zhang, H., Zong, Q., Connor, H., et al. 2022a, SSRv, 218, 40
Zhang, Y., Sun, T., Wang, C., et al. 2022b, ApJL, 932, L1
Zhou, Y., Yamasaki, N. Y., Toriumi, S., & Mitsuda, K. 2023, JGRA, 128, e2023JA032069

6 Discussion, Conclusion, and Outlook

6.1 Literature Context

This work is one of the first large statistical analysis of in-situ magnetosheath plasma and magnetosheath effects with respect to specific solar wind structures. There have been so far only a few studies that explicitly connected measurement up-and downstream of Earth's bow shock with large-scale structures in the solar wind, in particular CMEs: Lavraud and Borovsky (2008) discussed, how CMEs and their low Mach numbers alters the magnetosheath and the solar wind-magnetosphere interaction. Turc et al. (2014b) showed four case studies on how the internal structure of magnetic clouds is altered after crossing into the magnetosheath. Turc et al. (2017) extended this work to a statistical magnetosheath analysis based on 82 magnetic clouds. A comparison of CME-induced low Mach number bow shock models was presented by Turc et al. (2013) and a simple 3D magnetosheath model in CME conditions was developed by Turc et al. (2014a). The cone angle of magnetic clouds hitting the Earth is analyzed in a statistical study by Turc et al. (2016), showing that the bow shock is primarily in quasi-perpendicular configuration during these events. The quasi-parallel configuration is only found for 6.3% of the time, which is matching with our results on CME parameters in Koller et al. (2023). The analysis on CMEs in the magnetosheath was also extended to simulations: Turc et al. (2015) analyzed the interaction of a bow shock with a magnetic cloud using 3D hybrid simulations. For the upstream region, Turc et al. (2019) presented for the first time the disruption of the foreshock wave field due to the impact of a magnetic cloud in Cluster data. Foreshock waves appeared to have shorter correlation lengths in magnetic clouds, which should affect the formation of jets based on current jet formation concepts (Section 2.4.2). Turc et al. (2019) confirmed their results using global numerical simulations as well. Some studies also analyzed the impact of interplanetary shocks on the dayside magnetosheath system: Hietala et al. (2011) and Hietala et al. (2012) analyzed particle acceleration at the interaction of the bow shock with a CME-driven shock using in-situ measurements and models. Ala-Lahti et al. (2021) investigated, how a CME-driven shock is transmitted into the Earth's magnetosheath in in-situ data. As far as we are aware, there were no statistical

results of CME-sheath plasma measurements in the terrestrial magnetosheath prior to our work.

Numerous publications don't mention the type of solar wind or structure and instead primarily focus on the solar wind plasma parameters in each case. Several studies on the magnetosheath and magnetosheath jets were conducted during SIRs and solar wind high-speed streams (as these have the ideal conditions for jet formation), including the first ever detection of a jet (Němeček et al., 1998; Archer et al., 2019; Escoubet et al., 2020; Hietala et al., 2009; Hietala et al., 2012; Hietala et al., 2018; Nykyri et al., 2019; Raptis et al., 2022b). However, the connection to solar wind structure occurrences was rarely, if at all, explicitly stated or investigated previous to our work.

As e.g. Lavraud and Borovsky (2008) and Turc et al. (2014b) point out, it is crucial to understand how large-scale solar wind events like CMEs are modified by the magnetosheath, because this altered plasma is the one that actually interacts with the Earth's magnetopause and causes geomagnetic effects. By only considering the impact of solar wind structures using upstream data, one misses critical physical processes that are happening between the solar wind and Earth's magnetic field. This is why our work is highly relevant to further understand the interaction chain between the solar wind and our plasma environment.

6.2 Methodology

In terms of methodology used in our work, we primarily focused on statistical spacecraft data analysis. A main data reduction challenge in all three publications was the detection of dayside magnetosheath intervals in THEMIS measurements. This was accomplished building on the algorithm by Plaschke et al. (2013) based on the density increase and the ratio of plasma energetic ion flux between 1 keV and 10 keV. This method is fairly robust as we found no instances of measurements that were wrongly classified as magnetosheath. All subsequent analysis holds true for the subsolar region only. The method results in a large database that covers a huge variety in solar wind upstream conditions. This made cross-checking of the data with solar wind event list possible.

Subsequent detection of jets was done in these magnetosheath subintervals. Criteria that used a 20 minute average thus were further restricted to long intervals only, while criteria based on the upstream solar wind can detect jets in shorter intervals as well. We switched the focus to jets on the local threshold criteria, because due to structured solar wind there where times where the magnetosheath was wrongfully

classified as a jet for up to ten minutes in upstream criteria due to a mismatch of OMNI and near-Earth data.

Paper 1 (Koller et al., 2022) utilized superposed epoch analysis to learn, how the jet occurrence changes for each type of structure in general. Paper 2 and 3 (Koller et al., 2023; Koller et al., 2024) focused on the parameter distributions in either solar wind or magnetosheath utilizing one- and two- dimensional histograms. All these works give general information on the behavior of the system. Individual events can vary greatly from each other, however, with a dataset that spans more than 13 years we expect robust results. Error estimations were done using bootstrapping.

6.3 Conclusion and Scientific Advancements for the Community

To summarize the work and overarching goal of the three publications presented in this thesis: We showed for the first time, how structured solar wind impacts the occurrence of dynamic pressure enhancements in the magnetosheath and how they change the ion energy distribution in the magnetosheath.

The work done within this thesis highlights that interdisciplinary knowledge on solar physics and its solar wind events improves our understanding of closely connected research fields. In particular, we showed for the first time how large-scale solar wind structures impact the occurrence of dynamic pressure enhancements in the Earth's magnetosheath. This predicts a substantial impact on the jet occurrence on the solar cycle. The collaborative study by Vuorinen et al. (2023b) investigated this connection, finding that the overall jet occurrence varies only little over a solar cycle, with a small dip of about 10 % during solar maximum. Vuorinen et al. (2023b) therefore answered the main overarching question posed in the research project which this thesis was part of. Furthermore, we showed that structured solar wind changes the ion energy distribution in the magnetosheath. This has significant consequences for correctly categorizing the magnetosheath and thus immediately showcases an example, where heliospheric physics can improve the science of near-Earth plasma physics.

Our work is also relevant for solar physics and the solar wind upstream of the shock: Koller et al. (2023) shows general plasma parameter distributions for solar wind structures, which is particularly relevant for statistical solar wind analysis (like Yermolaev et al., 2021). We also provide an overview of solar wind parameter correlations which is relevant for all statistical studies using the solar wind.

The datasets produced in our work are already utilized by other research groups: Vuorinen et al. (2023a) and Vuorinen et al. (2023b) used magnetosheath intervals and detected jets of Koller et al. (2022). Our magnetosheath interval detection algorithm based on Plaschke et al. (2013) and the jet detection algorithm (Koller et al., 2023) was adjusted to provide results for the Cluster mission. The list of magnetosheath jets detected in Cluster was recently published in Pöppelwerth et al. (2024). The results and datasets produced by our work open up the possibility for new research, as we will briefly discuss below.

6.4 Open Questions and Outlook

A variety of topics and questions that we touched on require further investigation. Statistics show us general connections of occurrences and properties, however, case studies are needed in order to understand the detailed physics that cause the statistical results. A dedicated magnetosheath jet case study in CME magnetic ejecta and CME-sheath conditions could put physical context to our statistical analysis on jet occurrence. Our work yielded implications on the general magnetosheath configuration in terms of quasi-parallel and quasi-perpendicular condition. This opens up the following question: how do solar wind structures impact the plasma stability in the terrestrial magnetosheath and magnetosheath jets? Such an analysis requires a reliable differentiation of quasi-parallel and quasi-perpendicular magnetosheath, as the plasma stability varies greatly between both regions. Our results in Koller et al. (2024) provides the means to improve this differentiation under different types of solar wind, while our work in Koller et al. (2023) provides a sufficient dataset to undertake this study. Analyzing plasma stability on this database work would greatly expand on the results by Soucek et al. (2015) (who used two years of Cluster data) by having a greater time range, covering more of the plasma parameter space, yielding results on solar wind structure, and answering the question on jet plasma stability. This work would also help to uncover connections between mirror modes and jets on a statistical level, which so far have been hinted at in case studies (Kajdič et al., 2021; Blanco-Cano et al., 2020; Blanco-Cano et al., 2023).

Our work also provides observational results utilizing different jet criteria. There are underlying biases for each type criteria which have not jet been thoroughly investigated. Showcasing jet differences could lead to a more physical jet criterion in the future. Our datasets can be used to get a global idea about the magnetosheath in structured solar wind, which would extend on the work of Turc et al. (2017) by including more types of solar wind events. Jets always depend on their environment, which means that jet parameter studies in each solar wind type require an analysis on the background magnetosheath. This finally also leads to the general question

on how the solar wind impacts the magnetosphere-ionosphere-terrestrial system by including the effects introduced by the bow shock and the magnetosheath. Our work helps to fill in missing gaps of our knowledge on how our environment is impacted by structures in the solar wind.

Bibliography

Ala-Lahti, Matti, Andrew P. Dimmock, Tuija I. Pulkkinen, et al. (Dec. 2021). „Transmission of an ICME Sheath Into the Earth's Magnetosheath and the Occurrence of Traveling Foreshocks". In: *Journal of Geophysical Research (Space Physics)* 126.12, e29896, e29896. DOI: 10.1029/2021JA029896 (cit. on p. 85).

Allen, R. C., G. C. Ho, L. K. Jian, et al. (June 2021). „A living catalog of stream interaction regions in the Parker Solar Probe era". In: *Astronomy & Astrophysics* 650, A25, A25. DOI: 10.1051/0004-6361/202039833 (cit. on p. 16).

Angelopoulos, V. (Dec. 2008). „The THEMIS Mission". In: *Space Science Reviews* 141.1-4, pp. 5–34. DOI: 10.1007/s11214-008-9336-1 (cit. on p. 11).

– (Dec. 2011). „The ARTEMIS Mission". In: *Space Science Reviews* 165.1-4, pp. 3–25. DOI: 10.1007/s11214-010-9687-2 (cit. on p. 11).

Archer, M. O., H. Hietala, M. D. Hartinger, F. Plaschke, and V. Angelopoulos (Dec. 2019). „Direct Observations of a Surface Eigenmode of the Dayside Magnetopause". In: *Nature Communications* 10.1, p. 615. DOI: 10.1038/s41467-018-08134-5 (cit. on pp. 37, 86).

Archer, M. O. and T. S. Horbury (Feb. 2013). „Magnetosheath Dynamic Pressure Enhancements: Occurrence and Typical Properties". In: *Annales Geophysicae* 31.2, pp. 319–331. DOI: 10.5194/angeo-31-319-2013 (cit. on pp. 30, 34).

Archer, M. O., T. S. Horbury, and J. P. Eastwood (May 2012). „Magnetosheath Pressure Pulses: Generation Downstream of the Bow Shock from Solar Wind Discontinuities: MAGNETOSHEATH PRESSURE PULSES". In: *Journal of Geophysical Research: Space Physics* 117.A5, n/a–n/a. DOI: 10.1029/2011JA017468 (cit. on pp. 31, 32).

Auster, H. U., K. H. Glassmeier, W. Magnes, et al. (Dec. 2008). „The THEMIS Fluxgate Magnetometer". In: *Space Science Reviews* 141.1-4, pp. 235–264. DOI: 10.1007/s11214-008-9365-9 (cit. on p. 11).

Balogh, André and Rudolf A. Treumann (2013). *Physics of Collisionless Shocks: Space Plasma Shock Waves*. Vol. 12. DOI: 10.1007/978-1-4614-6099-2 (cit. on pp. 19, 21–23).

Baumjohann, Wolfgang and Rudolf A. Treumann (1996). *Basic space plasma physics*. DOI: 10.1142/p015 (cit. on pp. 7, 8).

Bertucci, C., F. Duru, N. Edberg, et al. (Dec. 2011). „The Induced Magnetospheres of Mars, Venus, and Titan". In: *Space Science Reviews* 162.1-4, pp. 113–171. DOI: 10.1007/s11214-011-9845-1 (cit. on p. 19).

Blanco-Cano, X., L. Preisser, P. Kajdič, and D. Rojas-Castillo (Sept. 2020). „Magnetosheath Microstructure: Mirror Mode Waves and Jets during Southward IP Magnetic Field“. In: *Journal of Geophysical Research: Space Physics* 125.9. DOI: 10.1029/2020JA027940 (cit. on pp. 32, 34, 88).

Blanco-Cano, X., D. Rojas-Castillo, P. Kajdič, and L. Preisser (2023). „Jets and Mirror Mode Waves in Earth's Magnetosheath“. In: *Journal of Geophysical Research: Space Physics* 128.7. e2022JA031221 2022JA031221, e2022JA031221. DOI: https://doi.org/10.1029/2022JA031221. eprint: https://agupubs.onlinelibrary.wiley.com/doi/pdf/10.1029/2022JA031221 (cit. on pp. 32, 88).

Bonnell, J. W., F. S. Mozer, G. T. Delory, et al. (Dec. 2008). „The Electric Field Instrument (EFI) for THEMIS“. In: *Space Science Reviews* 141.1-4, pp. 303–341. DOI: 10.1007/s11214-008-9469-2 (cit. on p. 12).

Borovsky, Joseph E. (Oct. 2018). „The spatial structure of the oncoming solar wind at Earth and the shortcomings of a solar-wind monitor at L1“. In: *Journal of Atmospheric and Solar-Terrestrial Physics* 177, pp. 2–11. DOI: 10.1016/j.jastp.2017.03.014 (cit. on p. 11).

Borovsky, Joseph E., Michael H. Denton, and Charles W. Smith (2019). „Some Properties of the Solar Wind Turbulence at 1 AU Statistically Examined in the Different Types of Solar Wind Plasma“. In: *Journal of Geophysical Research: Space Physics* 124.4, pp. 2406–2424. DOI: https://doi.org/10.1029/2019JA026580. eprint: https://agupubs.onlinelibrary.wiley.com/doi/pdf/10.1029/2019JA026580 (cit. on pp. 17, 18).

Burch, J. L., T. E. Moore, R. B. Torbert, and B. L. Giles (Mar. 2016). „Magnetospheric Multiscale Overview and Science Objectives“. In: *Space Science Reviews* 199.1-4, pp. 5–21. DOI: 10.1007/s11214-015-0164-9 (cit. on p. 11).

Burgess, D. (Sept. 1997). „What do we really know about upstream waves?“ In: *Advances in Space Research* 20.4-5, pp. 673–682. DOI: 10.1016/S0273-1177(97)00455-9 (cit. on p. 22).

Burgess, David and Manfred Scholer (2015). *Collisionless Shocks in Space Plasmas*. DOI: 10.1017/CBO9781139044097 (cit. on pp. 19–21).

Camporeale, Enrico, Algo Carè, and Joseph E. Borovsky (Nov. 2017). „Classification of Solar Wind With Machine Learning“. In: *Journal of Geophysical Research (Space Physics)* 122.11, pp. 10, 910–10, 920. DOI: 10.1002/2017JA024383. arXiv: 1710.02313 [physics.space-ph] (cit. on p. 18).

Chen, P. F. (Apr. 2011). „Coronal Mass Ejections: Models and Their Observational Basis“. In: *Living Reviews in Solar Physics* 8.1, 1, p. 1. DOI: 10.12942/lrsp-2011-1 (cit. on p. 13).

Cranmer, Steven R. (Aug. 2002). „Coronal Holes and the High-Speed Solar Wind“. In: *Space Science Reviews* 101.3, pp. 229–294. DOI: 10.1023/A:1020840004535 (cit. on p. 14).

Cranmer, Steven R., Sarah E. Gibson, and Pete Riley (Nov. 2017). „Origins of the Ambient Solar Wind: Implications for Space Weather“. In: *Space Science Reviews* 212.3-4, pp. 1345–1384. DOI: 10.1007/s11214-017-0416-y. arXiv: 1708.07169 [astro-ph.SR] (cit. on p. 12).

Dimmock, A. P. and K. Nykyri (Aug. 2013). „The statistical mapping of magnetosheath plasma properties based on THEMIS measurements in the magnetosheath interplanetary medium reference frame“. In: *Journal of Geophysical Research (Space Physics)* 118.8, pp. 4963–4976. DOI: 10.1002/jgra.50465 (cit. on p. 25).

Dmitriev, Alexei V. and Alla V. Suvorova (Jan. 2023). „Atmospheric Effects of Magnetosheath Jets“. In: *Atmosphere* 14.1, p. 45. DOI: 10.3390/atmos14010045 (cit. on pp. 1, 37).

Eastwood, J. P., E. A. Lucek, C. Mazelle, et al. (June 2005). „The Foreshock“. In: *Space Science Reviews* 118.1-4, pp. 41–94. DOI: 10.1007/s11214-005-3824-3 (cit. on p. 22).

Escoubet, C. P., R. Schmidt, and M. L. Goldstein (Jan. 1997). „Cluster - Science and Mission Overview“. In: *Space Science Reviews* 79, pp. 11–32. DOI: 10.1023/A:1004923124586 (cit. on p. 11).

Escoubet, C. Philippe, K.-J. Hwang, S. Toledo-Redondo, et al. (Jan. 2020). „Cluster and MMS Simultaneous Observations of Magnetosheath High Speed Jets and Their Impact on the Magnetopause“. In: *Frontiers in Astronomy and Space Sciences* 6, p. 78. DOI: 10.3389/fspas.2019.00078 (cit. on p. 86).

Geyer, Paul, Manuela Temmer, Jingnan Guo, and Stephan G. Heinemann (May 2021). „Properties of stream interaction regions at Earth and Mars during the declining phase of SC 24“. In: *Astronomy and Astrophysics* 649, A80, A80. DOI: 10.1051/0004-6361/202040162. arXiv: 2102.05948 [astro-ph.EP] (cit. on p. 16).

Goncharov, O., H. Gunell, M. Hamrin, and S. Chong (2020). „Evolution of High-Speed Jets and Plasmoids Downstream of the Quasi-Perpendicular Bow Shock“. In: *Journal of Geophysical Research: Space Physics* 125.6, e2019JA027667. DOI: 10.1029/2019JA027667 (cit. on pp. 28, 32).

Gosling, J. T. and V. J. Pizzo (July 1999). „Formation and Evolution of Corotating Interaction Regions and their Three Dimensional Structure“. In: *Space Science Reviews* 89, pp. 21–52. DOI: 10.1023/A:1005291711900 (cit. on p. 14).

Green, Lucie M., Tibor Török, Bojan Vršnak, Ward Manchester, and Astrid Veronig (Feb. 2018). „The Origin, Early Evolution and Predictability of Solar Eruptions“. In: *Space Science Reviews* 214.1, 46, p. 46. DOI: 10.1007/s11214-017-0462-5. arXiv: 1801.04608 [astro-ph.SR] (cit. on p. 13).

Gunell, Herbert, Maria Hamrin, Sara Nesbit-Östman, Eva Krämer, and Hans Nilsson (2023). „Magnetosheath jets at Mars“. In: *Science Advances* 9.22, eadg5703. DOI: 10.1126/sciadv.adg5703. eprint: https://www.science.org/doi/pdf/10.1126/sciadv.adg5703 (cit. on p. 28).

Gurchumelia, Alexandre, Luca Sorriso-Valvo, David Burgess, et al. (June 2022). „Comparing Quasi-Parallel and Quasi-Perpendicular Configuration in the Terrestrial Magnetosheath: Multifractal Analysis“. In: *Frontiers in Physics* 10, 903632, p. 903632. DOI: 10.3389/fphy.2022.903632 (cit. on p. 27).

Han, De Sheng, J. J. Liu, X. C. Chen, et al. (2018). „Direct Evidence for Throat Aurora Being the Ionospheric Signature of Magnetopause Transient and Reflecting Localized Magnetopause Indentations“. In: *Journal of Geophysical Research: Space Physics* 123.4, pp. 2658–2667. DOI: 10.1002/2017JA024945 (cit. on p. 37).

Harten, Ronald and Kenn Clark (Feb. 1995). „The Design Features of the GGS Wind and Polar Spacecraft“. In: *Space Science Reviews* 71.1-4, pp. 23–40. DOI: 10.1007/BF00751324 (cit. on p. 11).

Hathaway, David H. (Dec. 2010). „The Solar Cycle“. In: *Living Reviews in Solar Physics* 7.1, 1, p. 1. DOI: 10.12942/lrsp-2010-1 (cit. on p. 19).

Heinemann, Stephan G., Manuela Temmer, Niko Heinemann, et al. (Oct. 2019). „Statistical Analysis and Catalog of Non-polar Coronal Holes Covering the SDO-Era Using CATCH“. In: *Solar Physics* 294.10, 144, p. 144. DOI: 10.1007/s11207-019-1539-y. arXiv: 1907.01990 [astro-ph.SR] (cit. on p. 18).

Hietala, H., N. Agueda, K. AndréEová, et al. (Oct. 2011). „In situ observations of particle acceleration in shock-shock interaction“. In: *Journal of Geophysical Research (Space Physics)* 116.A10, A10105, A10105. DOI: 10.1029/2011JA016669 (cit. on p. 85).

Hietala, H., T. V. Laitinen, K. Andréeová, et al. (2009). „Supermagnetosonic Jets behind a Collisionless Quasiparallel Shock“. In: *Physical Review Letters* 103.24, pp. 20–23. DOI: 10.1103/PhysRevLett.103.245001 (cit. on pp. 1, 31, 32, 34, 86).

Hietala, H., N. Partamies, T. V. Laitinen, et al. (Jan. 2012). „Supermagnetosonic Subsolar Magnetosheath Jets and Their Effects: From the Solar Wind to the Ionospheric Convection“. In: *Annales Geophysicae* 30.1, pp. 33–48. DOI: 10.5194/angeo-30-33-2012 (cit. on pp. 34, 85, 86).

Hietala, H., T. D. Phan, V. Angelopoulos, et al. (Feb. 2018). „In Situ Observations of a Magnetosheath High-Speed Jet Triggering Magnetopause Reconnection“. In: *Geophysical Research Letters* 45.4, pp. 1732–1740. DOI: 10.1002/2017GL076525 (cit. on pp. 1, 35, 86).

Hietala, H., D. Trotta, A. Fedeli, et al. (June 2024). „Candidates for downstream jets at interplanetary shocks“. In: *Monthly Notices of the Royal Astronomical Society* 531.2, pp. 2415–2421. DOI: 10.1093/mnras/stae1294 (cit. on p. 28).

Jian, L., C. T. Russell, J. G. Luhmann, and R. M. Skoug (Dec. 2006). „Properties of Stream Interactions at One AU During 1995 2004“. In: *Solar Physics* 239.1-2, pp. 337–392. DOI: 10.1007/s11207-006-0132-3 (cit. on p. 14).

Kajdič, Primož, Savvas Raptis, Xóchitl Blanco-Cano, and Tomas Karlsson (July 2021). „Causes of Jets in the Quasi-Perpendicular Magnetosheath“. In: *Geophysical Research Letters* 48.13, e93173, e93173. DOI: 10.1029/2021GL093173. arXiv: 2106.15747 [astro-ph.SR] (cit. on pp. 28, 32, 88).

Karlsson, T., N. Brenning, H. Nilsson, et al. (2012). „Localized Density Enhancements in the Magnetosheath: Three-dimensional Morphology and Possible Importance for Impulsive Penetration“. In: *Journal of Geophysical Research: Space Physics* 117.3, pp. 1–14. DOI: 10.1029/2011JA017059 (cit. on p. 34).

Karlsson, T., A. Kullen, E. Liljeblad, et al. (Sept. 2015). „On the Origin of Magnetosheath Plasmoids and Their Relation to Magnetosheath Jets“. In: *Journal of Geophysical Research: Space Physics* 120.9, pp. 7390–7403. DOI: 10.1002/2015JA021487 (cit. on p. 34).

Karlsson, T., S. Raptis, H. Trollvik, and H. Nilsson (Sept. 2021). „Classifying the Magnetosheath Behind the Quasi-Parallel and Quasi-Perpendicular Bow Shock by Local Measurements“. en. In: *Journal of Geophysical Research: Space Physics* 126.9, e2021JA029269. DOI: 10.1029/2021JA029269 (cit. on p. 27).

King, J. H. and N. E. Papitashvili (Feb. 2005). „Solar wind spatial scales in and comparisons of hourly Wind and ACE plasma and magnetic field data“. In: *Journal of Geophysical Research (Space Physics)* 110.A2, A02104, A02104. DOI: 10.1029/2004JA010649 (cit. on p. 11).

Koller, Florian, Ferdinand Plaschke, Manuela Temmer, et al. (Apr. 2023). „Magnetosheath Jet Formation Influenced by Parameters in Solar Wind Structures“. en. In: *Journal of Geophysical Research: Space Physics* 128.4, e2023JA031339. DOI: 10.1029/2023JA031339 (cit. on pp. 4, 5, 13, 15, 16, 27, 32, 33, 85, 87, 88).

Koller, Florian, Savvas Raptis, Manuela Temmer, and Tomas Karlsson (Mar. 2024). „The Effect of Fast Solar Wind on Ion Distribution Downstream of Earth's Bow Shock“. In: *The Astrophysical Journal Letters* 964.1, p. L5. DOI: 10.3847/2041-8213/ad2ddf (cit. on pp. 3, 5, 87, 88).

Koller, Florian, Manuela Temmer, Luis Preisser, et al. (Apr. 2022). „Magnetosheath Jet Occurrence Rate in Relation to CMEs and SIRs“. en. In: *Journal of Geophysical Research: Space Physics* 127.4, e2021JA030124. DOI: 10.1029/2021JA030124 (cit. on pp. 4, 5, 14, 16, 30, 33, 87, 88).

LaMoury, Adrian T., Heli Hietala, Ferdinand Plaschke, Laura Vuorinen, and Jonathan P. Eastwood (Sept. 2021). „Solar Wind Control of Magnetosheath Jet Formation and Propagation to the Magnetopause“. In: *Journal of Geophysical Research: Space Physics* 126.9. DOI: 10.1029/2021JA029592 (cit. on pp. 2, 28, 32, 33).

Lavraud, Benoit and Joseph E. Borovsky (Sept. 2008). „Altered solar wind-magnetosphere interaction at low Mach numbers: Coronal mass ejections“. In: *Journal of Geophysical Research (Space Physics)* 113.A9, A00B08, A00B08. DOI: 10.1029/2008JA013192 (cit. on pp. 85, 86).

Liu, Terry Z., Heli Hietala, Vassilis Angelopoulos, Rami Vainio, and Yuri Omelchenko (July 2020a). „Electron Acceleration by Magnetosheath Jet-Driven Bow Waves“. In: *Journal of Geophysical Research: Space Physics* 125.7. DOI: 10.1029/2019JA027709 (cit. on p. 34).

Liu, Terry Z., Heli Hietala, Vassilis Angelopoulos, et al. (July 2019). „THEMIS Observations of Particle Acceleration by a Magnetosheath Jet-Driven Bow Wave“. In: *Geophysical Research Letters* 46.14, pp. 7929–7936. DOI: 10.1029/2019GL082614 (cit. on p. 34).

Liu, Terry Z., Heli Hietala, Vassilis Angelopoulos, et al. (July 2020b). „Statistical Study of Magnetosheath Jet-Driven Bow Waves“. In: *Journal of Geophysical Research* 125.7. DOI: 10.1029/2019ja027710 (cit. on p. 34).

McFadden, J. P., C. W. Carlson, D. Larson, et al. (Dec. 2008). „The THEMIS ESA Plasma Instrument and In-flight Calibration“. In: *Space Science Reviews* 141.1-4, pp. 277–302. DOI: 10.1007/s11214-008-9440-2 (cit. on p. 12).

Merka, J., A. Szabo, J. A. Slavin, and M. Peredo (2005). „Three-dimensional position and shape of the bow shock and their variation with upstream Mach numbers and interplanetary magnetic field orientation“. In: *Journal of Geophysical Research: Space Physics* 110.A4, pp. 1–13. DOI: 10.1029/2004JA010944 (cit. on p. 27).

Milošić, D., M. Temmer, S. G. Heinemann, et al. (Mar. 2023). „Improvements to the Empirical Solar Wind Forecast (ESWF) model“. In: *Solar Physics* 298.3, 45, p. 45. DOI: 10.1007/s11207-022-02102-5 (cit. on p. 18).

Němeček, Z., J. Šafránková, L. Přech, et al. (Apr. 1998). „Transient Flux Enhancements in the Magnetosheath“. In: *Geophysical Research Letters* 25.8, pp. 1273–1276. DOI: 10.1029/98GL50873 (cit. on pp. 1, 27, 86).

Ng, J., L.-J. Chen, and Y. A. Omelchenko (2021). „Bursty magnetic reconnection at the Earth's magnetopause triggered by high-speed jets“. In: *Physics of Plasmas* 28.9, p. 092902. DOI: 10.1063/5.0054394. eprint: https://doi.org/10.1063/5.0054394 (cit. on p. 35).

Norenius, L., M. Hamrin, O. Goncharov, et al. (Aug. 2021). „Ground-Based Magnetometer Response to Impacting Magnetosheath Jets“. In: *Journal of Geophysical Research: Space Physics* 126.8. DOI: 10.1029/2021JA029115 (cit. on p. 37).

Nykyri, K., M. Bengtson, V. Angelopoulos, Y. Nishimura, and S. Wing (June 2019). „Can Enhanced Flux Loading by High-Speed Jets Lead to a Substorm? Multipoint Detection of the Christmas Day Substorm Onset at 08:17 UT, 2015“. In: *Journal of Geophysical Research: Space Physics* 124.6, pp. 4314–4340. DOI: 10.1029/2018JA026357 (cit. on pp. 1, 35, 86).

Omidi, N., J. P. Eastwood, and D. G. Sibeck (2010). „Foreshock bubbles and their global magnetospheric impacts“. In: *Journal of Geophysical Research: Space Physics* 115.A6. DOI: https://doi.org/10.1029/2009JA014828. eprint: https://agupubs.onlinelibrary.wiley.com/doi/pdf/10.1029/2009JA014828 (cit. on p. 22).

Omidi, N., D. G. Sibeck, and X. Blanco-Cano (Aug. 2009). „Foreshock compressional boundary“. In: *Journal of Geophysical Research (Space Physics)* 114.A8, A08205, A08205. DOI: 10.1029/2008JA013950 (cit. on p. 23).

Parker, E. N. (Nov. 1958). „Dynamics of the Interplanetary Gas and Magnetic Fields.“ In: *Astrophysical Journal* 128, p. 664. DOI: 10.1086/146579 (cit. on p. 13).

Pizzo, V. (Dec. 1978). „A three-deminsional model of corotating streams in the solar wind 1. Theoretical foundations“. In: *Journal of Geophysical Research* 83.A12, pp. 5563–5572. DOI: 10.1029/JA083iA12p05563 (cit. on p. 17).

Plaschke, F., H. Hietala, and V. Angelopoulos (2013). „Anti-Sunward High-Speed Jets in the Subsolar Magnetosheath“. In: *Annales Geophysicae* 31.10, pp. 1877–1889. DOI: 10.5194/angeo-31-1877-2013 (cit. on pp. 2, 27, 28, 30, 32, 34, 35, 86, 88).

Plaschke, Ferdinand, Heli Hietala, Martin Archer, et al. (Aug. 2018). „Jets Downstream of Collisionless Shocks“. In: *Space Science Reviews* 214.5, 81, p. 81. DOI: 10.1007/s11214-018-0516-3 (cit. on pp. 1, 27, 28, 34).

Plaschke, Ferdinand, Heli Hietala, and Zoltan Vörös (Sept. 2020). „Scale Sizes of Magnetosheath Jets“. In: *Journal of Geophysical Research: Space Physics* 125.9. DOI: 10.1029/2020JA027962 (cit. on pp. 27, 34).

Pöppelwerth, Adrian, Florian Koller, Niklas Grimmich, et al. (2024). „Cluster: List of plasma jets in the subsolar magnetosheath“. In: *Frontiers in Astronomy and Space Sciences* 11. DOI: 10.3389/fspas.2024.1388307 (cit. on pp. 27, 88).

Preisser, Luis, Xóchitl Blanco-Cano, Primoz Kajdič, David Burgess, and Domenico Trotta (Sept. 2020). „Magnetosheath Jets and Plasmoids: Characteristics and Formation Mechanisms from Hybrid Simulations“. In: *The Astrophysical Journal Letters* 900.1, p. L6. DOI: 10.3847/2041-8213/abad2b (cit. on p. 31).

Raptis, Savvas, Tomas Karlsson, Ferdinand Plaschke, Anita Kullen, and Per-Arne Lindqvist (2020). „Classifying Magnetosheath Jets Using MMS: Statistical Properties“. In: *Journal of Geophysical Research: Space Physics* 125.11, e2019JA027754. DOI: 10.1029/2019JA027754 (cit. on pp. 27, 28, 32).

Raptis, Savvas, Tomas Karlsson, Andris Vaivads, et al. (Dec. 2022a). „Downstream High-Speed Plasma Jet Generation as a Direct Consequence of Shock Reformation“. In: *Nature Communications* 13.1, p. 598. DOI: 10.1038/s41467-022-28110-4 (cit. on pp. 1, 23, 31).

Raptis, Savvas, Tomas Karlsson, Andris Vaivads, et al. (Nov. 2022b). „On Magnetosheath Jet Kinetic Structure and Plasma Properties“. In: *Geophysical Research Letters* 49.21. DOI: 10.1029/2022GL100678 (cit. on pp. 34, 86).

Rouillard, A. P. (June 2011). „Relating white light and in situ observations of coronal mass ejections: A review“. In: *Journal of Atmospheric and Solar-Terrestrial Physics* 73.10, pp. 1201–1213. DOI: 10.1016/j.jastp.2010.08.015 (cit. on p. 13).

Schrijver, Carolus J. and George L. Siscoe (2009). *Heliophysics: Plasma Physics of the Local Cosmos*. Cambridge University Press. DOI: 10.1017/CBO9781107340657 (cit. on p. 19).

Schwartz, Steven J. and David Burgess (1991). „Quasi-parallel shocks: A patchwork of three-dimensional structures“. In: *Geophysical Research Letters* 18.3, pp. 373–376. DOI: https://doi.org/10.1029/91GL00138. eprint: https://agupubs.onlinelibrary.wiley.com/doi/pdf/10.1029/91GL00138 (cit. on p. 23).

Schwartz, Steven J., David Burgess, William P. Wilkinson, et al. (1992). „Observations of short large-amplitude magnetic structures at a quasi-parallel shock“. In: *Journal of Geophysical Research: Space Physics* 97.A4, pp. 4209–4227. DOI: https://doi.org/10.1029/91JA02581. eprint: https://agupubs.onlinelibrary.wiley.com/doi/pdf/10.1029/91JA02581 (cit. on p. 22).

Schwartz, Steven J., Chris P. Chaloner, Peter J. Christiansen, et al. (Nov. 1985). „An active current sheet in the solar wind“. In: *Nature* 318.6043, pp. 269–271. DOI: 10.1038/318269a0 (cit. on p. 22).

Schwenn, Rainer (Aug. 2006). „Space Weather: The Solar Perspective“. In: *Living Reviews in Solar Physics* 3.1, 2, p. 2. DOI: 10.12942/lrsp-2006-2 (cit. on pp. 12, 13).

Shue, J.-H., J.-K. Chao, P. Song, et al. (Sept. 2009). „Anomalous Magnetosheath Flows and Distorted Subsolar Magnetopause for Radial Interplanetary Magnetic Fields“. In: *Geophysical Research Letters* 36.18, p. L18112. DOI: 10.1029/2009GL039842 (cit. on pp. 25, 37).

Shue, J.-H., P. Song, C. T. Russell, et al. (1998). „Magnetopause location under extreme solar wind conditions“. In: *Journal of Geophysical Research: Space Physics* 103.A8, pp. 17691–17700. DOI: 10.1029/98JA01103 (cit. on p. 27).

Sibeck, D. G., T. -D. Phan, R. Lin, R. P. Lepping, and A. Szabo (Oct. 2002). „Wind observations of foreshock cavities: A case study“. In: *Journal of Geophysical Research (Space Physics)* 107.A10, 1271, p. 1271. DOI: 10.1029/2001JA007539 (cit. on p. 23).

Smith, E. J. and J. H. Wolfe (Mar. 1976). „Observations of interaction regions and corotating shocks between one and five AU: Pioneers 10 and 11“. In: *Geophysical Research Letters* 3.3, pp. 137–140. DOI: 10.1029/GL003i003p00137 (cit. on p. 14).

Smith, Edward J. (Aug. 2001). „The heliospheric current sheet“. In: *Journal of Geophysical Research* 106.A8, pp. 15819–15832. DOI: 10.1029/2000JA000120 (cit. on p. 16).

Soucek, Jan, C. Philippe Escoubet, and Benjamin Grison (2015). „Magnetosheath plasma stability and ULF wave occurrence as a function of location in the magnetosheath and upstream bow shock parameters“. In: *Journal of Geophysical Research: Space Physics* 120.4, pp. 2838–2850. DOI: https://doi.org/10.1002/2015JA021087. eprint: https://agupubs.onlinelibrary.wiley.com/doi/pdf/10.1002/2015JA021087 (cit. on p. 88).

Stone, E. C., A. M. Frandsen, R. A. Mewaldt, et al. (July 1998). „The Advanced Composition Explorer“. In: *Space Science Reviews* 86, pp. 1–22. DOI: 10.1023/A:1005082526237 (cit. on p. 11).

Suni, J., M. Palmroth, L. Turc, et al. (Oct. 2021). „Connection Between Foreshock Structures and the Generation of Magnetosheath Jets: Vlasiator Results“. In: *Geophysical Research Letters* 48.20. DOI: 10.1029/2021GL095655 (cit. on pp. 1, 31).

Suni, Jonas, Minna Palmroth, Lucile Turc, et al. (Dec. 2023). „Local bow shock environment during magnetosheath jet formation: results from a hybrid-Vlasov simulation“. In: *Annales Geophysicae* 41.2, pp. 551–568. DOI: 10.5194/angeo-41-551-2023 (cit. on p. 31).

Tatrallyay, M., C. T. Russell, J. D. Mihalov, and A. Barnes (July 1983). „Factors controlling the location of the venus bow shock“. In: *Journal of Geophysical Research: Space Physics* 88.A7, pp. 5613–5622. DOI: 10.1029/JA088iA07p05613 (cit. on p. 19).

Temmer, M. and V. Bothmer (Sept. 2022). „Characteristics and evolution of sheath and leading edge structures of interplanetary coronal mass ejections in the inner heliosphere based on Helios and Parker Solar Probe observations“. In: *Astronomy and Astrophysics* 665, A70, A70. DOI: 10.1051/0004-6361/202243291. arXiv: 2202.04391 [astro-ph.SR] (cit. on p. 14).

Temmer, Manuela (Dec. 2021). „Space weather: the solar perspective“. In: *Living Reviews in Solar Physics* 18.1, 4, p. 4. DOI: 10.1007/s41116-021-00030-3 (cit. on pp. 1, 12, 17).

Tinoco-Arenas, Arturo, Primož Kajdič, Luis Preisser, et al. (Feb. 2022). „Parametric Study of Magnetosheath Jets in 2D Local Hybrid Simulations“. In: *Frontiers in Astronomy and Space Sciences* 9, p. 793195. DOI: 10.3389/fspas.2022.793195 (cit. on p. 33).

Treumann, Rudolf A. and Wolfgang Baumjohann (1997). *Advanced space plasma physics*. DOI: 10.1142/p020 (cit. on p. 7).

Tsurutani, Bruce T., Walter D. Gonzalez, Alicia L. C. Gonzalez, et al. (2006). „Corotating solar wind streams and recurrent geomagnetic activity: A review“. In: *Journal of Geophysical Research: Space Physics* 111.A7. DOI: https://doi.org/10.1029/2005JA011273. eprint: https://agupubs.onlinelibrary.wiley.com/doi/pdf/10.1029/2005JA011273 (cit. on p. 14).

Turc, L., C. P. Escoubet, D. Fontaine, E. K. J. Kilpua, and S. Enestam (May 2016). „Cone angle control of the interaction of magnetic clouds with the Earth's bow shock“. In: *Geophysical Research Letters* 43.10, pp. 4781–4789. DOI: 10.1002/2016GL068818 (cit. on p. 85).

Turc, L., D. Fontaine, C. P. Escoubet, E. K. J. Kilpua, and A. P. Dimmock (Mar. 2017). „Statistical study of the alteration of the magnetic structure of magnetic clouds in the Earth's magnetosheath“. en. In: *Journal of Geophysical Research: Space Physics* 122.3, pp. 2956–2972. DOI: 10.1002/2016JA023654 (cit. on pp. 85, 88).

Turc, L., D. Fontaine, P. Savoini, H. Hietala, and E. K. J. Kilpua (June 2013). „A comparison of bow shock models with Cluster observations during low Alfvén Mach number magnetic clouds“. In: *Annales Geophysicae* 31.6, pp. 1011–1019. DOI: 10.5194/angeo-31-1011-2013 (cit. on p. 85).

Turc, L., D. Fontaine, P. Savoini, and E. K. J. Kilpua (Feb. 2014a). „A model of the magnetosheath magnetic field during magnetic clouds“. In: *Annales Geophysicae* 32.2, pp. 157–173. DOI: 10.5194/angeo-32-157-2014 (cit. on p. 85).

– (Oct. 2014b). „Magnetic clouds' structure in the magnetosheath as observed by Cluster and Geotail: four case studies“. In: *Annales Geophysicae* 32.10, pp. 1247–1261. DOI: 10.5194/angeo-32-1247-2014 (cit. on pp. 85, 86).

Turc, L., D. Fontaine, P. Savoini, and R. Modolo (Aug. 2015). „3D hybrid simulations of the interaction of a magnetic cloud with a bow shock“. In: *Journal of Geophysical Research (Space Physics)* 120.8, pp. 6133–6151. DOI: 10.1002/2015JA021318 (cit. on p. 85).

Turc, L., O. W. Roberts, M. O. Archer, et al. (Nov. 2019). „First Observations of the Disruption of the Earth's Foreshock Wave Field During Magnetic Clouds“. In: *Geophysical Research Letters* 46.22, pp. 12, 644–12, 653. DOI: 10.1029/2019GL084437 (cit. on p. 85).

Verscharen, Daniel, Kristopher G. Klein, and Bennett A. Maruca (Dec. 2019). „The multi-scale nature of the solar wind“. en. In: *Living Reviews in Solar Physics* 16.1, p. 5. DOI: 10.1007/s41116-019-0021-0 (cit. on pp. 8, 27).

Vuorinen, Laura, Heli Hietala, Adrian T. LaMoury, and Ferdinand Plaschke (Oct. 2023a). „Solar Wind Parameters Influencing Magnetosheath Jet Formation: Low and High IMF Cone Angle Regimes“. In: *Journal of Geophysical Research (Space Physics)* 128.10, e2023JA031494, e2023JA031494. DOI: 10.1029/2023JA031494 (cit. on pp. 32, 88).

Vuorinen, Laura, Heli Hietala, and Ferdinand Plaschke (Aug. 2019). „Jets in the Magnetosheath: IMF Control of Where They Occur“. In: *Annales Geophysicae* 37.4, pp. 689–697. DOI: 10.5194/angeo-37-689-2019 (cit. on pp. 2, 32).

Vuorinen, Laura, Heli Hietala, Ferdinand Plaschke, and Adrian T. LaMoury (Sept. 2021). „Magnetic Field in Magnetosheath Jets: A Statistical Study of B_Z Near the Magnetopause“. In: *Journal of Geophysical Research: Space Physics* 126.9. DOI: 10.1029/2021JA029188 (cit. on p. 35).

Vuorinen, Laura, Adrian T. LaMoury, Heli Hietala, and Florian Koller (Aug. 2023b). „Magnetosheath Jets Over Solar Cycle 24: An Empirical Model“. en. In: *Journal of Geophysical Research: Space Physics* 128.8, e2023JA031493. DOI: 10.1029/2023JA031493 (cit. on pp. 12, 33, 34, 87, 88).

Vuorinen, Laura, Rami Vainio, Heli Hietala, and Terry Z. Liu (Aug. 2022). „Monte Carlo Simulations of Electron Acceleration at Bow Waves Driven by Fast Jets in the Earth's Magnetosheath“. In: *The Astrophysical Journal* 934.2, p. 165. DOI: 10.3847/1538-4357/ac7f42 (cit. on p. 34).

Walsh, B. M., T. Bhakyapaibul, and Y. Zou (2019). „Quantifying the Uncertainty of Using Solar Wind Measurements for Geospace Inputs“. In: *Journal of Geophysical Research: Space Physics* 124.5, pp. 3291–3302. DOI: https://doi.org/10.1029/2019JA026507. eprint: https://agupubs.onlinelibrary.wiley.com/doi/pdf/10.1029/2019JA026507 (cit. on pp. 11, 30).

Wang, Boyi, Yukitoshi Nishimura, Heli Hietala, and Vassilis Angelopoulos (Nov. 2022). „Investigating the Role of Magnetosheath High-Speed Jets in Triggering Dayside Ground Magnetic Ultra-Low Frequency Waves“. In: *Geophysical Research Letters* 49.22. DOI: 10.1029/2022GL099768 (cit. on pp. 1, 37).

Wang, Boyi, Yukitoshi Nishimura, Heli Hietala, et al. (June 2018). „Impacts of Magnetosheath High-Speed Jets on the Magnetosphere and Ionosphere Measured by Optical Imaging and Satellite Observations“. In: *Journal of Geophysical Research: Space Physics* 123.6, pp. 4879–4894. DOI: 10.1029/2017JA024954 (cit. on p. 37).

Webb, David F. and Timothy A. Howard (June 2012). „Coronal Mass Ejections: Observations“. In: *Living Reviews in Solar Physics* 9.1, 3, p. 3. DOI: 10.12942/lrsp-2012-3 (cit. on p. 13).

Xirogiannopoulou, N., O. Goncharov, J. Šafránková, and Z. Němeček (2024). „Characteristics of Foreshock Subsolar Compressive Structures“. In: *Journal of Geophysical Research: Space Physics* 129.2. e2023JA032033 2023JA032033, e2023JA032033. DOI: https://doi.org/10.1029/2023JA032033. eprint: https://agupubs.onlinelibrary.wiley.com/doi/pdf/10.1029/2023JA032033 (cit. on pp. 22, 31).

Xu, Fei and Joseph E. Borovsky (Jan. 2015). „A new four-plasma categorization scheme for the solar wind“. en. In: *Journal of Geophysical Research: Space Physics* 120.1, pp. 70–100. DOI: 10.1002/2014JA020412 (cit. on pp. 17, 18).

Yermolaev, Yu. I., N. S. Nikolaeva, I. G. Lodkina, and M. Yu. Yermolaev (Apr. 2009). „Catalog of large-scale solar wind phenomena during 1976-2000“. In: *Cosmic Research* 47.2, pp. 81–94. DOI: 10.1134/S0010952509020014 (cit. on p. 13).

Yermolaev, Yuri I., Irina G. Lodkina, Alexander A. Khokhlachev, et al. (Sept. 2021). „Drop of Solar Wind at the End of the 20th Century“. In: *Journal of Geophysical Research (Space Physics)* 126.9, e29618, e29618. DOI: 10.1029/2021JA029618. arXiv: 2105.10955 [astro-ph.SR] (cit. on pp. 13, 87).

Yordanova, Emiliya, Zoltán Vörös, Savvas Raptis, and Tomas Karlsson (Feb. 2020). „Current sheet statistics in the magnetosheath“. In: *Frontiers in Astronomy and Space Sciences* 7, 2, p. 2. DOI: 10.3389/fspas.2020.00002 (cit. on p. 27).

Zhang, H., D. G. Sibeck, Q.-G. Zong, et al. (2013). „Spontaneous hot flow anomalies at quasi-parallel shocks: 1. Observations“. In: *Journal of Geophysical Research: Space Physics* 118.6, pp. 3357–3363. DOI: https://doi.org/10.1002/jgra.50376. eprint: https://agupubs.onlinelibrary.wiley.com/doi/pdf/10.1002/jgra.50376 (cit. on p. 23).

Zhang, Hui, Qiugang Zong, Hyunju Connor, et al. (Aug. 2022). „Dayside Transient Phenomena and Their Impact on the Magnetosphere and Ionosphere“. In: *Space Science Reviews* 218.5, p. 40. DOI: 10.1007/s11214-021-00865-0 (cit. on pp. 22, 23).

Zhou, Yufei, Savvas Raptis, Shan Wang, et al. (Jan. 2024). „Magnetosheath jets at Jupiter and across the solar system“. In: *Nature Communications* 15.1, p. 4. DOI: 10.1038/s41467-023-43942-4 (cit. on p. 28).

Zhou, Yufei, Chao Shen, and Yong Ji (2023). „Undulated Shock Surface Formed After a Shock–Discontinuity Interaction“. In: *Geophysical Research Letters* 50.10. e2023GL103848 2023GL103848, e2023GL103848. DOI: https://doi.org/10.1029/2023GL103848. eprint: https://agupubs.onlinelibrary.wiley.com/doi/pdf/10.1029/2023GL103848 (cit. on p. 31).

List of Publications

Refereed journal publications

Within this work I published the following 3 peer-reviewed articles as first author. These articles were reproduced in this work.

1. **Koller, F.**, Temmer, M., Preisser, L., Plaschke, F., Geyer, P., Jian, L. K., Roberts, O. W., Hietala, H., LaMoury, A., **Magnetosheath Jet Occurrence Rate in Relation to CMEs and SIRs**, Journal of Geophysical Research: Space Physics, Volume 127, e2021JA030124, DOI: 10.1029/2021JA030124, (2022)

2. **Koller, F.**, Plaschke, F., Temmer, M., Preisser, L., Roberts, O. W., Vörös, Z., **Magnetosheath Jet Formation Influenced by Parameters in Solar Wind Structures**, Journal of Geophysical Research: Space Physics, Volume 128, e2023JA031339, DOI: 10.1029/2023JA031339, (2023)

3. **Koller, F.**, Raptis, S., Temmer, M., Karlsson, T., **The Effect of Fast Solar Wind on Ion Distribution Downstream of Earth's Bow Shock**, The Astrophysical Journal Letters, Volume 964, L5, DOI: 10.3847/2041-8213/ad2ddf, (2024)

I contributed to the following three peer-reviewed articles. Two were published and one is accepted for publication.

1. Vuorinen, L., LaMoury, A. T., Hietala, H., **Koller, F.**, **Magnetosheath jets over solar cycle 24: An empirical model**, Journal of Geophysical Research: Space Physics, 128, e2023JA031493. DOI: 10.1029/2023JA031493,(2023)

2. Pöppelwerth, A., **Koller, F.**, Grimmich, N., Constantinescu, D., Glebe, G., Vörös, Z., Temmer, M., Simon Wedlund, C., Plaschke, F., **Cluster: List of plasma jets in the subsolar magnetosheath**, Frontiers in Astronomy and Space Sciences, 11, DOI: 10.3389/fspas.2024.1388307, (2024)

3. Pöppelwerth, A., Glebe, G., Mieth, J.Z.D., **Koller, F.**, Karlsson, T., Vörös, Z., Plaschke, F., **Scale Size Estimation of Magnetosheath Jets**, accepted for publication in Annales Geophysicae. Preprint DOI:10.5194/angeo-2023-31. (2024)

Two more articles with my contributions are currently in preparation: an article on magnetosheath instabilities which serves as a direct continuation of the presented work, and a review article on the latest results on magnetosheath jets lead by early career scientists in the field.

1. **Koller, F.**, Simon Wedlund, C., Plaschke, F., Temmer, M., Svenningson, I., Preisser, L., Roberts, O. W., Vörös, Z. **Dayside Magnetosheath Plasma Stability: Effects of1 Jets and Solar Winds Structures**, Journal of Geophysical Research: Space Physics, in preparation.

2. Krämer, E., **Koller, F.**, Suni, J., LaMoury, A., Pöppelwerth, A., et al. **Jets Downstream of Collisionless Shocks: Recent discoveries and Challenges**, Space Science Reviews, in preparation.

Colophon

This thesis was typeset with LaTeX 2$_\varepsilon$. It uses the *Clean Thesis* style developed by Ricardo Langner, available at http://cleanthesis.der-ric.de/. The design of the *Clean Thesis* style is inspired by user guide documents from Apple Inc.

The template is provided in this adapted version by Desmond Grossmann, BSc, Stefan Janisch, BSc, Lea Schimak and Paul Beck, PhD to implement the editorial guidelines of *Astronomy & Astrophysics* and the cooperate-identity guidelines of the University of Graz for the Institute for Physics. Version: March, 2024.